Modélisation non-linéaire du transport en présence d'instabilité MHD du plasma périphérique de tokamak.

Eric Nardon

ÉCOLE POLYTECHNIQUE

Département de Recherches
sur la Fusion Controlée
CEA Cadarache

Thèse de doctorat de l'École Polytechnique

Spécialité :

Physique

Présentée par :

Éric NARDON

EDGE LOCALIZED MODES CONTROL BY RESONANT MAGNETIC PERTURBATIONS

CONTRÔLE DES INSTABILITÉS DE BORD PAR PERTURBATIONS MAGNÉTIQUES RÉSONANTES

Soutenue le 31 octobre 2007 devant le jury composé de :

Marina BÉCOULET	Responsable CEA, Ingénieur de recherches CEA
Peter BEYER	Rapporteur, Prof. à l'Université de Provence
Michel CHATELIER	Directeur de recherches CEA
Gerardus HUYSMANS	Ingénieur de recherches CEA
Jean-Marcel RAX	Directeur de thèse, Prof. à l'Univ. de Paris XI
François WAELBROECK	Rapporteur, Prof. à l'Université d'Austin, Texas

Remerciements

Mes premiers remerciements vont à Michel Chatelier, chef du Département de Recherches sur la Fusion Contrôlée et à André Grosman, chef du Service Intégration Plasma Paroi, pour leur accueil et les conditions de travail excellentes dont j'ai pu bénéficier pendant ces trois ans. En particulier, j'ai apprécié la possibilité de participer à des conférences et workshops internationaux, qui m'ont permis de rencontrer les chercheurs de mon domaine et de leur faire connaître mon travail. Un second merci à Michel Chatelier pour avoir accepté de présider mon jury de thèse.

Merci à Jean-Marcel Rax de m'avoir fait l'honneur d'être mon directeur de thèse et d'avoir appuyé ma candidature pour l'obtention d'une bourse CFR.

Merci également à mes deux rapporteurs, Peter Beyer et François Waelbroeck, qui ont relu mon manuscrit en détail et qui ont fait le déplacement pour venir à ma soutenance (depuis les Etats-Unis dans le cas de François !).

Mes remerciements les plus chaleureux vont ensuite à Marina Bécoulet, mon encadrante CEA, et à Guido Huysmans. C'était un réel plaisir que de travailler avec vous pendant ces trois ans. Je me suis toujours senti fortement soutenu et j'ai beaucoup appris à vos côtés. Un remerciement particulier à Marina qui a été une encadrante exemplaire et qui s'est beaucoup investie pour m'offrir la meilleure formation possible.

Pour les nombreux coups de mains rendus toujours avec le sourire, en particulier ces dernières semaines pour l'organisation de la soutenance, j'adresse mes sincères remerciements aux secrétaires du SIPP : Colette Junique, Laurence Azcona et Yvonne Barbu.

Je voudrais maintenant remercier toutes les autres personnes que j'ai pris plaisir à côtoyer sur le centre au cours de ces trois années. Je commencerai par les "permanents" : Philippe Ghendrih (merci pour les leçons de physique toujours très instructives), Xavier Garbet, Yanick Sarazin, Gloria Falchetto, Rémi Dumont, Maurizio Ottaviani, Virginie Grandgirard, Chantal Passeron, Patrick Maget, Pascale Monier-Garbet, Alain Bécoulet, Tuong Hoang, Sylvain Brémond, Paul Thomas... Je continuerai par les nombreux post-docs, thésards et stagiaires dont j'ai croisé la route au DRFC : Stéphanie Fouquet, Olivier Czarny (à qui je dois d'innombrables dépannages numériques délivrés avec la plus grande patience), Guido "éééé" Ciraolo, Nathanaël Schaeffer, Joan Decker, Aurélien Mendès, Nicolas Arcis et Antoine Sirinelli que j'aurai plaisir à rejoindre à Oxford, Nicolas Dubuit, Guillaume Attuel, Guilhem Dif-Pradalier, Thomas Gerbaud, Christine N'Guyen, Roland Bellessa, Stanislas Paméla, Thomas Parisot, Jean-Laurent Gardarein, Hassan Nesme,

Alexis Delias, Alex Palpant, Axel, Slim, Clément, Fred, Elysée, Maxime, Cyrille, Lucie... Un mot spécial pour ceux que j'ai le plus côtoyés, mes deux "compagnons de galère", Guillaume Darmet et Patrick Tamain. "Gros", j'ai beaucoup apprécié ta compagnie et j'espère qu'on se recroisera pour un petit tennis ou quelques bières. D'ici là je te souhaite bonne route... Quant à toi Patou, mon inséparable co-bureau, sache que ce n'est pas sans une certaine émotion que je repenserai aux petits objets que tu me lançais si affectueusement à la figure quand tu avais bu trop de café, à tes "problèmes de maths insolubles", à notre exploration de la Chine après PSI, aux raids... On devrait se voir dans pas longtemps sur Oxford de toute façon, et je serai ravi de t'y héberger ! Je finirai par mes amis sur le centre, en dehors du DRFC : Julien "los Ballinos" Balland, Mila, Elie, Steph "Super Romain" Reboul, Camille, Bruno, J.B., Steph Renaud, Vincent Feuillou, Maud, tous les footeux du mercredi et du vendredi et bien-sûr l'équipe des Mercenaires (avec encore toutes mes excuses pour ce pénalty pitoyable qui nous a privés de finale...).

Merci à mes différents colocataires des Platanes : Alex, Patrice, Célia, Cha, Marie, Céline, Emily.

Un très grand merci à mes parents, qui m'ont toujours soutenu dans mes études, tant financièrement que moralement.

Enfin, merci à Amélie, qui a sacrifié ses vacances d'été pour rester vivre avec un thésard en pleine rédaction. Ca m'a beaucoup aidé. Je te revaudrai ça...

Summary

The control of Edge Localized Modes (ELMs) is a capital question for the future ITER tokamak. The present work is dedicated to one of the most promising methods of control of the ELMs, based on a system of coils producing Resonant Magnetic Perturbations (RMPs), the efficiency of which was first demonstrated in the DIII-D tokamak in 2003. Our main objectives are, on the one hand, to improve the physical understanding of the mechanisms at play, and on the other hand to propose a concrete design of ELMs control coils for ITER.

In order to calculate and analyze the magnetic perturbations produced by a given set of coils, we have developed the ERGOS code. The first ERGOS calculation was for the DIII-D ELMs control coils, the I-coils. It showed that they produce magnetic islands chains which overlap at the edge of the plasma, resulting in the ergodization of the magnetic field.

We have then used ERGOS for the modelling of the experiments on ELMs control using the error field correction coils at JET and MAST, to which we participate since 2006. In the case of JET, we have shown the existence of a correlation between the mitigation of the ELMs and the ergodization of the magnetic field at the edge, in agreement with the DIII-D result.

The design of ELMs control coils for ITER was done principally in the frame of an EFDA[1]-CEA contract, in collaboration with engineers from EFDA and ITER. We used ERGOS intensitvely, taking the case of the DIII-D I-coils as a reference. Three candidate designs came out, which we presented at the ITER Design Review, in 2007. Recently, the ITER management decided to provide a budget for building ELMs control coils, the design of which remains to be chosen between two of the three options that we proposed[2].

Finally, in order to understand better the non-linear magnetohydrodynamics phenomena taking place in ELMs control by RMPs, we performed numerical simulations, in particular with the JOREK code for a DIII-D case. The simulations reveal the existence of convection cells induced at the edge by the magnetic perturbations, and the possible screening of the RMPs in presence of rotation. The adequate modelling of the screening, which requires to add more physics into JOREK, has been started.

[1] European Fusion Development Agreement

[2] or close to the ones we proposed

Résumé

Le contrôle des instabilités de bord connues sous le nom d'"*Edge Localized Modes*" (ELMs) est une question capitale pour le futur tokamak ITER. Ce travail est consacré à l'une des plus prometteuses méthodes de contrôle des ELMs, basée sur un système de bobines produisant des Perturbations Magnétiques Résonantes (PMRs), dont le fonctionnement a été démontré en premier lieu dans le tokamak DIII-D en 2003. Nos objectifs principaux sont, d'une part, d'éclaircir la compréhension physique des mécanismes en jeu, et d'autre part, de proposer un design concret de bobines de contrôle des ELMs pour ITER.

Afin de calculer et d'analyser les perturbations magnétiques créées par un ensemble de bobines donné, nous avons développé le code ERGOS. Le premier calcul ERGOS a été consacré aux bobines de contrôle des ELMs de DIII-D, les I-coils. Il montre que celles-ci créent des chaines d'îlots magnétiques se recouvrant au bord du plasma, engendrant ainsi une ergodisation du champ magnétique.

Nous avons par la suite utilisé ERGOS pour la modélisation des expériences de contrôle des ELMs à l'aide des bobines de correction de champ d'erreur sur JET et MAST, auxquelles nous participons depuis 2006. Dans le cas de JET, nous avons montré l'existence d'une corrélation entre la mitigation des ELMs et l'ergodisation du champ magnétique au bord, en accord avec le résultat pour DIII-D.

Le design des bobines de contrôle des ELMs pour ITER s'est fait principalement dans le cadre d'un contrat EFDA[3]-CEA, en collaboration avec des ingénieurs et physiciens de l'EFDA et d'ITER. Nous avons utilisé ERGOS intensivement, le cas des I-coils de DIII-D nous servant de référence. Trois designs candidats sont ressortis, que nous avons présentés au cours de la revue de design d'ITER, en 2007. La direction d'ITER a décidé récemment d'attribuer un budget pour les bobines de contrôle des ELMs, dont le design reste à choisir entre deux des trois options que nous avons proposées[4].

Enfin, dans le but de mieux comprendre les phénomènes de magnétohydrodynamique non-linéaires liés au contrôle des ELMs par PMRs, nous avons recouru à la simulation numérique, notamment avec le code JOREK pour un cas DIII-D. Les simulations révèlent l'existence de cellules de convection induites au bord du plasma par les perturbations magnétiques et le possible "écrantage" des PMRs par le plasma en présence de rotation. La modélisation adéquate de l'écrantage, qui demande la prise en compte de plusieurs phénomènes physiques supplémentaires dans JOREK, a été entamée.

[3] *European Fusion Development Agreement*

[4] ou proches de celles que nous avons proposées

Contents

Chapter 1

Introduction

1.1 General introduction to fusion

The general objective of present research on nuclear fusion [1] is to exploit the fusion reaction of deuterium (D) and tritium (T):

$$ {}^{2}_{1}D \ + \ {}^{3}_{1}T \quad \rightarrow \quad {}^{4}_{2}He \ (3.56\text{MeV}) \ + \ n \ (14.03\text{MeV}). \tag{1.1} $$

The numbers between parenthesis are the energies carried by the reaction products, which are a helium (He) nucleus (also called "alpha particle") and a neutron (n). There exist other possible fusion reactions (in particular the $D-D$ one, which is interesting given the large quantity of deuterium on Earth) but they are more difficult to realize. The reaction rate depends on the temperature and has a maximum around 20keV (i.e. $\sim 2 \cdot 10^8$K), which is therefore the target temperature in a fusion reactor. At such a temperature, the $D-T$ mix is in the state of a hot plasma (i.e. a totally ionized gas).
The amplification factor, usually denoted Q, of a fusion reactor, is defined as:

$$ Q \equiv \frac{P_{fus}}{P_{inj}}, \tag{1.2} $$

where P_{fus} is the power exhausted by fusion reactions and P_{inj} the power injected into the reactor. The higher the Q, the more "profitable" the reactor. When Q reaches the value of 1, one gets back from the fusion reaction as much power as one "invests" into the reactor. This situation, called "break even", was almost reached in recent years in the JET tokamak. When approaching ignition (the stage where the fusion reaction is self-sustained), it is not necessary to inject anymore power into the reactor, so that P_{inj} can approach 0 and Q tends to infinity. For fusion reactors to be economically competitive, the desired value of Q is about 50. The future experimental reactor ITER (described below) aims at reaching $Q = 10$ routinely.
A critical parameter that appears when developing the expression of Q is the energy confinement time, τ_E, which is defined as the ratio of the thermal energy accumulated in the plasma over the power injected into the plasma:

$$ \tau_E \equiv \frac{W_{th}}{P_{inj}}. \tag{1.3} $$

It can be shown that any objective in terms of Q (for a given plasma temperature) can be translated into an objective in terms of the $n\tau_E$ product, where n is the plasma density. The objective is thus to maximize the $n\tau_E$ product. To do that, two approaches exist:

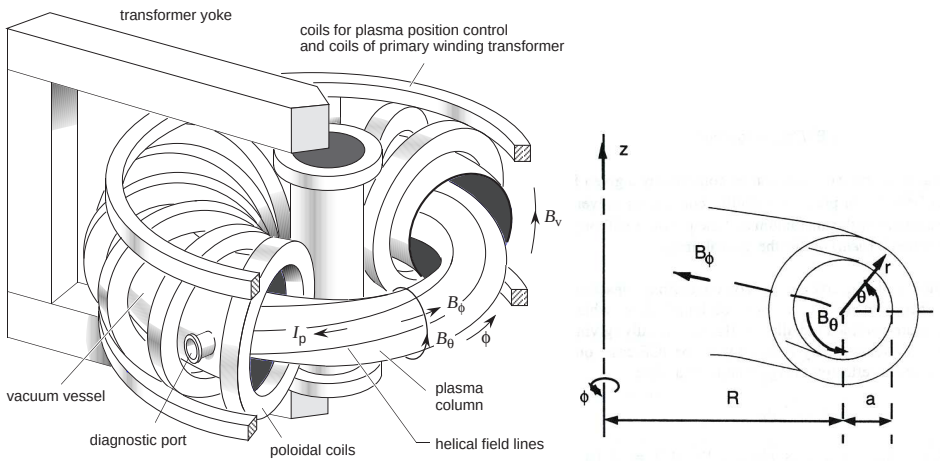

Figure 1.1: Typical configuration (left) and coordinates system (right) of a tokamak. From [9].

- In nuclear fusion by inertial confinement, solid $D-T$ targets are heated by a laser pulse, which provokes an explosion, the resulting $D-T$ plasma being "confined" only by its inertia. In this case, density is privileged over energy confinement time, with the typical values:

$$n \sim 10^{31}\mathrm{m}^{-3} \tag{1.4}$$
$$\tau_E \sim 10^{-11}\mathrm{s}. \tag{1.5}$$

- In nuclear fusion by magnetic confinement, the $D-T$ plasma has a very low density, but the energy confinement time is greatly enhanced by the use of a strong, confining, magnetic field (the plasma is much too hot to be contained by material walls). Typical values are:

$$n \sim 10^{20}\mathrm{m}^{-3} \tag{1.6}$$
$$\tau_E \sim 10\mathrm{s}. \tag{1.7}$$

1.2 The tokamak configuration

In a magnetic field, a charged particle gyrates around a magnetic field line with a radius of gyration called the "Larmor radius" and equal to:

$$\rho_L = \frac{mv_\perp}{qB}, \tag{1.8}$$

where m is the mass of the particle, $v_\perp$ its velocity perpendicularly to the magnetic field, q its charge, and B is the intensity of the magnetic field. For an ion from a D plasma with an ion temperature $T_i = 10\mathrm{keV}$, embedded in a magnetic field of 3T, if we take $v_\perp$ to be the ion thermal velocity $v_{th,i} = (T_i/m_i)^{1/2}$, we have $\rho_{L,i} \simeq 5 \cdot 10^{-3}\mathrm{m}$. The Larmor radius of the electrons, assuming $T_e = T_i$ (T_e being the electron temperature), is smaller by a factor $(m_e/m_i)^{1/2} \simeq 1.7 \cdot 10^{-2}$.

Hence, it seems possible to confine a fusion plasma by embedding it into a strong magnetic field with closed field lines, for instance in a solenoid closed on itself so as to

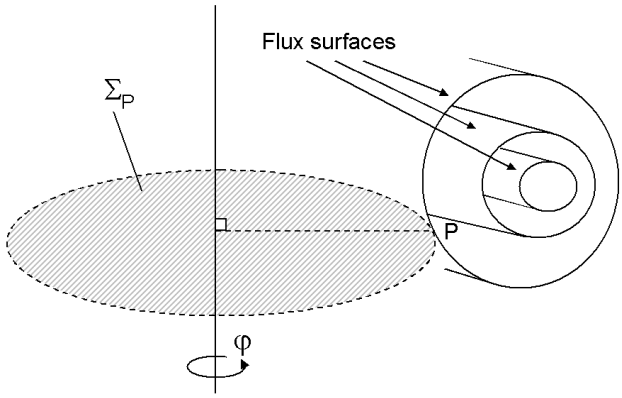

Figure 1.2: Geometry used in the definition of the poloidal magnetic flux ψ.

form a torus. However, in a non-constant magnetic field, the gyromotion of the particles is accompanied by a (slower) drift motion perpendicular to the magnetic field lines [3]. In a toroidal solenoid, plasma particles would drift vertically and be deconfined very fast. The tokamak concept relies on the addition of a so-called "poloidal" field B_p (denoted B_θ in fig. 1.1) to the toroidal magnetic field B_φ of the solenoid, this poloidal field being created by an electrical plasma current I_p flowing in the toroidal direction. The plasma current itself is typically generated by induction, using a transformer such as shown on fig. 1.1. This way, magnetic field lines are no longer circles but rather helicoidal curves generating nested surfaces with toroidal shapes (two of which can be seen on the right plot of fig. 1.1), usually referred to as "flux surfaces", and the vertical drift of the particles cancels out on average. In the particular case where flux surfaces have circular cross sections, it is easy to label them by their so-called "minor radius" r, cf. fig. 1.1 (right). In the general case, one classically makes use of the poloidal flux ψ, which is defined, at a given point P, as:

$$\psi(P) \equiv \iint_{\Sigma_P} \vec{B} \cdot d\vec{\Sigma_P}, \tag{1.9}$$

where Σ_P is the disk lying on P and whose axis is the axis of symmetry of the machine, cf. fig. 1.2. It is easily verified that ψ is constant on a given flux surface (hence the name "flux surface") and can therefore be used as a label for flux surfaces, i.e. as a radial-like coordinate.

The plasma is well confined as long as flux surfaces are closed. However, there necessarily exists a region where flux surfaces are intercepted by solid elements, which are usually called "Plasma Facing Components" (PFCs). The Last Closed Flux Surface (LCFS), also called "separatrix", is the frontier between the well confined core plasma and the "Scrape-Off Layer", where the plasma-surface interaction [40] takes place (cf. fig. 1.3). Two classical tokamak configurations are [40]:

- Limiter configurations (an example of which is Tore Supra [2]), where the separatrix

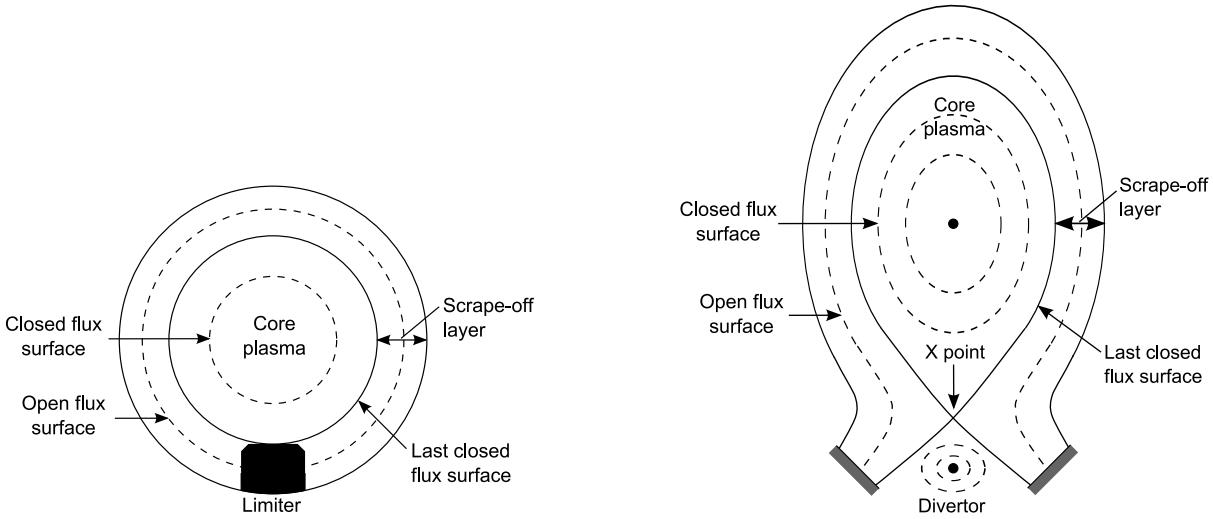

Figure 1.3: Poloidal cuts, i.e. cuts by a plane of constant φ, showing the limiter (left) and axisymmetric poloidal divertor (right) configurations.

is directly due to the presence of a material element, called "limiter" (cf. fig. 1.3, left);

- Axisymmetric poloidal divertor configurations (which is the case of most of the largest tokamaks in the world and of the future ITER), where additional coils are used in which axisymmetric toroidal currents flow in order to produce a null in the poloidal magnetic field, which results in the presence of an X-point (cf. fig. 1.3, right). This offers the possibility to place the material elements further away from the plasma, which is better in terms of plasma-surface interaction [40].

The poloidal magnetic flux is often used in its normalized form $\psi_N \equiv \frac{\psi-\psi_{axis}}{\psi_{sep}-\psi_{axis}}$, where ψ_{axis} is the value of ψ on the magnetic axis, i.e. the innermost flux surface (which is in fact reduced to a curve) and ψ_{sep} its value at the separatrix. This way, $\psi_N = 0$ corresponds to the magnetic axis and $\psi_N = 1$ to the separatrix.

An important physical parameter is the so-called "safety factor" q [2], which quantifies the helicity of the field lines. More precisely, q is defined as the number of toroidal turns that a field line does while performing a single poloidal turn:

$$q(\psi) \equiv \frac{1}{2\pi} \oint_{\Gamma_\psi} \frac{1}{R} \frac{B_\varphi}{B_p} ds, \tag{1.10}$$

where R represents the major radius (cf. right plot in fig. 1.1) and Γ_ψ is the closed curve obtained by taking a "poloidal cut", i.e. a cut by a plane of constant φ, of the flux surface labelled by ψ. Of particular importance are the rational flux surfaces, i.e. the flux surfaces where q takes a rational value $q = m/n$ (with m and n integer numbers), in particular when m and n are small. We can remark that in poloidally diverted plasmas, since B_p has a null at the X-point, q diverges to infinity when approaching the separatrix. In order to quantify q at the edge of an X-point plasma, it is usual to take its value at $\psi_N = 0.95$, denoted q_{95}.

We need to define some more terms which will be employed below, namely:

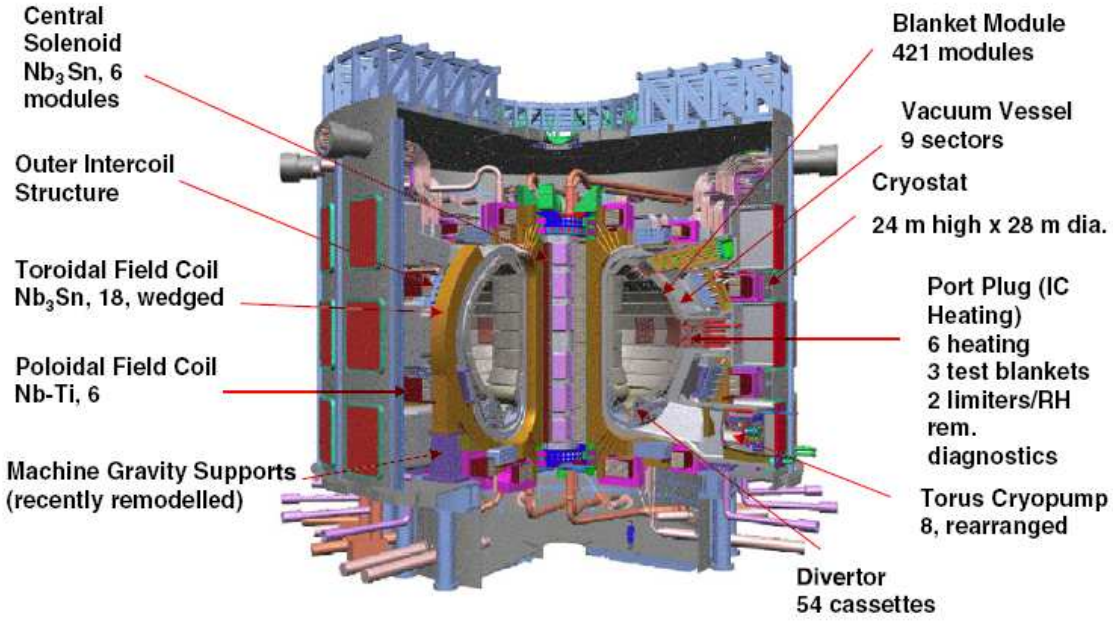

Figure 1.4: Cutaway of ITER with its major components indicated. From [7].

- Low Field Side (LFS) and High Field Side (HFS). These terms designate respectively the outer and inner sides of the tokamak, referring to the $1/R$ dependence of the toroidal magnetic field B_φ, which is thus stronger on the inner side than on the outer side.

- Banana particles [2]. Due to the $1/R$ dependence of B_φ, as a particle travels along a field line, it sees the amplitude of the magnetic field vary. If the ratio $v_\parallel/v_\perp$ of the parallel over perpendicular (to the field line) velocities of the particle is too small, the particle can be trapped on the LFS, in which case it describes an orbit which has the shape of a banana [2].

- Bootstrap current [2]. Due to the existence of banana particles, a radial pressure gradient results in a parallel current, called "bootstrap current". This effect is particularly important in transport barriers, where the radial pressure gradient is large.

1.3 ITER

The ITER tokamak [4, 5, 6], which is being built at Cadarache in the frame of a wide international collaboration, will be the leading experimental fusion reactor for the decades to come. Its main objective is to reach an amplification factor $Q = 10$ with a pulse duration of 400s. The ITER design is shown on fig. 1.4 and its principal parameters, together with those of Tore Supra and the Joint European Torus (JET) [2], which is presently the largest tokamak in the world, appear in table 1.3.

	Tore Supra	**JET**	**ITER**
Major radius R (m)	2.25	3	6.2
Minor radius a (m)	0.7	1.25	2.0
Plasma volume V (m^3)	25	155	830
Plasma current I_p (MA)	1.7	5-7	15
Toroidal field on axis B_t (T)	4.5	3.4	5.3
Pulse duration	minute(s)	$\sim$ 10s	400s
Type of plasma	$D-D$	$D-D$ / $D-T$	$D-T$
Fusion power P_{fus}	$\sim$kW	50kW / 10MW	500MW
Amplification factor Q	$<< 1$	~ 1	> 10

Table 1.1: Principal parameters for Tore Supra, JET and ITER.

1.4 Transport in tokamaks

Transport in tokamaks is a central subject since it determines the energy confinement time τ_E and plays a key role in the plasma density and temperature.

1.4.1 Parallel versus perpendicular transport

In the direction parallel to the magnetic field lines, in contrast with the perpendicular direction, particles are not confined by the magnetic field. Parallel transport is thus much more efficient than perpendicular transport. Physical quantities (density, temperature, pressure) consequently equilibrate much faster on flux surfaces than perpendicularly to them, i.e. radially. Therefore, it is common to describe the spatial dependence of physical quantities in terms of radial profiles (cf. fig. 1.5 for instance), and one is in fact interested mainly in the radial transport.

1.4.2 Drifts

We already mentioned that in a spatially non-constant magnetic field, charged particles have, on top of their fast gyromotion around field lines, a slower drift motion perpendicular to the field lines. Another drift occurs in presence of an electric field $\vec{E}$, called the "electric", or "$\vec{E} \times \vec{B}$" drift and denoted $\vec{v}_E$. Its expression is:

$$\vec{v}_E = \frac{\vec{E} \times \vec{B}}{B^2}. \tag{1.11}$$

This electric drift velocity will be mentioned again in section 6.3.3. Other drifts exist, such as the so-called "diamagnetic drift" in presence of a pressure gradient and "polarization drift" in a non-constant (spatially or temporally) electric potential field. These drifts are usually slower than the $\vec{E} \times \vec{B}$ drift.

1.4.3 Turbulence

In present tokamaks, the radial transport is typically due to turbulence. Collective plasma instabilities indeed develop, due to the sources of free energy constituted by the radial

gradients of the physical quantities. They result in a turbulent state where electric (or electromagnetic) fluctuations induce a radial transport, in general through the $\vec{E} \times \vec{B}$ drift (but other drifts can also play a role in the transport, and in the case of magnetic fluctuations, parallel transport along perturbed magnetic field lines can also contribute significantly to the radial transport). This turbulent radial transport is by orders of magnitude more efficient than the one occuring due to collisions.

1.5 The H-mode and Edge Localized Modes

1.5.1 The H-mode

It was discovered in the German tokamak ASDEX [8], in the beginning of the 80's, that under certain conditions (typically above a certain threshold in the injected power P_{inj}), a transition occurs in the plasma, resulting in a spectacular improvement of the confinement. This mode was given the name of "H-mode", the H standing for "High confinement", as opposed to the "L-mode", with the L for "Low confinement", which was the reference mode until then. In H-mode, the energy confinement time increases by typically a factor of 2 with respect to the L-mode. The H-mode is characterized by a transport barrier, i.e. a region where the radial transport is reduced, located at the edge of the plasma (typically between $r \simeq 0.95$ and $r = 1$, r being the normalized minor radius). Experiments show that this is due to a reduction of the turbulence. Due to the reduced transport, the radial gradients of the plasma density and (ion and electron) temperatures in the Edge Transport Barrier (ETB) region are enhanced. Elsewhere, there is almost no change in the gradients (a property often referred to as "profile stiffness"). Thus, at the L to H transition, profiles are like put on a "pedestal" (see fig. 1.5). In the last 20 years, the H-mode was obtained in many tokamaks and was extensively studied. It is now the reference operational mode for ITER. However, it is remarkable that no model has been able, up to now, to reproduce the L to H transition.

1.5.2 Edge Localized Modes

Phenomenology

As can be seen on fig. 1.6, just after the L to H transition, one generally observes a series of bursts on the D_α signal[1], whose frequency decreases in time. These bursts are associated to so-called "type III Edge Localized Modes (ELMs)". If P_{inj} is large enough, type III ELMs are followed by a period of time where the D_α signal is quiet, which is called the "ELM-free H-mode". A further increase in P_{inj} leads to large, quasi-periodic bursts on the D_α signal, which are the mark of "type I (or giant) ELMs".

Good reviews on ELMs can be found in [10, 11, 12, 14, 20]. Here, we are particularly interested in type I ELMs. Indeed, the type I ELMy H-mode has been chosen as the

[1]The D_α signal gives a measure of the emission of the α ray of deuterium which is associated to its recycling, i.e. its coming back into the plasma after having reached the PFCs. The D_α signal is therefore a measure of the recycling, which is itself strongly correlated to the particle flux coming out from the plasma and reaching the PFCs.

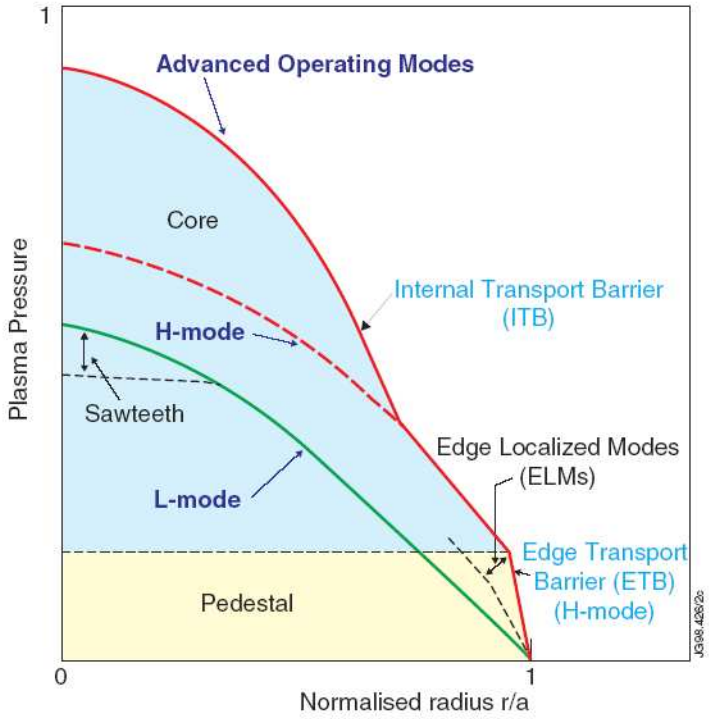

Figure 1.5: Typical pressure profiles for the different operating modes in a tokamak.

baseline mode of operation for ITER, due mainly to its good confinement properties [35]. The main experimentally observed characteristics of type I ELMs are the following:

- They expulse a certain amount of particles and energy from the edge plasma (by "edge" we mean here edge of the region inside the separatrix), resulting in a collapse of the profiles, as can be seen on fig. 1.7. Following this collapse, the profiles are re-built thanks to the energy and particle fluxes coming from the core as well as from local power sources and particles recycling and/or injection, until the next ELM happens.
- They are associated to magnetic fluctuations (observable with magnetic pick-up coils located in the vacuum vessel [but away from the plasma]).
- Their typical duration is of the order of 200μs.
- They are localized mainly on the LFS.

From the point of view of PFCs, ELMs in general and type I ELMs in particular are synonyms of large transient heat and particles loads. On fig. 1.8, the impact of type I ELMs on PFCs appears very clearly. As explained in section 1.6.1, these loads can cause damage to the PFCs and they are the reason for the need to avoid type I ELMs in ITER.

Magnetohydrodynamics origin of the ELMs

On the theoretical viewpoint, type I ELMs have been found to be triggered by MagnetoHydroDynamics (MHD) instabilities [15]. It is important to detail this somewhat,

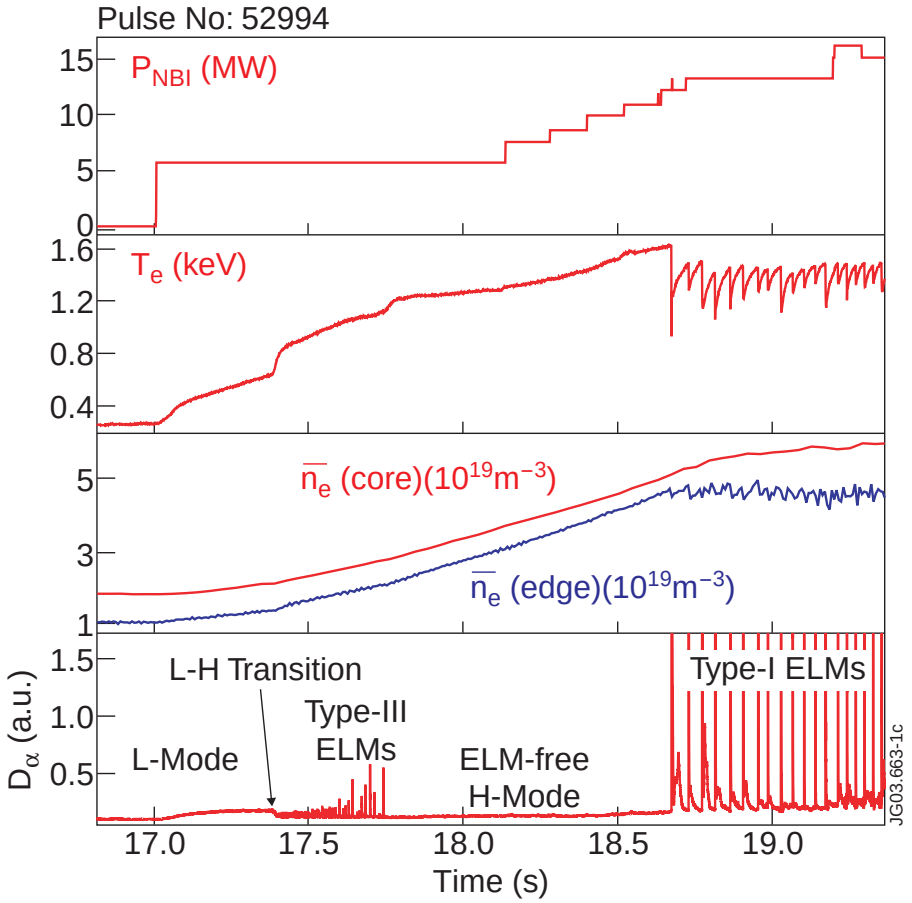

Figure 1.6: Overview on a JET discharge displaying the typical sequence of events during the gradual increase in the injected power. From [9].

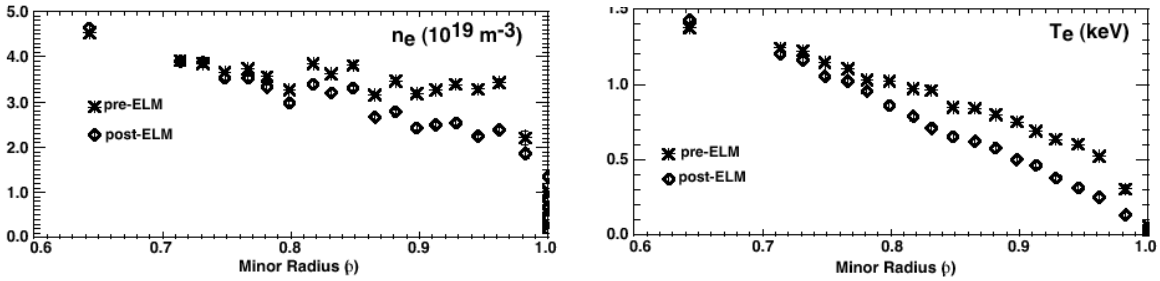

Figure 1.7: Profiles of the electron density (left) and electron temperature (right) just before and just after a type I ELM.

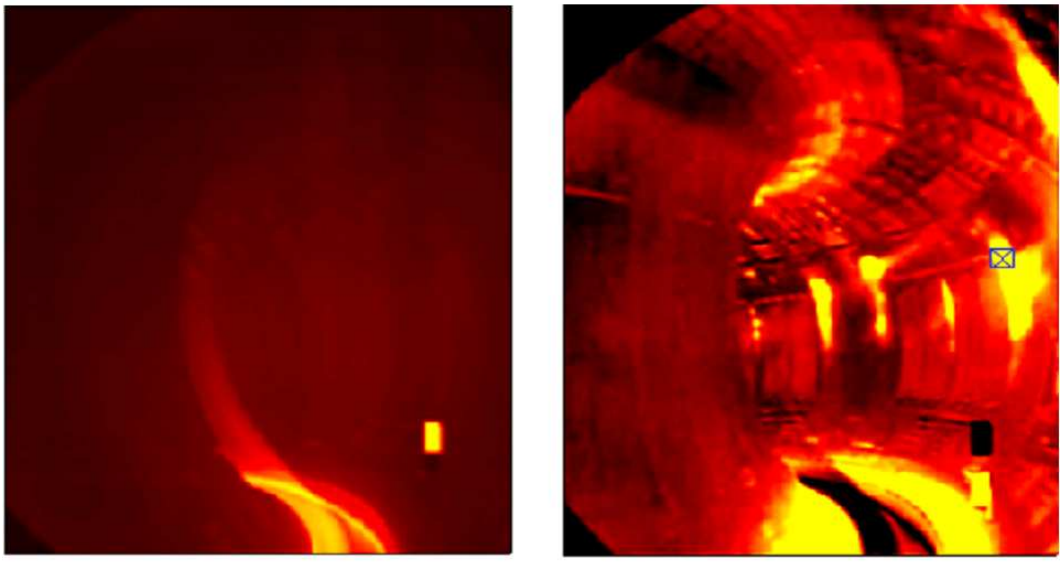

Figure 1.8: Photographs of the vacuum vessel of the JET tokamak taken in visible light before (left) and during (right) an ELM. Visible light comes typically from the recycling deuterium (D_α ray) or from light impurities, so that the patterns observable on this figure are linked to recycling and, indirectly, to the heat flux deposition (which is responsible for the release of light impurities from the plasma facing components). (courtesy Ph. Ghendrih)

because it will be useful in order to understand how ELMs control by Resonant Magnetic Perturbations (RMPs) works (or is thought to work, at least in certain cases - see section 2.2.2).
Let us first explain what MHD is. Generally speaking, there are several possible levels of description of a plasma. Due to the very low collisionality of tokamak plasmas, kinetic models, based on the Vlasov equation, are the most relevant ones. The gyrokinetic model, in which the dimensionality is reduced from six to five degrees of freedom by means of an averaging with respect to the gyromotion of the charged particles, is presently the subject of important efforts in the community. However, such models are hardly possible to tackle analytically, which is why numerical codes are being developed, but these codes also require large resources, due to the large number of degrees of freedom. A less refined but less demanding description of the plasma is obtained when taking the successive moments of the Vlasov equation with respect to the particles velocity, which results in a fluid model. It is common, in particular in order to study the anomalous transport due to plasma turbulence, to use a description that considers the electrons and the ions as two separate fluids. But the model can be simplified further, so as to become a single-fluid model, called the MHD model. Even though the MHD model does not describe many important aspects of the plasma dynamics, it is still very utilized and is of great practical interest. In particular, this model is able to describe (at least partly) most of the main fast, large scale instabilities that are susceptible to occur in tokamaks and therefore limit the operational space in which to run them. Thus, the basic equilibrium of a tokamak plasma is in general calculated in the frame of MHD[2].

Ideal MHD [13] is the reduction of the MHD model where the plasma electrical resistivity is assumed to be null. In ideal MHD, the stability of the plasma can be studied through a so-called "energy principle" that we will briefly explain now. Linearizing the ideal MHD equations around an equilibrium state, all the perturbed quantities (magnetic field, current density, etc.) can be expressed as a function of the spatial displacement field of the plasma, $\vec{\xi}$, with respect to its equilibrium position. It is thereby possible to define a potential energy δW that is a function of $\vec{\xi}$ only. The energy principle simply states that the plasma is stable if δW is positive for any possible $\vec{\xi}$. The potential energy is calculated in the form of an integral over the whole domain of the physical problem, which in general comprises a plasma region surrounded by a vacuum region, itself surrounded by a wall which is assumed to have an infinite electrical conductivity. The potential energy can be decomposed in the following way [13]:

$$\delta W = \delta W_F + \delta W_S + \delta W_V, \tag{1.12}$$

where δW_F (resp. δW_S, resp. δW_V) denotes the contribution from the plasma ("F" stands for "fluid") (resp. plasma-vacuum interface ["S" standing for "surface"], resp. vacuum). We will not give the expressions for δW_S or δW_V, the interesting elements for our purpose being contained in the expression of δW_F:

[2]The Grad-Shafranov equation [2], which is the classical equation used in order to calculate the plasma equilibrium, is derived from the MHD equations.

$$\delta W_F = \frac{1}{2}\iiint_{plasma} dV\left[|\vec{Q}_\perp|^2 + B^2|\vec{\nabla}\cdot\vec{\xi}_\perp + 2\vec{\xi}_\perp\cdot\vec{\kappa}|^2 + \gamma p|\vec{\nabla}\cdot\vec{\xi}|^2 - 2\left(\vec{\xi}_\perp\cdot\vec{\nabla}p\right)\left(\vec{\kappa}\cdot\vec{\xi}_\perp^*\right) - j_\parallel B^{-1}\left(\vec{\xi}_\perp^*\times\vec{B}\right)\cdot\vec{Q}_\perp\right]. \quad (1.13)$$

In this expression, the integral is taken over the plasma volume, the indexes $\perp$ and $\parallel$ designate the components perpendicular and parallel to the equilibrium magnetic field, $\vec{Q}$ is the linear perturbation of the magnetic field $\vec{B}$, $\vec{\kappa}$ is the curvature of the equilibrium magnetic field ($\vec{\kappa} \equiv (\vec{b}\cdot\vec{\nabla})\vec{b}$, with $\vec{b} \equiv \vec{B}/B$), γ (=5/3) is the ratio of specific heats of the plasma, p is the plasma pressure, and $\vec{j}$ is the current density. Finally, stars designate complex conjugate quantities (all quantities are real *a priori*, but the expression presented here is extended to cases where a Fourier transform is used). The energy principle provides an important insight on the physics at play in MHD instabilities in the sense that it allows one to identify clearly the sources of instability. Indeed, the first three terms under the integration symbol are positive definite, meaning that their contribution is always stabilizing, whereas the last two terms are susceptible to be negative, meaning that they can lead to an instability. Looking at the expression of those last two terms, the possible sources of instability turn out to be the pressure gradient[3] and the parallel current density.
The evolution of research on linear ideal MHD related to type I ELMs is well described in [15]. The present model is the so-called "Peeling-Ballooning" (P-B) model, which deals with instabilities that are driven by both the parallel current density[4] (peeling component) and the pressure gradient (ballooning component) in the pedestal. This model provides stability diagrams such as the one shown in fig. 1.9, where the stable and unstable regions are shown in the (α, j_{ped}) space of parameters, α being the normalized pressure gradient in the pedestal and j_{ped} the parallel current density in the pedestal. Many experiments (see in particular [16]) have confirmed that type I ELMs are triggered when the plasma reaches the boundary between the stable and unstable zones in such diagrams.

1.6 ELMs control

1.6.1 The necessity of ELMs control for ITER

Estimation of the type I ELM size in ITER

As mentioned above, the type I ELMy H-mode is the reference scenario for ITER [35]. Studies have been done in the past years in order to estimate the ELMs size (from now

[3]Typically, the pressure gradient term is negative (destabilizing) on the LFS (where the pressure gradient and magnetic curvature point towards the same direction) and positive (stabilizing) on the HFS, explaining the tendency of some MHD instabilities to present a so-called "ballooning" aspect, i.e. to be localized on the LFS.

[4]It should be noticed that in the pedestal, the parallel current is essentially constituted by bootstrap current.

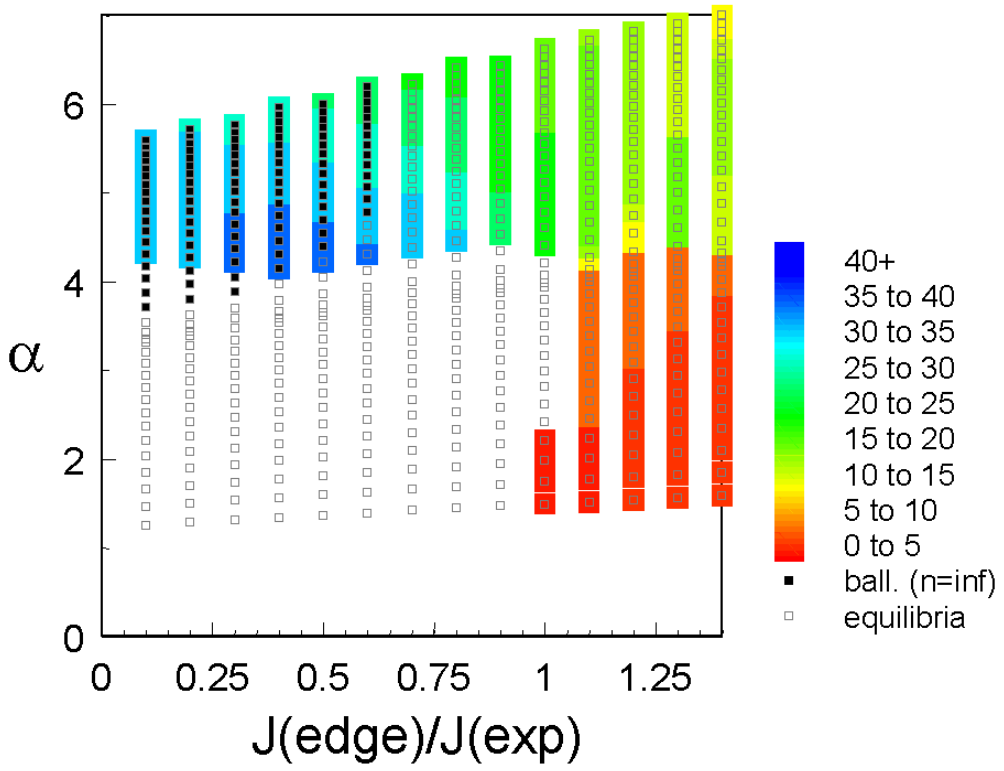

Figure 1.9: Example of the MHD P-B stability as a function of the normalized radial pressure gradient in the pedestal (α) and the current density in the pedestal normalized to its experimental value for a JET H-mode discharge. Each square marks an equilibrium for which the stability was evaluated. The small black squares indicate instability of $n = \infty$ (n being the toroidal mode number of the mode - and $n = \infty$ thus corresponding to modes infinitely localized perpendicularly to the equilibrium magnetic field) ballooning modes while the large coloured squares indicate instabilities with a finite n, the colour depending on the value of n. From [15].

on, "ELMs" will always mean "type I ELMs", unless precised), i.e. the amount of energy expelled from the confined region during an ELM, ΔW_{ELM}, in ITER [17]. The estimation is based on an experimental approach. Data was collected from the largest tokamaks in the world in order to determine the physical parameters that have an influence on the ELM size. A clear scaling of the ELM size normalized to W_{ped}, the amount of energy "stored in the pedestal"[5], with the plasma pedestal electron collisionality ν_e^* (defined as $\nu_e^* \equiv \frac{\pi R q_{95}}{\lambda_{e,e}}$, where $\lambda_{e,e}$ is the electron-electron collision mean free path [2] calculated with the values of the pedestal parameters) was found and is illustrated on fig. 1.10. As one can see on this figure, the ELM size increases as collisionality decreases. At the ITER value for ν_e^*, which is about 0.1, the normalized ELM size is of about 15%, which corresponds to $\Delta W_{ELM} \simeq 17$MJ (since $W_{ped} \simeq 110$MJ in ITER).

Maximum tolerable type I ELM size in ITER

In parallel, work was done in order to estimate the consequences of the ELMs on the ITER PFCs, depending on their size [18, 19]. The conclusion from Federici et al. [18] was that the maximal tolerable size for the ELMs[6] was of about 3 or 4MJ. This was already far below the expected 17MJ, but recent work [19] reduces even more the tolerable ELM size, now considered to be below 2MJ.

The conclusion is that type I ELMs are unacceptable in ITER, which is in obvious contradiction with the fact to take the type I ELMy H-mode as the reference scenario.

1.6.2 Possible solutions to the problem of ELMs

Benefic effects of type I ELMs

Before describing the different possible solutions that have been imagined in order to solve the problem of ELMs in ITER, it is important to mention that, although ELMs are nefast to PFCs, they have certain benefic effects. In particular, by transiently expelling large amounts of particles from the confined plasma, they maintain a certain level of density and impurity transport at the edge. Without ELMs, it would be difficult to prevent the density from rising too much[7] and the impurities (and also fusion "ashes", i.e. α particles) to accumulate in the core plasma[8]. Furthermore, the type I ELMy H-mode, in spite of the ELMs, presents good confinement properties and a good level

[5] defined as $W_{ped} \equiv \frac{3}{2} n_{e,ped}(T_{e,ped} + T_{i,ped}) V_{plasma}$, where $n_{e,ped}$ (resp. $T_{e,ped}$, resp. $T_{i,ped}$) is the plasma density (resp. electron temperature, resp. ion temperature) at the top of the pedestal and V_{plasma} is the volume of the confined plasma

[6] By "tolerable size" we mean the size allowing the divertor to survive for about 3000 discharges ($\sim 10^6$ type I ELMs) at full injected power. This duration corresponds to the ITER divertor replacement schedule.

[7] A too high density is a well known cause of disruption, i.e. abrupt, undesired, termination of the discharge.

[8] Impurities are species others than the species "normally" present in the plasma (i.e. deuterium, tritium and α particles), for instance carbon, nickel or oxygen. In general, they come from the PFCs, and are nefast to the plasma because they disperse a large amount of power by radiation (especially the heavy impurities), thereby cooling down the plasma (and in some cases leading to a radiative collapse of the plasma), and also they dilute the "fuel", i.e. the deuterium and tritium mixture, reducing the fusion power. The same problems exist with α particles.

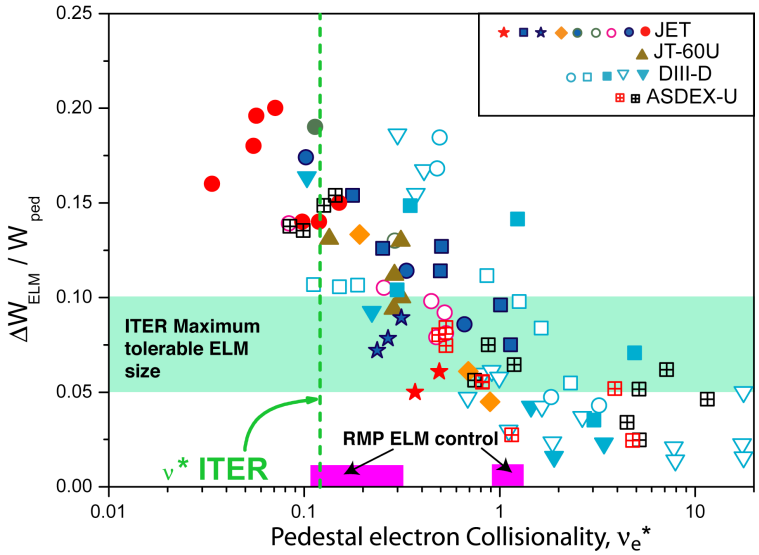

Figure 1.10: Typical amount of energy expelled during a type I ELM nomalized to the pedestal energy, as a function of the pedestal electron collisionality, for different large tokamaks. The domains of collisionality explored during the DIII-D ELMs control experiments (see chapter 2) are shown in purple. From [29].

of fusion power, which is the reason why it was chosen as the reference scenario for ITER.

Looking for a way to avoid the ELMs, one should thus make sure that a sufficient level of particle transport will still exist and that the plasma performances will not be degraded.

Passive or active ELMs control methods

Now, there are two possible approaches to try and avoid the ELMs. The first one, which we could call "passive control approach", consists in looking for another regime in which to run ITER that would offer similar performances to the type I ELMy H-mode but would not damage the PFCs so drastically. The second one, the "active control approach", consists in keeping the type I ELMy H-mode as the ITER baseline scenario, but controlling the ELMs (i.e. either reducing their size or totally suppressing them) by dedicated means. Several variations of these two concepts have been investigated and are reviewed in [14, 20, 35]. Different high confinement scenarios without type I ELMs have been found in present machines. However, the extrapolation of these regimes to ITER is questionable since the operational windows are usually very narrow and do not match ITER relevant parameters. Active ELMs control methods are thus likely to be required in ITER. The two main candidates are ELMs triggering by pellet injection [21] and ELMs mitigation by Resonant Magnetic Perturbations (RMPs), the central subject of the present manuscript. It has been decided to implement both systems in ITER.

1.7 ELMs control by Resonant Magnetic Perturbations

We now focus on the central subject of this work: ELMs control by RMPs. In this section, we explain the "historical" genesis of the concept.

1.7.1 Degrading the ETB to suppress ELMs

The underlying idea is that, according to the ideal MHD theory of ELMs[9] presented in section 1.5.2, ELMs occur because the Edge Transport Barrier (ETB) of the H-mode is "too efficient", i.e. the pressure gradient, and hence bootstrap current density, can reach too large values. If, by some process, transport in the ETB could be enhanced enough that the plasma would remain in the stable region with respect to P-B instabilities (however without loosing all the benefit of the ETB if possible!), ELMs could be avoided[10].

1.7.2 Confinement degradation by radial RMPs

One possible way to enhance the radial transport in a tokamak is to produce magnetic perturbations that possess a radial component. That way, the very efficient parallel transport contributes to the radial transport. It is known in particular that radial RMPs ("resonant" means constant along field lines on a given flux surface, called "resonant surface"), can "tear" the nested flux surfaces, creating so-called "magnetic islands" [2], a schematic example of which can be seen on fig. 1.11. When a magnetic island is present inside the plasma, the radial transport is short-circuited, across the island width, by the strong parallel transport. Thus, in terms of transport, the annulus of plasma located in the region of the island is effectively "lost", because it offers almost no resistance to radial transport. That is why, usually, one tries to avoid large magnetic islands inside the plasma. However, for our purposes, magnetic islands could be beneficial.

1.7.3 Ergodic divertors

Islands overlapping and ergodic magnetic field

It can happen that several islands chains exist in the plasma, centered on distinct resonant surfaces. This is the case in fig. 1.12, which presents three Poincaré plots done for RMPs containing only $(m = 2, n = 1)$ and $(m = 3, n = 2)$ components, m (resp. n) being the poloidal (resp. toroidal) mode number, which create islands chains on the $q = 2$ and $q = 3/2$ surfaces. The three Poincaré plots correspond to three amplitudes of the RMPs, more precisely there is an increase of the RMPs by a factor 2 between the top and the middle plots as well as between the middle and the bottom plots. It can be seen that for small enough RMPs, the islands are well separated, but that increasing the RMPs, the islands grow until they "overlap". Then, magnetic field lines start to behave in a chaotic

[9] which was, as mentioned above, validated by many experiments

[10] An important remark here is that several of the high confinement scenarios alternative to the type I ELMy H-mode seem to rely on the same principle.

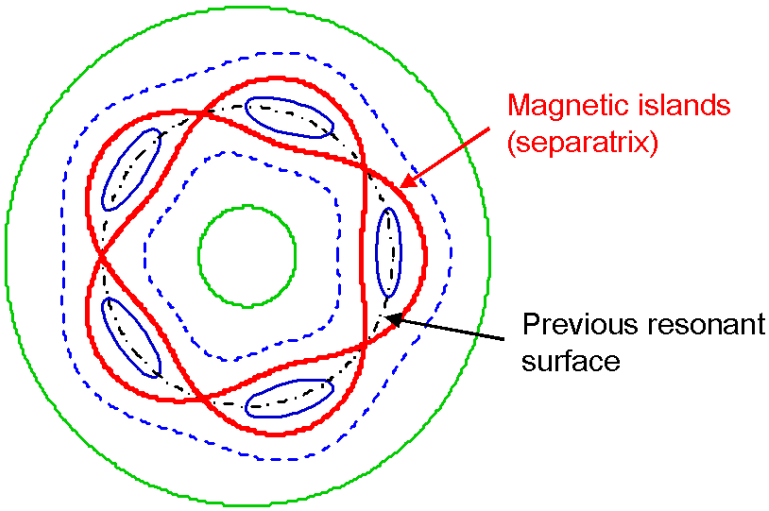

Figure 1.11: Schematic poloidal cut of a circular plasma showing several flux surfaces. An islands chain appears with its separatrix in red, while the position of the previous resonant surface (before the islands chain existed) is shown by a dash-dotted black line.

manner, all closed flux surfaces between the two resonant surfaces being destroyed[11]. One will also often find the words "stochastic" and (for instance in the rest of this manuscript) "ergodic", which are used with almost no distinction in the fusion community, although they have a different mathematical meaning [43]. The degree of islands overlapping is quantified by the so-called "Chirikov parameter", σ_{Chir}, which, in-between two islands chains of radial half-widths δ_1 and δ_2 separated by a radial distance Δ_{12}, is defined as:

$$\sigma_{Chir} \equiv \frac{\delta_1 + \delta_2}{\Delta_{12}}. \tag{1.14}$$

The criterion for ergodicity to occur is therefore $\sigma_{Chir} \geq 1$, roughly.

In the past, several machines have tested the concept of "ergodic limiter" (see the review paper [33]). This is still the case today in the TEXTOR tokamak. The idea is to use a specific set of coils to produce radial RMPs at the edge of the plasma, so as to create an ergodic region, for the purpose of improving the plasma-wall interaction with respect to a standard limiter case.

[11]This description is somewhat simplified. In fact, before the islands overlap, there are higher order islands chains (i.e. islands chains that appear at flux surfaces that are not resonant with the imposed RMPs) growing in-between them, as can be seen in fig. 1.12 (in particular on the middle plot). This process is described in [43]. The image of two "primary" islands chains (such as the $(m = 2, n = 1)$ and $(m = 3, n = 2)$ one on fig. 1.12) growing in the middle of nested flux surfaces until they overlap is thus incorrect, although it is intuitively helpful.

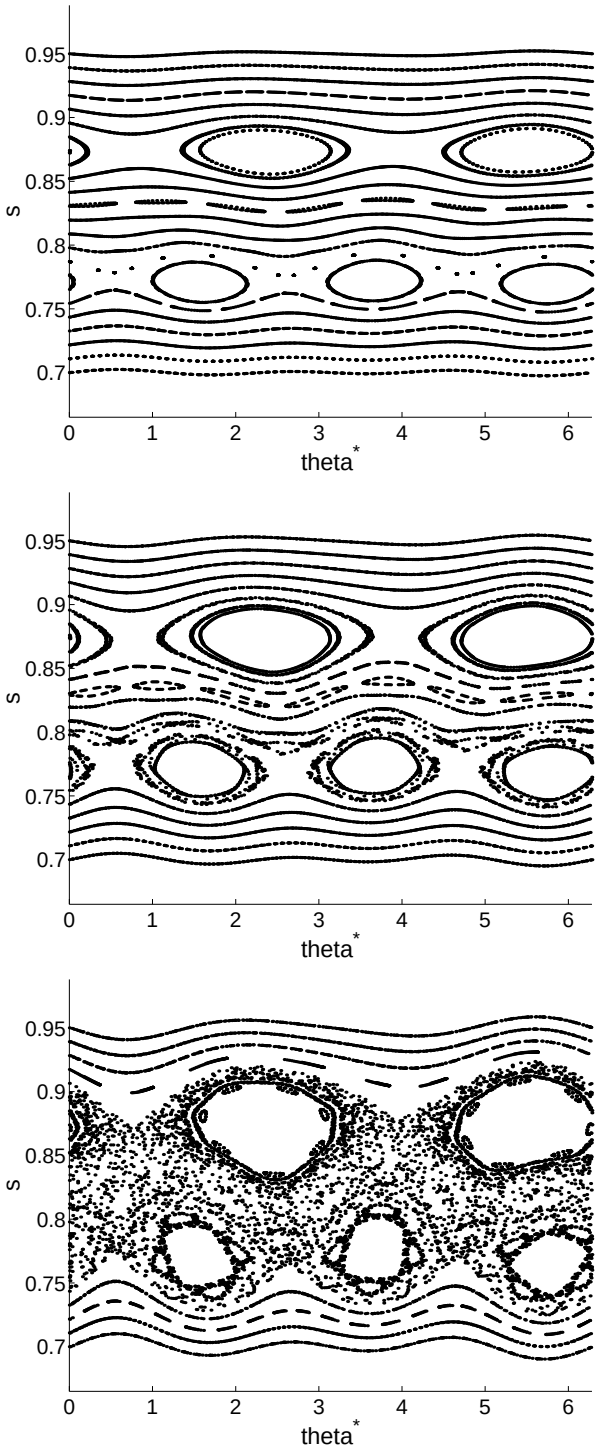

Figure 1.12: Poincaré plots obtained by field line integration. θ^* is a poloidal coordinate and s a radial coordinate. The RMPs only have an $(m = 2, n = 1)$ and an $(m = 3, n = 2)$ components, which create two islands chains on the $q = 2$ and the $q = 3/2$ surfaces. Between the top and middle plots, as well as between the middle and bottom plots, the amplitude of the RMPs is doubled.

1.7.4 Synergy between the axisymmetric poloidal divertor and the ergodic divertor

As is well known (see for instance [2] or appendix A), for a given RMPs amplitude, the islands widths scale as $(q')^{-1/2}$, q' being the magnetic shear, i.e. the radial derivative of the safety factor q, while the distance between islands chains scales as $(q')^{-1}$. The Chirikov parameter therefore scales as $(q')^{1/2}$, meaning that a high magnetic shear is favorable for ergodization. As mentioned above, for poloidally diverted plasmas q tends to infinity when approaching the separatrix, and so does q'. The magnetic field at the edge is likely to be ergodized easily. Reference [24] provides a good illustration that a poloidally diverted plasma is more easily subject to edge ergodization than a plasma in limiter configuration.

1.7.5 Transport in an ergodic magnetic field

The main theoretically expected effect of the magnetic field ergodization on radial transport is an enhancement of the heat transport through the electrons [23], which travel along field lines much faster than the ions (at equal temperatures, their thermal velocity is larger than that of the ions by a factor $(m_i/m_e)^{1/2}$) and hence have larger parallel transport coefficients. This effect was verified experimentally in several devices, as reviewed in [33]. An increase in the density transport is also expected and was clearly observed experimentally [33], sometimes resulting in a "pump-out", i.e. a drop in the plasma density [34].

The conclusion of the above considerations is that it seems *a priori* worthwile trying to ergodize the magnetic field at the edge of an H-mode tokamak plasma in order to increase the pedestal transport and, hopefully, suppress type I ELMs. This was the statement of Grosman et al. in 2003 [62], who proposed to test the concept at DIII-D. In next chapter, we will see that this concept was indeed tested (and is still under investigation) at DIII-D and led to ELMs suppression, although not exactly in the way that was imagined by Grosman et al..

1.8 Construction of the present manuscript

The manuscript is constructed as follows. In chapter 2, we review the experimental and modelling findings from the DIII-D experiments using the so-called "I-coils" in order to mitigate the ELMs. These experiments are the departure point of the present work. In chapter 3, we describe the numerical tools that we developed in order to calculate and analyze the magnetic perturbations created by a given set of coils in a tokamak plasma and describe our results for the DIII-D I-coils. In chapter 4, we present recent experiments on ELMs mitigation by RMPs done at JET and MAST with the error field correction coils in which we participated and provided modelling support using the tools presented in chapter 3. In chapter 5, we report on our design study for ELMs control coils for ITER, the central piece of the present manuscript from a practical point of view. This design study was indeed used in the ITER design review process, which led to the decision to implement ELMs control coils in ITER (although it is not yet decided which design

will be chosen). Finally, in chapter 6, we present our modelling work for ELMs control experiments, using non-linear MHD numerical simulations, a necessary tool in order to understand the plasma response on the external RMPs and progress in the understanding of the physical mechanisms at play in ELMs control by RMPs.

Chapter 2

ELMs control with the I-coils at DIII-D

In 2003, DIII-D was the first tokamak to demonstrate the possibility to control the ELMs by imposing RMPs to the plasma, using a set of coils called the "I-coils". After having briefly described these coils, we will present the experimental phenomenology and describe the present status of modelling and interpretation of the experiments.

2.1 The DIII-D I-coils

The I-coils [41] are a set of 12 coils located inside the vacuum vessel ("I" standing for "internal") of DIII-D that were originally installed in order to stabilize the so-called "resistive wall modes" (see section 5.2 for a brief definition of these modes). A schematic view of the DIII-D I-coils appears on fig. 2.1. On this figure, one can see that there are two rows of six coils equally spaced toroidally, the two rows being symmetric with respect to the midplane (the horizontal plane containing the magnetic axis). The current direction alternates between one coil and the toroidally adjacent one. The coils thus produce mainly $n = 3$ magnetic perturbations. The coils are single turn loops which can carry up to 7kA (but in most of the past experiments, the current was limited to $\sim$ 4kA). There are two possible configurations: in the so-called "even parity" configuration, the upper and lower coils are in phase (i.e. the current flows in the same direction in upper and lower coils that are at the same toroidal location, those coils hence producing a radial magnetic perturbation pointing in the same direction), and in the "odd parity" configuration they are out of phase (or shifted by 60° toroidally, which is equivalent). Both these configurations have been used in the experiments, with different effects on the plasma, as will be detailed below. Calculations of the (vacuum-like, i.e. neglecting any plasma response) magnetic perturbations produced by both configurations are presented in chapter 3 and show that the even parity configuration produces stronger RMPs than the odd parity one.

2.2 The experiments

It is usual to distinguish the DIII-D ELMs control experiments with the I-coils according to the value of the electron pedestal collisionality ν_e^* (see section 1.6.1 for a definition

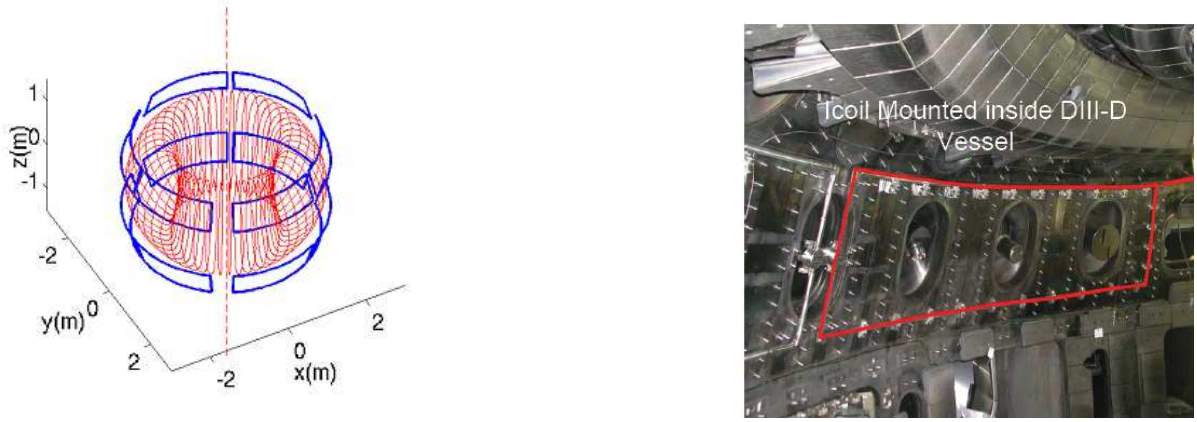

Figure 2.1: Left: 3D schematic view of the DIII-D I-coils together with the shape of a typical DIII-D plasma. Right: photograph taken inside the DIII-D vacuum vessel with one of the I-coils highlighted in red. From [36].

of ν_e^*). Indeed, as can be seen on fig. 1.10, two distinct domains of collisionality were explored: one "high collisionality" domain ($\nu_e^* \sim 1$) [25, 26, 27, 28] and one "low collisionality" domain ($\nu_e^* \sim 0.1$, close to the ITER forecasted value) [28, 27, 30, 31, 32]. These two domains were explored successively in time: the high ν_e^* one in 2004 mainly, and the low ν_e^* one since 2005. While the high ν_e^* experiments used the odd parity I-coils configuration, the low ν_e^* ones were mainly done with the even parity configuration[1]. In both domains, the I-coils were shown to have a very clear effect on the ELMs but the phenomenology was somewhat different. In the following sections, we describe the high and low ν_e^* experiments successively. Each time, we present the phenomenology in a first subsection and we summarize modelling results and elements of interpretation in a second subsection.

2.2.1 High collisionality experiments

As stated above, the high ν_e^* (~ 1) domain was explored first [25, 26, 27, 28], using the odd parity configuration of the I-coils, which produces much smaller RMPs than the even parity one (see section 3.2).

Phenomenology

On fig. 2.2 (second box from the top), it can be seen that ELMs suppression occurs immediately after the beginning of the I-coils pulse (or more precisely within 15ms, i.e. less than one typical ELM cycle), but that ELMs are not completely suppressed: some large D_α spikes remain. No difference was found between the remaining ELMs during the I-coils pulse and the ELMs before the I-coils pulse.

[1]It should be noticed that changing the I-coils configuration from odd to even (or *vice versa*) requires hardware modifications, so that the configuration cannot be changed between, for instance, two shots on the same experimental day. The fact that the high ν_e^* experiments were done in the less resonant odd parity configuration is only due to the fact that this was the configuration in which the I-coils were used at the time for other purposes. When ELMs control by RMPs became a high priority subject on DIII-D, the I-coils were switched to the even parity configuration and stayed that way until now.

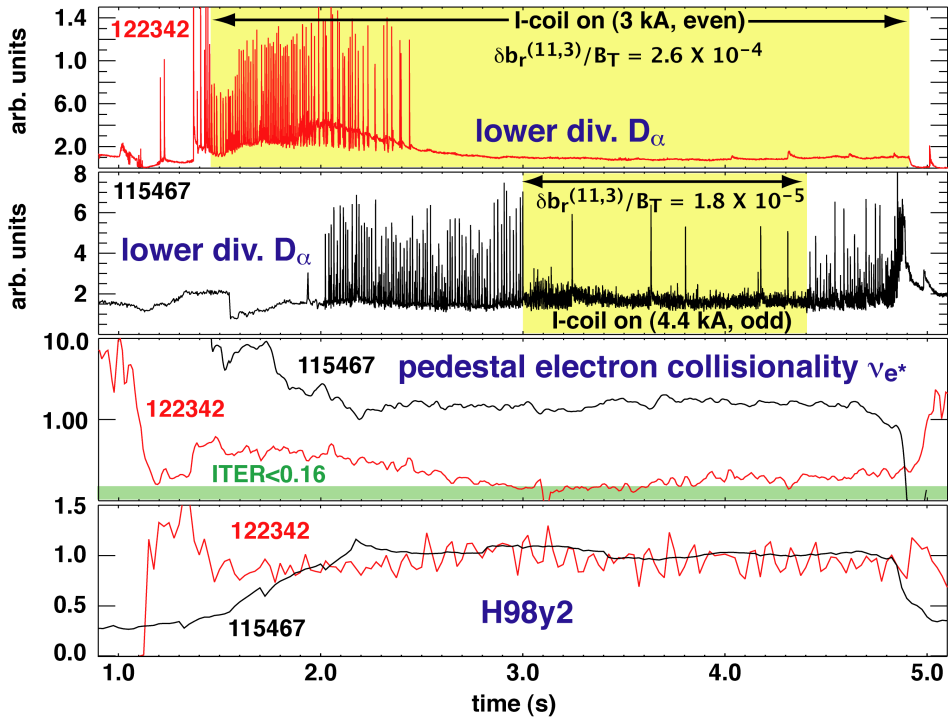

Figure 2.2: Experimental times traces for two shots: one at high ν_e^* (115467, black traces), the other at low ν_e^* (122342, red traces). From [29].

In-between the remaining ELMs, one can see that the D_α signal is not completely quiet. A detailed study reveals that the D_α signal in fact presents a bursty behaviour modulated with a coherent 130Hz envelope. This is associated with magnetic fluctuations (measured by magnetic probes) that also present a bursty behaviour with a coherent 130Hz envelope. The $H_{98(y,2)}$ confinement factor[2] (bottom box on fig. 2.2) remains constant during the I-coils pulse, meaning that the I-coils do not degrade the energy confinement. This is a strong point in favor of an application to ITER.
Consistently, the ETB does not seem to be affected by the I-coils and the temperature and density profiles exhibit only small changes between before and during the I-coils pulse, as can be seen on fig. 2.3.
On the other hand, the toroidal rotation profile shows a clear braking of the plasma due to the I-coils -see fig. 2.5- and in particular the toroidal rotation at the foot of the pedestal is reduced to zero.
Plasma current ramp experiments were done in order to investigate the dependence of the results on q_{95} [28]. It was found that ELMs suppression is only obtained for $3.5 \leq q_{95} \leq 3.9$ (with an optimal suppression at $q_{95} \simeq 3.7$)[3].
The magnetic footprints (i.e. regions of high heat and particle fluxes on the divertor plates, see section 4.2.2) exhibit a clear change between before and during the I-coils pulse, with a so-called "triple splitting" of the strike points [59].
Finally, it should be noticed that the plasma behaviour is sensitive to the toroidal phase of the magnetic perturbations from the I-coils (which can be changed by 60° by reversing the direction of current in all the coils).

Modelling and interpretation

The fact that the remaining ELMs during the I-coils pulse present no obvious difference with the "natural" ELMs suggests that the I-coils do not directly affect the ELMs, but only the transport in-between ELMs. Accordingly, a transport analysis [26] indicates that, in-between the remaining ELMs, an extra-transport mechanism (possibly related to the bursty D_α and magnetic fluctuations observed) is at play that slows down the recovery time of the profiles between ELMs and thus reduces the ELMs frequency.
Somewhat paradoxically, calculations of the vacuum-like magnetic perturbations produced by the I-coils in odd parity configuration, which are presented in chapter 3, show that the experimental q_{95} window for ELMs suppression corresponds to a "valley" in the odd parity I-coils magnetic perturbations spectrum, with edge ergodization occurring only on the $\sim 2\%$ most external flux surfaces[4]. This could mean that edge ergodization is not the reason of ELMs suppression. On the other hand, the observed drop in the toroidal rotation is consistent with a penetration of the RMPs, according to the classical theory of RMPs penetration into a rotating plasma (see chapter 6), and a modelling of the magnetic footprints [59] reveals that the observed splitting of the strike points is larger than the one calculated in the vacuum field hypothesis, meaning that there could

[2] which is defined as the ratio of the discharge thermal energy confinement time τ_{th} to a reference energy confinement time $\tau_{th,98y2}$ given by a scaling law that is derived from many experiments in present machines and used for ITER predictions, see [35]

[3] The resonant window was however observed to change with the shape and pedestal parameters of the discharge.

[4] in terms of square root of the poloidal magnetic flux

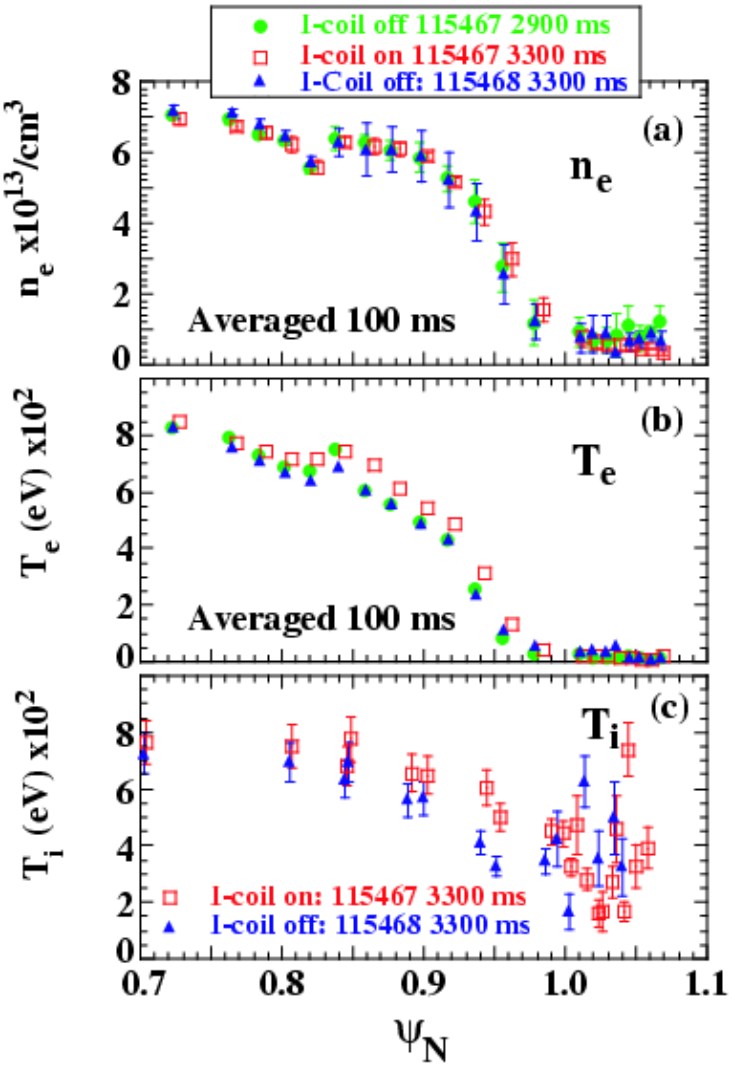

Figure 2.3: (a) Electron density (n_e) and (b) temperature (T_e) profiles averaged over 100ms before (at t = 2900ms) and during (at t = 3300ms) the I-coil pulse for shot 115467 and at t = 3300ms for shot 115468, where there was no I-coils pulse. (c) Ion temperature (T_i) profile at t = 3300ms for shots 115467 and 115468. From [28].

be a plasma response amplifying the external RMPs.
To finish, the sensitivity of the experimental results to the phase of the magnetic perturbations suggests that there exist intrinsic "error fields" (coming for instance from misalignments of the toroidal or poloidal field coils or currents flowing in the coils alimentation systems), which play a non negligible role.

2.2.2 Low collisionality experiments

Since 2005, DIII-D ELMs control experiments are devoted to the low ν_e^* domain [28, 27, 30, 31, 32], which is more relevant for ITER. In order to reach this domain, an active pumping by a cryopump is used so as to decrease the plasma density[5]. For the pumping to be efficient, the plasma shape is chosen such that the outer strike point is located near the entrance of the cryopump.

Phenomenology

The very first low ν_e^* experiments were done with the I-coils in odd parity configuration [28, 27]. An effect on the ELMs was observed, typically an increase in their frequency by a factor of about 2 and decrease in their amplitude by an order of magnitude. However, this configuration was not studied much.

Indeed, the I-coils configuration was soon switched to the even parity one, which is by far more resonant (see section 3.3.2). This configuration is being studied in detail since 2005 and we participated on-site to some of the experiments.
As can be seen on fig. 2.2 (top box), a complete suppression of the ELMs (no remaining spike on the D_α signal) occurs during the I-coils pulse but there is some delay with respect to the beginning of the I-coils pulse before the ELMs completely disappear. This is clearly different from the high ν_e^* experiments, were the suppression was incomplete but immediate[6].
One common point, however, between low and high ν_e^*, is that the $H_{98(y,2)}$ confinement factor (bottom box on fig. 2.2) is not affected by the I-coils.
Looking at the plasma profiles (fig. 2.4), a clear "pump-out" (decrease in n_e) due to the I-coils can be observed. The electron temperature (T_e) profile is flattened for a normalized poloidal flux ψ_N (used here as a radial coordinate) below ~ 0.97 and the T_e pedestal is conserved, with even a slight increase with the I-coils current $I_{I-coils}$ in the value of T_e at the top of the pedestal. Furthermore, the width of the pedestal decreases with increasing $I_{I-coils}$. There is thus a dramatic increase in $|\partial_r T_e|$ at the edge with $I_{I-coils}$. The ion temperature T_i is seen to increase with $I_{I-coils}$ across the entire plasma edge and $|\partial_r T_i|$ increases strongly for $\psi_N > 0.97$.
The toroidal velocity is also typically observed to increase at the edge in presence of the RMPs (fig. 2.5), oppositely to the high ν_e^* results. In the core, however, a drop in the rotation is still observed [36].

[5]Without pumping, all of the particles escaping the plasma tend to recycle, i.e. come back to the plasma, after reaching the plasma facing components, and density can thus not be decreased significantly.

[6]This could be due to the fact that the time of penetration of the RMPs into the plasma is longer in that case due to the smaller plasma resistivity, an effect which will be seen in the non-linear MHD simulations presented in chapter 6.

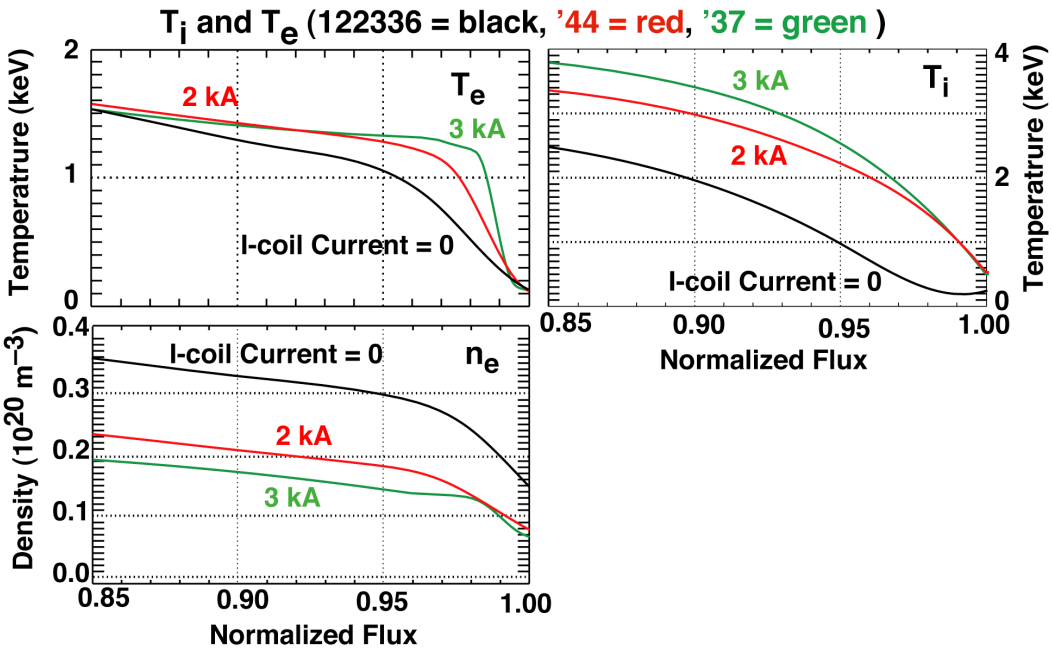

Figure 2.4: Plasma profiles from three low ν_e^* shots with three different values of $I_{I-coils}$: 0kAt (reference case, black traces), 2kAt (red traces) and 3kAt (green traces). The normalized poloidal flux is used as a radial coordinate. From [29].

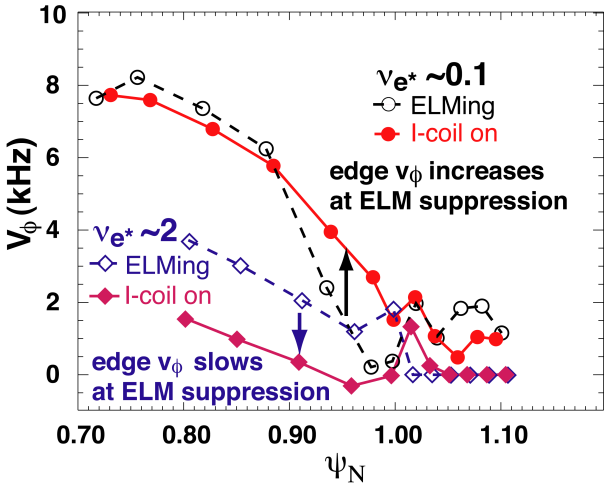

Figure 2.5: Toroidal rotation frequencies (in kilo-turns per second) for two shots: one at high ν_e^*, the other at low ν_e^*. From [29].

Modelling and interpretation

The magnetic modelling presented in chapter 3 shows that in these experiments, in the vacuum approximation, the magnetic field is ergodized over the $\sim 5\%$ most external flux surfaces[7], i.e. the ergodized region is about twice wider than the pedestal.
Another key modelling finding relative to these experiments is that, during the I-coils pulse, the plasma remains in the stable region with respect to Peeling-Ballooning (P-B) ideal MHD instabilities which are known to be the trigger of type I ELMs (cf. section 1.5.2) [36]. This can be seen on fig. 2.6, where the position of the plasma is represented in a diagram showing, as a function of the normalized radial pressure gradient in the pedestal α and normalized toroidal current density in the pedestal $j_{ped}/\langle j \rangle$, the growth rate of the most unstable P-B mode. The green circles correspond to the ELMs suppression phase during the I-coils pulse (for different shots with different values of $I_{I-coils}$) while the red diamonds are points from ELMing phases with the I-coils off (the values of α and $j_{ped}/\langle j \rangle$ being taken just before an ELM). One can clearly see that the I-coils push the plasma towards the stable region by reducing both α and $j_{ped}/\langle j \rangle$ (points with the smallest α and $j_{ped}/\langle j \rangle$ correspond to the highest values of $I_{I-coils}$)[8]. This result is, to a certain extent, consistent with the original idea of Grosman et al. [62] mentioned in section 1.7: RMPs can modify the pressure profile at the edge of an H-mode plasma in such a way that P-B modes remain stable. However, what had been imagined was that the reduction in α would come mostly from a reduction in $|\partial_r T_e|$, accordingly to the theory of transport in an ergodic magnetic field (see section 1.7.5). This is not what happens in reality, the reduction in α actually coming from the strong pump-out (which is nonetheless also an expected effect of the edge ergodization).
Several modelling works were dedicated to numerically calculating the electron heat transport in the magnetic field perturbed by the I-coils (always in the vacuum approximation), assuming a fixed density [61, 37, 38, 39]. The calculated radial electron heat conductivity was larger than the one deduced from experimental measurements by typically two orders of magnitude ($\chi_e^{calc} \simeq 20m^2/s$, $\chi_e^{exp} \simeq 0.2m^2/s$), unless an expression including a flux limiting term was used for the parallel electron heat conductivity $\chi_{e,||}$ [61, 39, 40]:

$$\chi_{e,||} = \frac{\chi_{e,||}^{SH}}{1 + \lambda_{e,e}/(\alpha_e L_T)}, \tag{2.1}$$

where $\chi_{e,||}^{SH}$ is the classical Spitzer-Härm parallel electron thermal conductivity [40] ($\chi_{e,||}^{SH}[m^{-1}s^{-1}] \simeq 1.6 \cdot n_e[10^{19}m^{-3}] \cdot V_{th,e}[ms^{-1}] \cdot \lambda_{e,e}[m]$, with $V_{th,e}$ the electron thermal velocity), $\lambda_{e,e}$ is the electron collisional mean free path, L_T is the typical parallel electron temperature gradient and α_e is a numerical coefficient. This type of expression is employed in cases where the collisionality is small and where the condition of validity of the Sptizer-Härm calculation, $\lambda_{e,e} << L_T$ is susceptible to be violated. Its effect is to avoid unphysically

[7] in terms of square root of the poloidal magnetic flux

[8] On fig. 2.6, one can remark, however, that the growth rate of the most unstable P-B mode remains positive, even for the points corresponding to ELMs suppression. In fact, a positive growth rate does not necessarily mean that the plasma is unstable. Indeed, there exists a phenomenon of stabilization due to the so-called "diamagnetic drift velocity" [3] $\vec{v}_{*e} = \frac{\vec{\nabla} p_e \times \vec{B}}{e n_e B^2}$. The stabilization occurs when the growth rate γ of the P-B mode is smaller than (half of) the diamagnetic frequency $\omega_{*e} \sim v_{*e}/2\pi a$ (a being the plasma minor radius), which explains the choice of normalization for γ and the dashed black line on fig. 2.6.

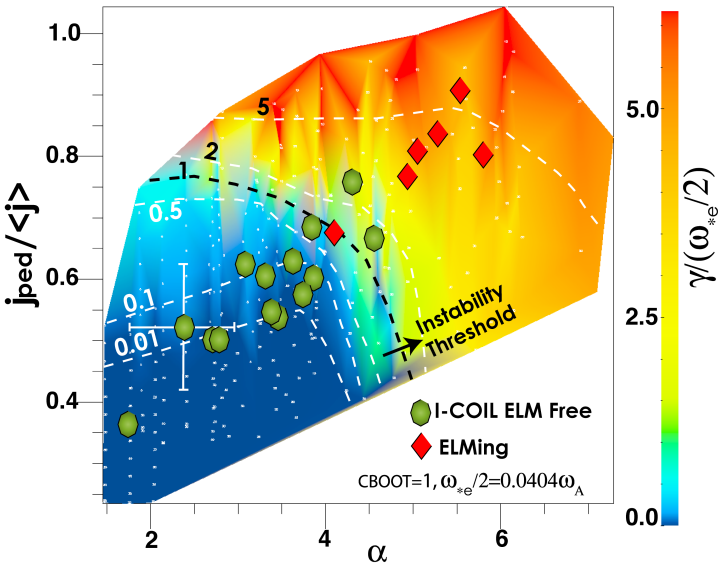

Figure 2.6: Position of the plasma in a diagram showing, as a function of the normalized radial pressure gradient (α) in the pedestal and normalized toroidal current density in the pedestal ($j_{ped}/\langle j \rangle$), the growth rate of the most unstable peeling-ballooning mode (γ) normalized to half the electron diamagnetic drift frequency (ω_{*e} -see footnote for an explanation). Taken from [36].

large heat fluxes which would be obtained using $\chi^{SH}_{e,||}$. Another possible reason for the discrepancy between modelled and experimental radial electron heat conductivities could be that the vacuum approximation is not correct and that the plasma reacts so as to screen the magnetic perturbations from the I-coils. Addressing this point is one of the main motivations of the work presented in chapter 6. However, to date, no definitive answer can be given.
Fewer modelling works exist for the density transport. Tokar et al. [39] find that the parallel transport along the field lines could be responsible for the observed pump-out. In section 6.3, we present another transport mechanism, based on convective cells induced by the I-coils at the edge of the plasma, which could also be playing a role in the pump-out.

2.3 Summary

ELMs suppression was obtained at DIII-D using the I-coils, both at high and low collisionality.

At high collisionality, the weakly resonant odd parity configuration of the I-coils (see next chapter) was used. ELMs suppression was immediate but not complete: some ELMs remained. In between the remaining ELMs, small fluctuations with a coherent 130Hz envelope were seen on the D_α signal and magnetic measurements. No clear effect on the density and temperature profiles was observed, but there was a significant drop in the plasma rotation. The interpretation of these results is that the I-coils enhance the

transport at the edge of the plasma (which is possibly linked to the observed magnetic fluctuations), making the time for recovery of the profiles after an ELM crash longer. The effect of the I-coils on the rotation and analysis of the magnetic footprints suggest that RMPs penetrate into the plasma and are even possibly enhanced by plasma effects.

At low, ITER relevant, collisionality, a complete but not immediate ELMs suppression was obtained, using the much more resonant even parity I-coils configuration (which is shown, in next chapter, to ergodize the magnetic field at the edge in the vacuum approximation). It is associated to a clear pump-out of the plasma density, while T_e is not significantly affected and T_i raises. The plasma rotation is decreased in the core but enhanced at the edge. MHD stability calculations show that in presence of the I-coils perturbation, the plasma remains stable with respect to P-B modes, explaining the suppression of the ELMs. The effect of the I-coils on profiles has been the object of several modelling works. The small effect on T_e is in disagreement with the heat transport simulations taking the magnetic perturbations to be as in vacuum (which predict a large drop of T_e), unless a flux limited expression is used for the parallel heat conductivity. The density pump-out could come from parallel transport along the perturbed field lines and/or the generation of convective cells by the I-coils (presented in section 6.3).

Chapter 3

The ERGOS suite of codes for RMPs analysis and calculations for the DIII-D reference case

3.1 Motivation

The success of the DIII-D experiments on ELMs control with the I-coils motivated the decision to focus the present work on the subject of ELMs control by RMPs. Our first objective was to propose a design for ELMs control coils for ITER, using DIII-D as a reference. To do this, a natural first step consisted in developing a suite of numerical tools, that we called "ERGOS" (for ERGOdic Spectrum), in order to calculate and study the magnetic perturbations produced by a given set of coils on a tokamak plasma. For simplicity reasons, we decided to do these calculations in the vacuum hypothesis, i.e. neglecting any current that could appear in the plasma in response to the magnetic perturbations and modify them. Checking the validity of the vacuum hypothesis is one of the main motivations of the non-linear MHD modelling work described in chapter 6. The first application of ERGOS was the calculation of the DIII-D I-coils reference case to be used later for the design of ELMs control coils for ITER. The latter is presented in chapter 5. In fact, designing ELMs control coils for ITER was not the only application of ERGOS. Indeed, EROGS was also used for:

- designing ELMs control coils for other machines than ITER: JET [45], MAST, COMPASS-D [46];

- analysing the experiments on JET and MAST with the error field correction coils, as presented in chapter 4.

In this chapter, we present ERGOS as well as the results of our calculations for the DIII-D I-coils in even and odd parity configurations, the even parity case with a current of 4kAt in the I-coils constituting our reference case. In next section, the code is presented and the results for the I-coils are given without any comments. We dedicate a further section to comments and elements of interpretation of the results.

3.2 Presentation of ERGOS and results of the ERGOS calculations for the DIII-D I-coils

The successive steps in the RMPs analysis by ERGOS, which will be described one by one in this section, are:

- the calculation of the magnetic field produced in vacuum by the set of coils;
- the projection of this magnetic field in the direction perpendicular to the equilibrium flux surfaces;
- the Fourier transformation with respect to the toroidal and poloidal angles, which gives, in particular, the resonant components of the magnetic perturbations;
- the estimation of the islands widths and Chirikov parameter, from the resonant Fourier components, using analytical formulas;
- as an alternative (or rather a complement) to the two preceding steps, the realization of a Poincaré plot.

Each of these steps will now be described and illustrated by the corresponding results for the DIII-D I-coils.

3.2.1 Calculation of the magnetic field produced in vacuum by a given set of coils

The first step in the series of calculations consists in calculating the magnetic field produced by the coils, as if in vacuum. This is done by applying the Biot and Savart formula:

$$\vec{B}(P) = \frac{\mu_0}{4\pi} \sum_{i_{coil}=1}^{n_{coils}} \left(\oint_{coil_{i_{coil}}} \frac{I_{i_{coil}} d\vec{r} \times \vec{r}}{r^3} \right) \tag{3.1}$$

where there is a summation over all the coils and where μ_0 is the magnetic permeability of vacuum, $I_{i_{coil}}$ is the current flowing in coil number i_{coil}, $\vec{r}$ is the vector between point P and a point moving along the coils and $d\vec{r}$ is the corresponding infinitesimal vector. For the DIII-D I-coils in even parity configuration, poloidal cuts of the $B^R \equiv \vec{B} \cdot \vec{e}_R$ and $B^Z \equiv \vec{B} \cdot \vec{e}_Z$ components of the magnetic perturbations (where R and Z are the radial and axial coordinates of the cylindrical system of coordinates whose axis is the axis of revolution of the tokamak) are presented in fig. 3.1.

3.2.2 Calculation of the radial-like component of the magnetic perturbations

The second step is to calculate the radial-like component of the magnetic perturbations, i.e. their component perpendicular to the equilibrium flux surfaces. It is indeed this component that is responsible for the formation of magnetic islands and possible ergodization of the magnetic field. For our reference case, we chose DIII-D shot 125913, a low collisionality shot in which complete ELMs suppression was obtained. The parameters for

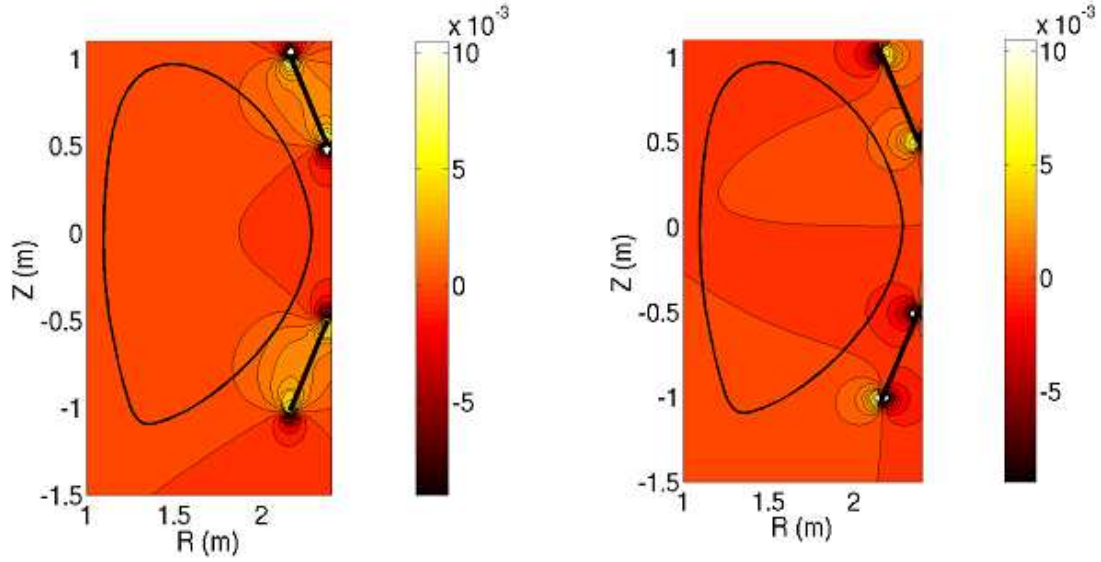

Figure 3.1: Poloidal cuts (in the plane $\varphi = 30°$, which approximately corresponds to the middle of a coil) of B^R (left) and B^Z (right) produced by the I-coils fed with 1kAt, in Teslas. The I-coils appear as black bars, and the plasma separatrix is also represented.

this discharge are a major radius $R_0 = 1.72$m, a triangularity (see [2] for a definition) $\langle\delta\rangle \simeq 0.5$, an elongation [2] $\kappa = 1.78$, a toroidal field on axis $B_0 = 1.9$T, a plasma current $I_p = 1.55$MA, and a safety factor at $s = 0.95^{1/2}$ (see just below for the definition of s) $q_{95} = 3.5$. The magnetic equilibrium and all metric coefficients are calculated using the HELENA code [42]. We work in the intrinsic equilibrium coordinates (s, θ^*, φ), where $s \equiv \psi^{1/2}$ (ψ being the normalized poloidal magnetic flux, cf. introduction) is used as a radial coordinate (in the (s, θ^*, φ) system of coordinates, a flux surface is defined by $s = cte$, in particular $s = 0$ for the magnetic axis and $s = 1$ for the separatrix[1]), and θ^* is such that field lines are straight in the (s, θ^*, φ) system of coordinates:

$$\left.\frac{d\varphi}{d\theta^*}\right|_{FL} = q, \tag{3.2}$$

where the derivative is taken along a field line. We define:

$$B^1 \equiv \vec{B} \cdot \vec{\nabla} s, \tag{3.3}$$
$$B^2 \equiv \vec{B} \cdot \vec{\nabla} \theta^*, \tag{3.4}$$
$$B^3 \equiv \vec{B} \cdot \vec{\nabla} \varphi, \tag{3.5}$$

and our radial-like normalized magnetic perturbations have the following expression:

$$b^r \equiv \frac{b^1}{\sqrt{g^{11}}}, \tag{3.6}$$

[1]It is usual to work with $\psi^{1/2}$ instead of ψ as a radial coordinate (although ψ is sometimes used) because for a cylindrical plasma with a spatially constant axial current density, $\psi^{1/2}$ exactly corresponds to the normalized radius r/a, where a is the plasma minor radius.

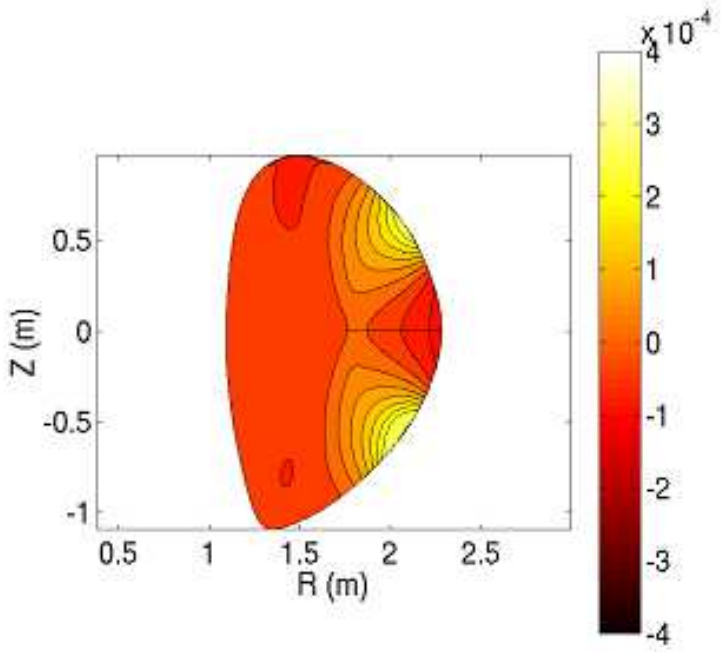

Figure 3.2: Poloidal cut (in the plane $\varphi = 30°$, as in 3.1) of b^r (dimensionless quantity) produced by the I-coils in even parity configuration fed with 1kAt.

where $b^1 \equiv B^1/B_0$ (B_0 being the vacuum toroidal magnetic field on the geometrical axis) and $g^{11} \equiv \vec{\nabla}s \cdot \vec{\nabla}s$. A poloidal cut of b^r produced by the I-coils in even parity configuration is shown in fig. 3.2.

3.2.3 Calculation of the resonant harmonics

Next step consists in calculating the Fourier spectrum of the radial-like magnetic perturbations with respect to the toroidal angle φ and intrinsic poloidal angle θ^*. More exactly, one needs to calculate the Fourier spectrum of

$$\tilde{b}^1 \equiv B^1/B^3, \tag{3.7}$$

with $B^3 \equiv \vec{B} \cdot \vec{\nabla}\varphi$, because it is the resonant harmonics of $\tilde{b}^1$ that appear in the expression of the islands widths. This is demonstrated in appendix A). We define:

$$\tilde{b}^1_{mn}(s) \equiv \int_{\varphi=0}^{2\pi} \int_{\theta^*=0}^{2\pi} \tilde{b}^1\left(s, \theta^*, \varphi\right) e^{-i(m\theta^* + n\varphi)} \frac{d\theta^*}{2\pi} \frac{d\varphi}{2\pi}, \tag{3.8}$$

so that:

$$\tilde{b}^1\left(s, \theta^*, \varphi\right) = \sum_{m,n=-\infty}^{\infty} \tilde{b}^1_{mn}(s) e^{i(m\theta^* + n\varphi)}. \tag{3.9}$$

It should be noticed that, because $\tilde{b}^1$ is a real number, we have:

$$\tilde{b}^1_{-m,-n} = \left(\tilde{b}^1_{mn}\right)^*, \tag{3.10}$$

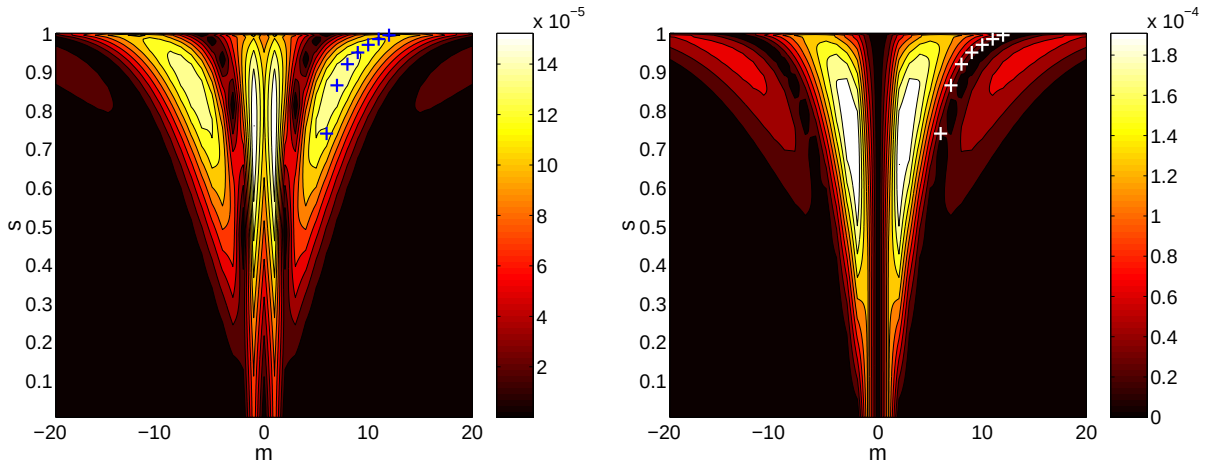

Figure 3.3: Spectrum of $2|\tilde{b}^1_{m,-3}|$ (dimensionless quantity) as a function of m and the radial coordinate s, for 1kAt in the I-coils, with crosses showing the position of the resonant harmonics, $\tilde{b}^1_{res}$. Left: even parity configuration. Right: odd parity configuration.

where the star designates the conjugate complex number. Our convention is that, along a field line, we have: $d\varphi = qd\theta^*$, so that $m\theta^* - n\varphi$ is a constant quantity on a field line located on the $q = m/n$ surface. One should therefore keep in mind that the components of $\tilde{b}^1$ that are resonant on such a surface are not $\tilde{b}^1_{mn}$ and $\tilde{b}^1_{-m,-n}$ but $\tilde{b}^1_{m,-n}$ and $\tilde{b}^1_{-m,n}$ (and also $\tilde{b}^1_{2m,-2n}$ etc.). We will often be considering cases where one toroidal harmonic (n_0) is dominant over the others. For instance, in the case of the DIII-D I-coils, the $n_0 = 3$ harmonic dominates. Then, the resonant surfaces which we will consider are those of the type $q = m/n_0$. Let us express the resonant part of $\tilde{b}^1$ on such a surface:

$$\left(\tilde{b}^1\right)_{res} = \tilde{b}^1_{m,-n_0} e^{i(m\theta^* - n_0\varphi)} + \tilde{b}^1_{-m,n_0} e^{i(-m\theta^* + n_0\varphi)} \quad (3.11)$$

$$= 2\Re\left(\tilde{b}^1_{m,-n_0} e^{i(m\theta^* - n_0\varphi)}\right) \quad (3.12)$$

$$= 2|\tilde{b}^1_{m,-n_0}| \sin(m\theta^* - n_0(\varphi - \varphi_0)), \quad (3.13)$$

where use has been made of 3.10, $\Re$ designates the real part and where φ_0 is an appropriate phase. We thus define:

$$\tilde{b}^1_{res} \equiv 2|\tilde{b}^1_{m,-n_0}|. \quad (3.14)$$

Fig. 3.3 represents the quantity $2|\tilde{b}^1_{m,-3}|$ as a function of m and the radial coordinate s, for both even parity (left) and odd parity (right) configurations. Crosses are added in order to show the position of the resonant harmonics, $\tilde{b}^1_{res}$.

The expression that we use for the physical effective radial RMPs is:

$$b^r_{res} \equiv \frac{\tilde{b}^1_{res}}{R_0 \langle\sqrt{g^{11}}\rangle_{\theta^*}}, \quad (3.15)$$

where the brackets represent an averaging over θ^*: $\langle\sqrt{g^{11}}\rangle_{\theta^*} \equiv \int_{\theta^*=0}^{2\pi} \sqrt{g^{11}} \frac{d\theta^*}{2\pi}$. Fig. 3.4 represents the profile of b^r_{res} for the I-coils fed with 4kAt (the typical current used in the experiments and our reference for the ITER ELMs control coils design study).

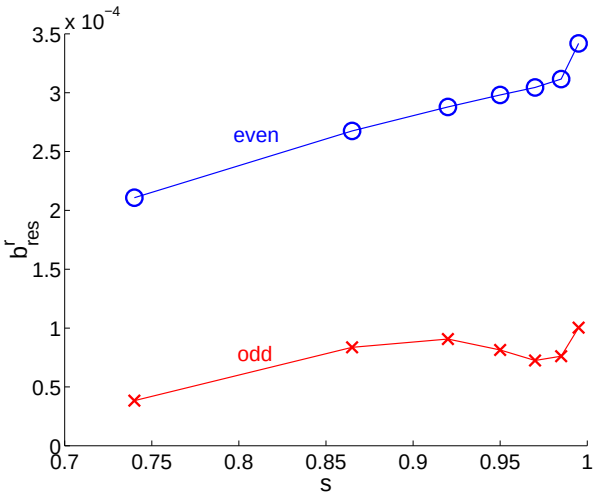

Figure 3.4: Profile of b^r_{res} (dimensionless quantity) for 4kAt in the I-coils in even (circles) and odd (crosses) parity configurations.

3.2.4 Estimation of islands half-widths and Chirikov parameter

The islands half-widths in terms of s on the $q = m/n$ surface, denoted $\delta_{q=m/n}$, is estimated using the following expression, which is derived in appendix A:

$$\delta_{q=m/n} = \left(\frac{4q^2 \tilde{b}^1_{res}}{q'm} \right)^{1/2}, \tag{3.16}$$

where $q' \equiv dq/ds$ is the magnetic shear. Fig. 3.5 shows the q profile for DIII-D shot 125913 together with symbolic islands represented by horizontal bars of half-widths $\delta_{q=m/n}$ produced by the I-coils fed with 4kAt, for both even and odd parity configurations. The Chirikov parameter in-between the $q = m/n$ and $q = (m+1)/n$ surfaces, denoted $\sigma^{m,m+1}_{Chir}$ is finally calculated as:

$$\sigma^{m,m+1}_{Chir} \equiv \frac{\delta_{q=m/n} + \delta_{q=(m+1)/n}}{\Delta_{m,m+1}}, \tag{3.17}$$

where $\Delta_{m,m+1}$ designates the radial distance (in terms of s) between the $q = m/n$ and the $q = (m+1)/n$ surfaces, which can be approximated as:

$$\Delta_{m,m+1} \simeq \frac{q}{mq'} \tag{3.18}$$

(but in ERGOS we take for $\Delta_{m,m+1}$ the actual distance between the two resonant surfaces, without any approximation: $\Delta_{m,m+1} \equiv s(q = (m+1)/n) - s(q = m/n)$). Fig. 3.6 represents the profile of $\sigma^{m,m+1}_{Chir}$ for 4kAt in the I-coils, for both even and odd parity configurations.

3.2.5 Poincaré plots

We also perform Poincaré plots, which can be used in order to cross-check the analytical estimations for the islands widths and Chirikov parameter. These Poincaré plots are done

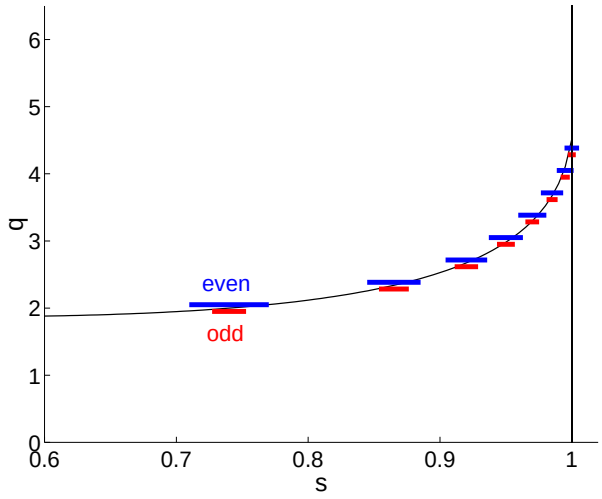

Figure 3.5: q profile for DIII-D shot 125913 together with symbolic islands represented by horizontal bars of half-widths $\delta_{q=m/n}$ produced by the I-coils fed with 4kAt (upper bars for even parity, lower bars for odd parity).

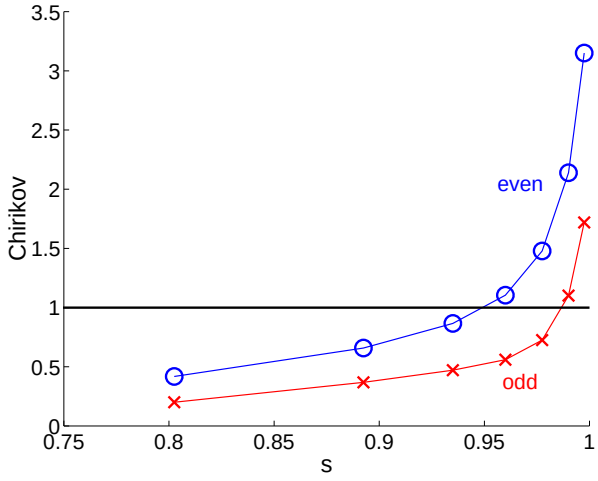

Figure 3.6: Profile of $\sigma_{Chir}^{m,m+1}$ for DIII-D shot 125913 produced by the I-coils fed with 4kAt.

by numerically following a large number of field lines over a large number of toroidal rotations, integrating the equations:

$$\frac{ds}{d\varphi} = \frac{B^1}{B^3} \tag{3.19}$$

$$\frac{d\theta^*}{d\varphi} = \frac{1}{q}. \tag{3.20}$$

Rigorously, the second equation should be $\frac{d\theta^*}{d\varphi} = \frac{B^2}{B^3}$, but we neglect the perturbations from the ELMs control coils to B^2 and B^3, i.e. we keep the equilibrium B^2 and B^3, which satisfy $\frac{B^2}{B^3} = \frac{1}{q}$. In order to perform the integration, we use a 4th order Runge-Kutta algorithm.

Poincaré plots obtained for 4kAt in the I-coils is shown in fig. 3.7. They show an excellent agreement with the analytical calculations for the islands widths.

However, fig. 3.8 only allows one to "guess" if ergodicity is present or not, but it does not provide any means of determining this properly and does not allow one to estimate the width of the ergodic region. For this reason, it is useful to color the points in the Poincaré plots in order to show if they belong or not to the ergodic region. On fig. 3.8, we present one such colored Poincaré plot, done for the I-coils in even parity configuration, fed with 4kAt (i.e. the equivalent of top plot in fig. 3.8). The plot is done as follows: there are 12 departure points in s (equally spaced between 0.85 and 0.995) and 1 in θ^* (at $\theta^* = 0$), and field lines are followed over a maximum of 8000 toroidal turns. If a field line, starting from a given departure point, crosses the unperturbed separatrix ($s = 1$) after a certain number of toroidal rotations, then each Poincaré point generated by this field line is colored by the number of toroidal rotations that remain to be done before the field line crosses the unperturbed separatrix. If, after 8000 toroidal turns, the field line has not crossed the unperturbed separatrix, then all the Poincaré points generated by this field line have the color corresponding to the value 8000. In the figure, the clear frontier between the red and the blue regions shows that the ergodic region extends up to $s \simeq 0.9$.

Now, looking back at fig. 3.6, we see that the Chirikov parameter is below 1 at $s \simeq 0.93$, i.e. between the $(m = 8, n = 3)$ and the $(m = 9, n = 3)$ islands chains, meaning that there is no overlapping of these two islands chains. Therefore, there seems to be a disagreement between the Chirikov parameter calculations and the Poincaré plot. This paradox is solved by noticing that there are so-called "second-order islands" [43] with an $(m = 17, n = 6)$ structure[2], located around the $q = 17/6$ surface, i.e. in between the $(m = 8, n = 3)$ and $(m = 9, n = 3)$ islands chains. These secondary islands and the role they play in the ergodization process can be observed on fig. 3.9, which presents two Poincaré plots done for the I-coils in even parity fed with 1kAt (top plot) and 3kAt (bottom plot). On this figure, one can see the $(m = 8, n = 3)$ (resp. $(m = 9, n = 3)$) first-order islands centered on $s \simeq 0.918$ (resp. $s \simeq 0.950$) and the second-order $(m = 17, n = 6)$ islands centered on $s \simeq 0.937$. Judging by the plot for 1kAt, it is clear that a direct overlapping of the $(m = 8, n = 3)$ and $(m = 9, n = 3)$

[2]The fact that n is equal to 6 cannot be seen on Poincaré plots and has not been verified, but it is expected by theory, see [43]. Also, we stress the fact that these islands are not due to the $n = 6$ part of the RMPs spectrum produced by the I-coils: indeed, they also exist if we perform the Poincaré plot taking only the $n = 3$ component of the RMPs.

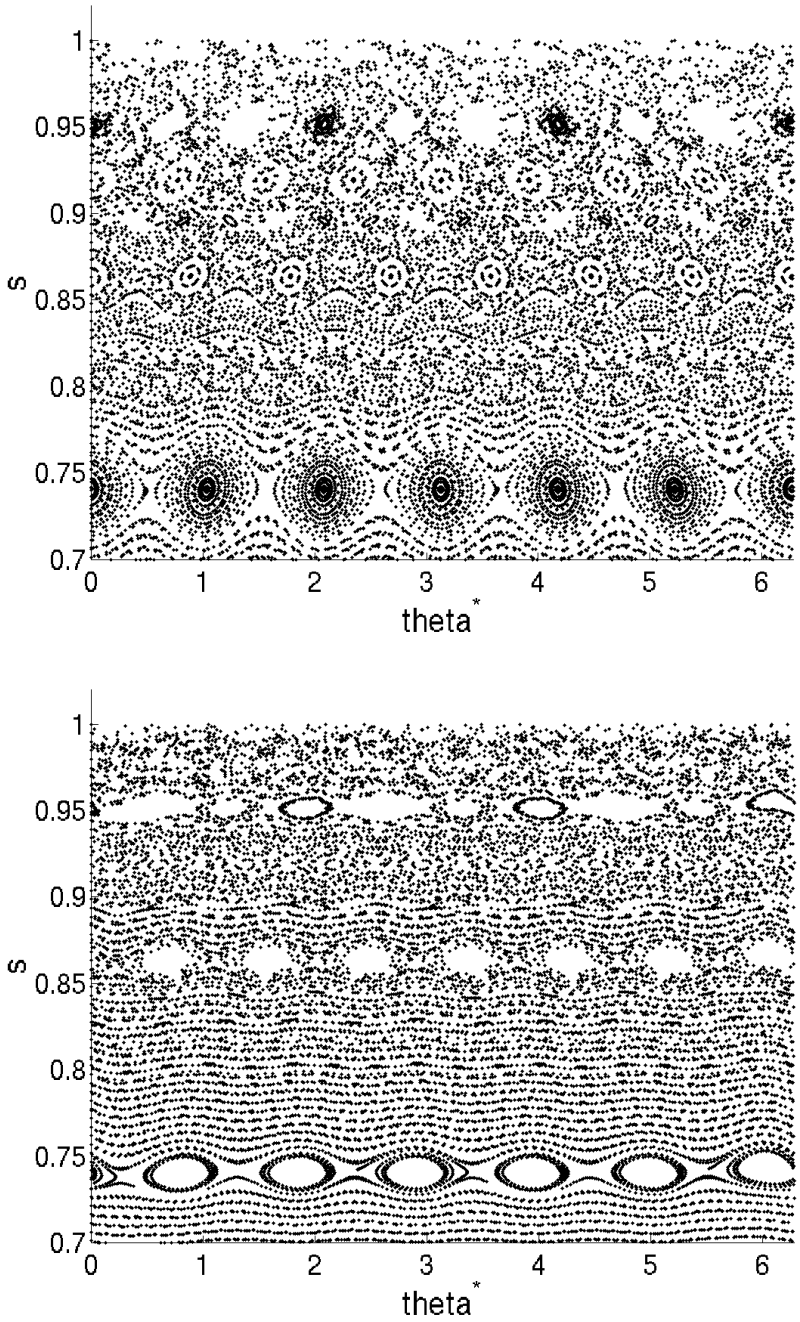

Figure 3.7: Poincaré plots for DIII-D shot 125913 with magnetic perturbations from the I-coils fed with 4kAt. Top: even parity configuration. Bottom: odd parity configuration.

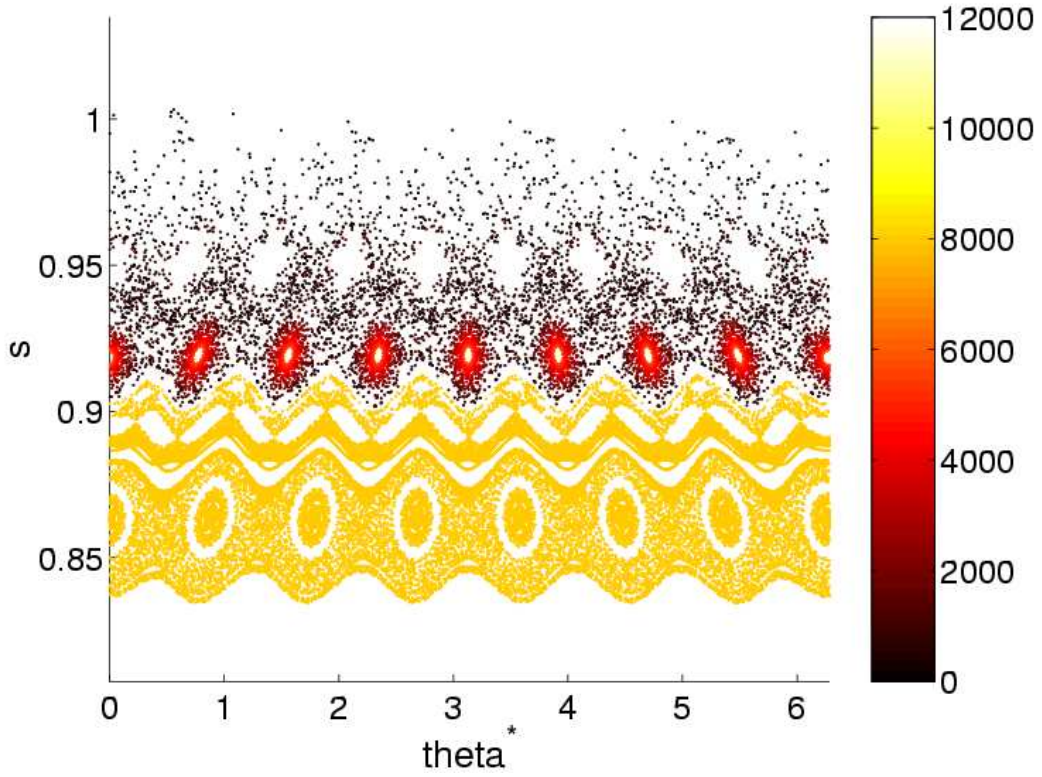

Figure 3.8: Colored Poincaré plot for DIII-D shot 125913 with magnetic perturbations from the even parity I-coils fed with 4kAt.

islands chains would require more than a doubling of their widths, i.e. a multiplication of the current in the I-coils by more than a factor of 4 (since the islands widths scales as the square root of the I-coils current, see eq. 3.16). However, as the I-coils current is increased, it can be seen that many closed flux surfaces are destroyed between the first order islands chains due to a "cascade" of higher order resonances[3]. This shows that the secondary and higher order islands ease the process of ergodization of the magnetic field, explaining why the ergodic layer can extend up to $s \simeq 0.9$ even though the $(m = 8, n = 3)$ and $(m = 9, n = 3)$ do not directly overlap and finally reconciling the Chirikov parameter calculations and the Poincaré plots.

3.3 Interpretation and comments on the results of the ERGOS calculations for the DIII-D I-coils

Now that we have presented the calculations done by ERGOS and their results in the case of the DIII-D I-coils, we analyze these results and make a qualitative discussion which allows one to gain intuition as to what determines the RMPs profile and why the even parity configuration is more efficient than the odd parity one.

[3]Islands of higher than second order can also be observed here, for instance an $(m = 25, n = 9)$ on the plot for 1kAt at $s \simeq 0.932$.

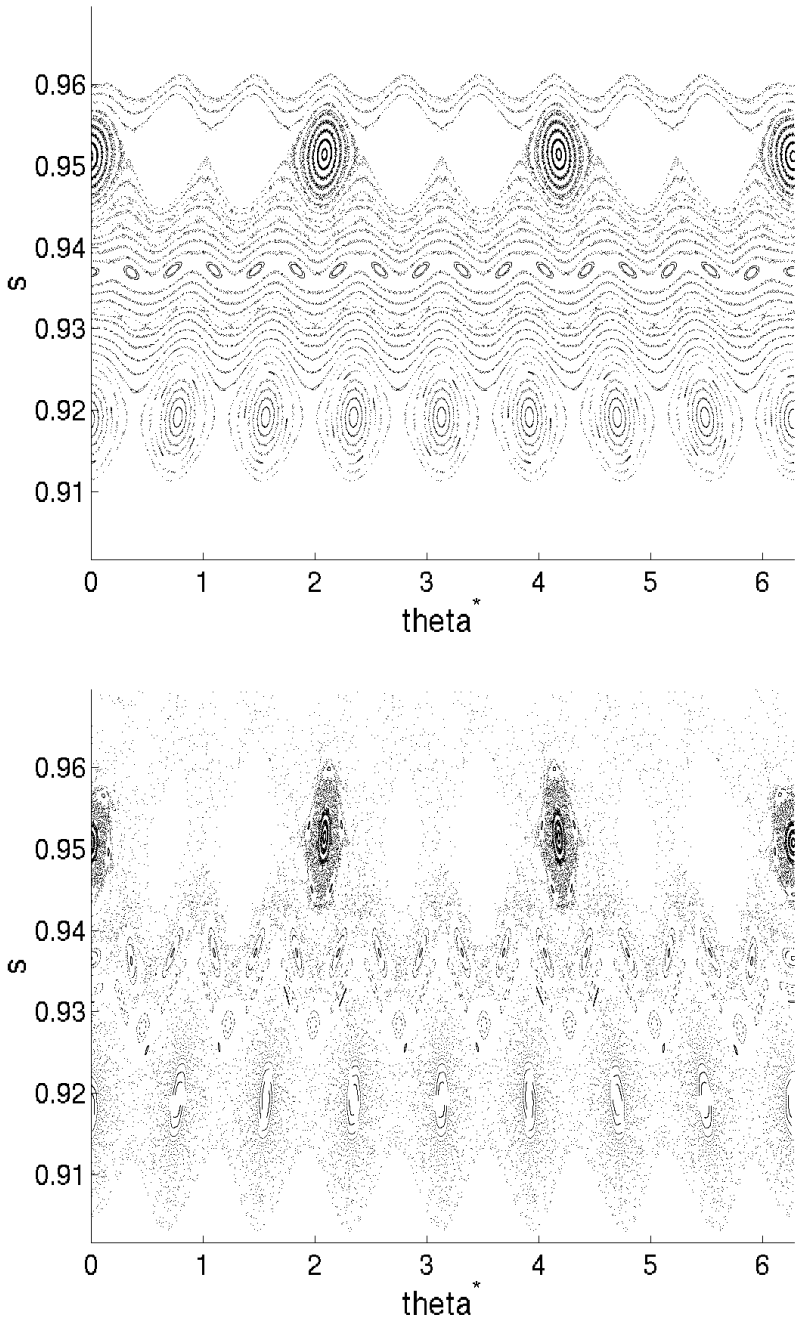

Figure 3.9: Poincaré plots for the I-coils in even parity configuration, fed with 1kAt (top) and 3kAt (bottom).

3.3.1 The θ^* effect

First, for the even parity configuration, it can be surprising to observe that the RMPs spectrum is peaked, at the edge, around poloidal mode numbers m of about 10 or 12 (see fig. 3.3, left). Indeed, judging by a poloidal cut of b^r (fig. 3.2), one would rather expect a peaking of the Fourier spectrum with respect to the poloidal angle around $m = 4$, because the positive and negative "bumps" of b^r have a poloidal extension of about $\frac{2\pi}{8}$. But this is in terms of the geometrical poloidal angle, θ, whereas in fact the RMPs spectrum is calculated with respect to θ^*, the intrinsic poloidal angle. On fig. 3.10 is represented a poloidal view of the mesh of intrinsic equilibrium coordinates, showing lines of constant $s = k/20$ (poloidal cuts of flux surfaces), with $k = 1, ..., 20$, and lines of constant $\theta^* = 2\pi l/32$, with $l = 0, ..., 31$. It is clear, looking at this figure, that θ^* varies more slowly with respect to θ on the Low Field Side (LFS) than elsewhere. As a consequence, the function $b^r(\theta^*)$ is much more contracted around 0 than the function $b^r(\theta)$, and thus magnetic perturbations localized on the LFS have a higher poloidal mode number with respect to θ^* (m_{θ^*}) than with respect to θ (m_θ). This so-called "θ^* effect" is also known from experimentalists who, from magnetic measurements, want to determine the poloidal mode number of magnetic perturbations that appear in the plasma [44]. This is the occasion to notice that the classical statement that "magnetic perturbations with a poloidal mode number m have an amplitude proportional to r^{-m} (r being the minor radius)", which is true[4] in purely cylindrical geometry when the poloidal mode number is defined with respect to the cylindrical angle θ (see demonstration in appendix B), does not apply here, because of the θ^* effect. In order to apply such a "thumb rule", one should at least replace the intrinsic poloidal mode number $m = m_{\theta^*}$ by the geometrical poloidal mode number m_θ, which, due to the θ^* effect, is much smaller, implying a much slower decrease of the RMPs with r.

Now, where does this effect come from? Let us first notice that, since θ^* is defined by the relation $\frac{d\varphi}{d\theta^*}\big|_{FL} = q$ (see section 3.2.2), an alternative formulation of the θ^* effect is that field lines have a much larger pitch angle (the angle they form with the horizontal plane), i.e. a larger poloidal field with respect to the toroidal field, on the LFS than elsewhere. There are in fact several factors that are responsible for this:

- The first one is the presence of an X-point (and closeness to the presence of a second X-point at the top of the plasma). Indeed, since the poloidal magnetic field at the X-point is null, when approaching it, field lines have a smaller and smaller pitch angle. This effect is strongest for the most external flux surfaces.

- Then, toroidal effects also play a role. One well known toroidal effect is the so-called "Shafranov shift" [2], which is a contraction of the equilibrium flux surfaces toward the LFS due to plasma pressure. On fig. 3.10, one can indeed see that flux surfaces are closer to each other on the LFS than on the HFS. Since the poloidal magnetic flux is constant between two magnetic surfaces, the poloidal magnetic field is larger where flux surfaces are closer to each other, i.e. on the LFS, contributing to the θ^* effect.

- Finally, even with no Shafranov shift, i.e. with concentric magnetic flux surfaces,

[4] when it concerns the magnetic potential (if it concerns the radial magnetic field, then the dependency is in $r^{-(m-1)}$)

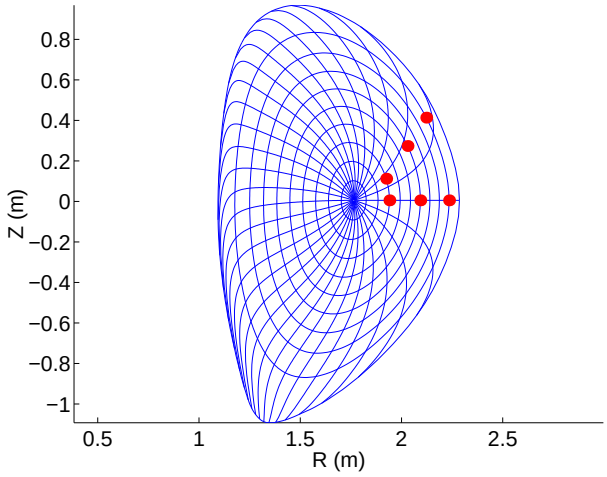

Figure 3.10: Poloidal view for DIII-D shot 125913 showing the mesh of intrinsic equilibrium coordinates (20 lines of constant $s = k/20$ with $k = 1, ..., 20$, and 32 lines of constant $\theta^* = 2\pi l/32$, with $l = 0, ..., 31$). Red dots represent the positions of 3 field lines on 3 different flux surfaces. For each of these, one dot is plotted when the field lines are at $\theta^* = 0$ and another dot is plotted after an advance in the toroidal direction by $\Delta\varphi = 2\pi/10$.

there would already exist a θ^* effect due to the toroidal geometry (see [48]).

Another very important consequence of the θ^* effect is the alignment of the RMPs spectrum on the q profile, that appears clearly on fig. 3.3. This alignment can be understood easily when comparing figs. 3.11 and 3.12, which show colormaps of B^1/B^3 on the $q = 2$ and $q = 3$ equilibrium surfaces respectively, together with $q = 2$ and $q = 3$ field lines: going from the $q = 3$ to the $q = 2$ surface, the colormap of B^1/B^3 is like "stretched" in the poloidal direction in the same time as field lines change their orientation. In fact, thinking in terms of geometrical space, this only means that field lines on the $q = 2$ and $q = 3$ surfaces have nearly the same pitch angle. This is illustrated by the red dots appearing on fig. 3.10: for three different flux surfaces, we plotted a dot at $\theta^* = 0$, then we advanced three field lines starting from each of these points toroidally by $\Delta\varphi = 2\pi/10$ and plotted three other dots. The fact that the dots alignment is conserved shows that field lines rotate together on the LFS. We will see in chapter 5 that this property is rather unfortunate with respect to the question of minimizing the ratio of core to edge RMPs produced by ELMs control coils, since it implies a strong correlation of core and edge RMPs.

3.3.2 Comparison of the even and odd parity configurations

As clearly appeared in the results shown in last section, the even parity configuration is much more efficient at producing RMPs than the odd parity configuration. This can be understood very well looking at figs. 3.11 and 3.12 and comparing the left and right plots: with the even parity configuration, a field line that passes on the LFS undergoes two successive radial "kicks" in the same direction, whereas with the odd parity configuration the kicks are in opposite direction, cancelling each other. It should be noticed that, if q was somewhat smaller or larger, the situation would be opposite: the even parity

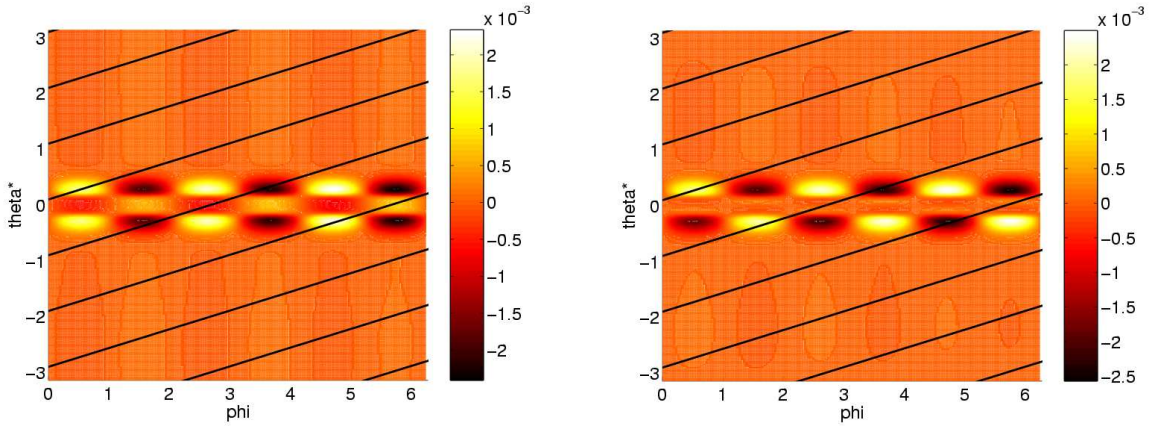

Figure 3.11: Colormap of B^1/B^3 (dimensionless quantity) on the $q = 3$ equilibrium flux surface, together with several field lines. Left: I-coils even parity (1kAt). Right: I-coils odd parity (1kAt).

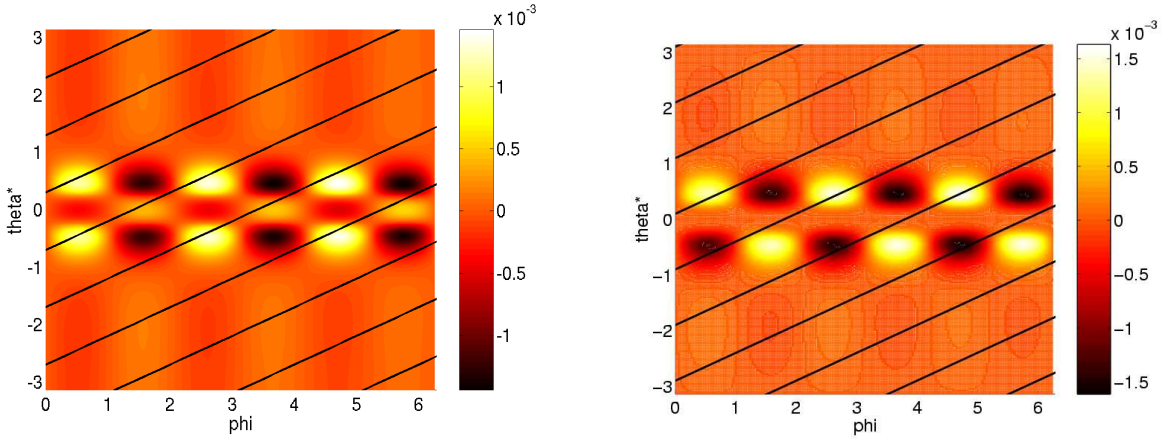

Figure 3.12: Colormap of B^1/B^3 (dimensionless quantity) on the $q = 2$ equilibrium flux surface, together with several field lines. Left: I-coils even parity (1kAt). Right: I-coils odd parity (1kAt).

configuration would produce small RMPs while the odd parity one would produce large RMPs[5]. We can thus say that these two configurations are complementary and offer a possibility of adaptation to different q profiles. This idea will be mentioned again in chapter 5.

3.3.3 Interpreting the magnetic perturbations spectrum

Figs. 3.11 and 3.12 allow one to gain intuitive insight on the spectrum of the magnetic perturbations presented on fig. 3.3. Indeed, a horizontal displacement in fig. 3.3, i.e. a change in the poloidal mode number m, corresponds, in figures such as figs. 3.11 or 3.12, to a change in the inclination of the lines. It is then easy to understand the origin of the "ridges" and "valleys" in fig. 3.3: ridges correspond to lines with inclinations such that they undergo a significant total radial kick, while valleys correspond to inclinations such

[5]This is the case for the new MAST ELMs control coils presented on fig. 4.1.

that the several individual radial kicks underwent by the lines compensate each other, so that the total radial kick is small.

3.4 Summary

A suite of numerical codes called ERGOS was developed in order to calculate and analyze the magnetic perturbations produced by a given set of coils on a tokamak plasma, in the vacuum approximation. The first application of ERGOS was devoted to the DIII-D I-coils. The case of the I-coils in even parity configuration fed with 4kAt for DIII-D shot 125913 constitutes a reference for later studies, in particular for the design of ELMs control coils for ITER presented in chapter 5. Indeed, full ELMs suppression was obtained in this low, ITER-relevant, collisionality shot. It was found for this case that the ergodized layer extends from the unperturbed separatrix inside the plasma up to $s \sim 0.9$, the Chirikov parameter being above 1 for $s \geq 0.95$ and reaching $\simeq 3$ at $s = 1$.

Chapter 4

ELMs control with the Error Field Correction Coils at JET and MAST

4.1 Context

After the success of the DIII-D experiments, it was thought that the method of ELMs control by RMPs should be tested in other tokamaks. In view of an application to ITER, it is indeed very desirable to progress in the understanding of the physical mechanisms at play in ELMs control by RMPs and to estimate the robustness of the method. However, no divertor machine had coils similar to the DIII-D I-coils at that time.
In the case of JET, a design project for ELMs control coils was launched and completed at CEA Cadarache in 2005 making use of the ERGOS suite of codes presented in chapter 3 [45]. At the moment this manuscript is being written, the tokamaks MAST and ASDEX-Upgrade are about to install new coils specifically designed for ELMs control. CEA and ERGOS were involved in the design of the MAST coils, which are presented on fig. 4.1. The tokamak COMPASS-D, which is being transferred from Culham, England, to Prague, Czech Republic, also comprises a set of coils that can produce significant RMPs at the edge of the plasma. The calculation of the RMPs for the COMPASS-D coils and selection of the most promising configurations between the many possibilities of coils phasing was done in collaboration with CEA, using ERGOS again [46].
On the other hand, in two tokamaks, namely JET and MAST, experiments have been done recently, using sets of coils that were already in the machines but built for other purposes, namely the Error Field Correction Coils (EFCCs). These coils, as their name indicates, were built in order to compensate for error fields, i.e. small departures of the principal magnetic field from pure axisymmetry. Error fields are naturally present in all tokamaks, due for instance to unavoidable misalignments of the toroidal or poloidal field coils or to the current flowing in the coils alimentation systems. In large tokamaks, they pose serious problems, and in particular for ITER the level of tolerance to error fields is very small ($\delta B/B \sim 10^{-4}$), so that EFCCs are also part of the ITER design (see [73] and section 5.5.4).
We provided modelling support for both the JET and MAST experiments with EFCCs, showing in particular with ERGOS the ability of the EFCCs to ergodize the magnetic field at the edge in both machines, even if they were not designed for this. We also participated on site to the experiments, which gave promising and interesting results, with

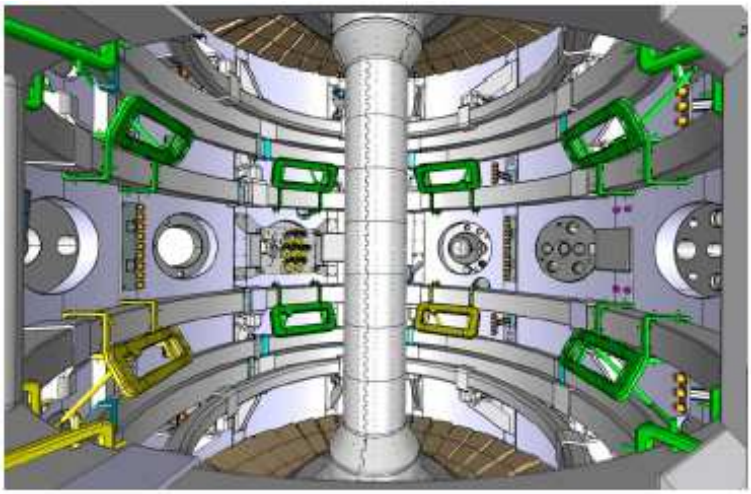

Figure 4.1: Design of the future ELMs control coils at MAST. (courtesy A. Kirk)

clear ELMs mitigation obtained at JET and possible effects observed at MAST. In the following sections, we will describe the experiments as well as our associated modelling work, for JET and for MAST successively.

4.2 ELMs control by the Error Field Correction Coils at JET

The design of the JET EFCCs is represented on fig. 4.2. There are 4 square coils equally spaced toroidally. Each one is made of windings comprising 16 turns. The maximum current per turn is 3kA, i.e. the maximum current in one coil is 48kAt. The coils feedings can be changed in such a way that the respective directions of currents in the coils (when going from one to another, moving toroidally) can be either + + - -, producing mainly $n = 1$ perturbations, or + - + -, producing mainly $n = 2$ perturbations.
In June 2006, we did preliminary calculations that showed the ability of the EFCCs to ergodize the magnetic field at the edge, but expressed doubts on the possibility to do so without triggering core MHD modes [49]. First experiments, in the $n = 1$ configuration, were done at the end of 2006 and beginning of 2007, and we participated on site [50]. More recently, the $n = 2$ configuration was investigated. Both $n = 1$ and $n = 2$ configurations were successful in mitigating the ELMs (the sense of "mitigating" will be explained below).
In a first subsection, we will describe the experimental results, for both $n = 1$ and $n = 2$ configurations, and discuss briefly the relevance of these results for ELMs mitigation in ITER. In a second subsection, we will show results of our calculations of the RMPs for the $n = 1$ configuration and analyze an experimental q_{95} scan, comparing the experimental thresholds for ELMs mitigation with thresholds for islands overlapping found in our modelling. We will also show examples of calculated so-called "magnetic footprints", which could be used in the future as a powerful tool for analyzing the experiments. Finally, in a third subsection, we will present the results of our RMPs calculations for

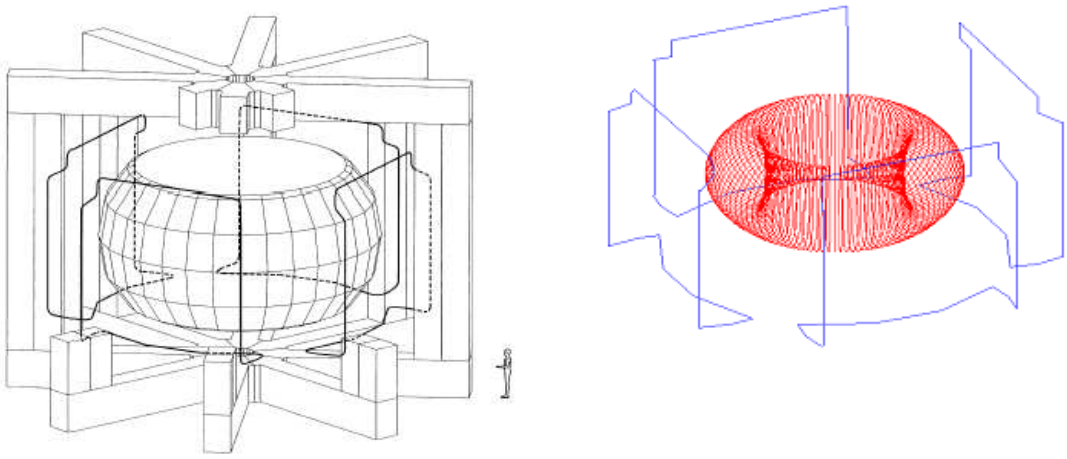

Figure 4.2: Design of the JET EFCCs. The left figure is taken from [47].

the $n = 2$ configuration.

4.2.1 Summary of the experimental results

Experiments in $n = 1$ configuration

Fig. 4.3 shows time traces from one of the $n = 1$ experimental shots: (a) shows the total input power, P_{total}, and the diamagnetic energy stored in the plasma, W_{dia} (denoted E_{dia} on fig. 4.3), (b) the current in the EFCCs, I_{EFCC} (units should be kAt, not kA as written on the vertical axis), (c) the line-integrated electron densities, $n_e l$, measured with an interferometer along two vertical lines of sight, one close to the magnetic axis (upper trace) and the other near the top of the pedestal (lower trace), (d) the electron temperature, T_e, from the Electron Cyclotron Emission (ECE) diagnostic, measured near the center of the plasma (upper trace) and at the top of the pedestal (lower trace), (e) the D_α signal in front of the outer divertor, (f) the fast ion loss current, I_{loss}, measured by Faraday cups [52], and (g) the magnetic fluctuations dB_θ/dt measured by a magnetic pickup coil. It can be seen, first of all, that during the EFCCs pulse, the D_α spikes get smaller and their frequency increases (the same behaviour is observed on the I_{loss} trace), meaning that ELMs remain present during the EFCCs pulse, but become smaller and have their frequency raising. In the case shown on fig. 4.3, the ELMs frequency increases from ∼30Hz to ∼120Hz and the normalized energy loss per ELM, $\Delta W_{dia}/W_{dia}$, decreases from ∼7% to below 2%. It can also be seen on the dB_θ/dt trace that magnetic fluctuations bursts become smaller. This reduction of ELMs amplitude and enhancement of ELMs frequency is similar to what was observed in DIII-D low collisionality experiments when q_{95} was out of the resonant window [53] and different from what was observed when q_{95} was inside the resonant window (i.e. a complete suppression of the ELMs, see chapter 2). When looking at the plasma profiles (fig. 4.4), other similarities to the DIII-D low collisionality experiments appear. Indeed, a density pump-out is observed (although it is smaller than at DIII-D), as well as an increase in the core electron and ion tempera-

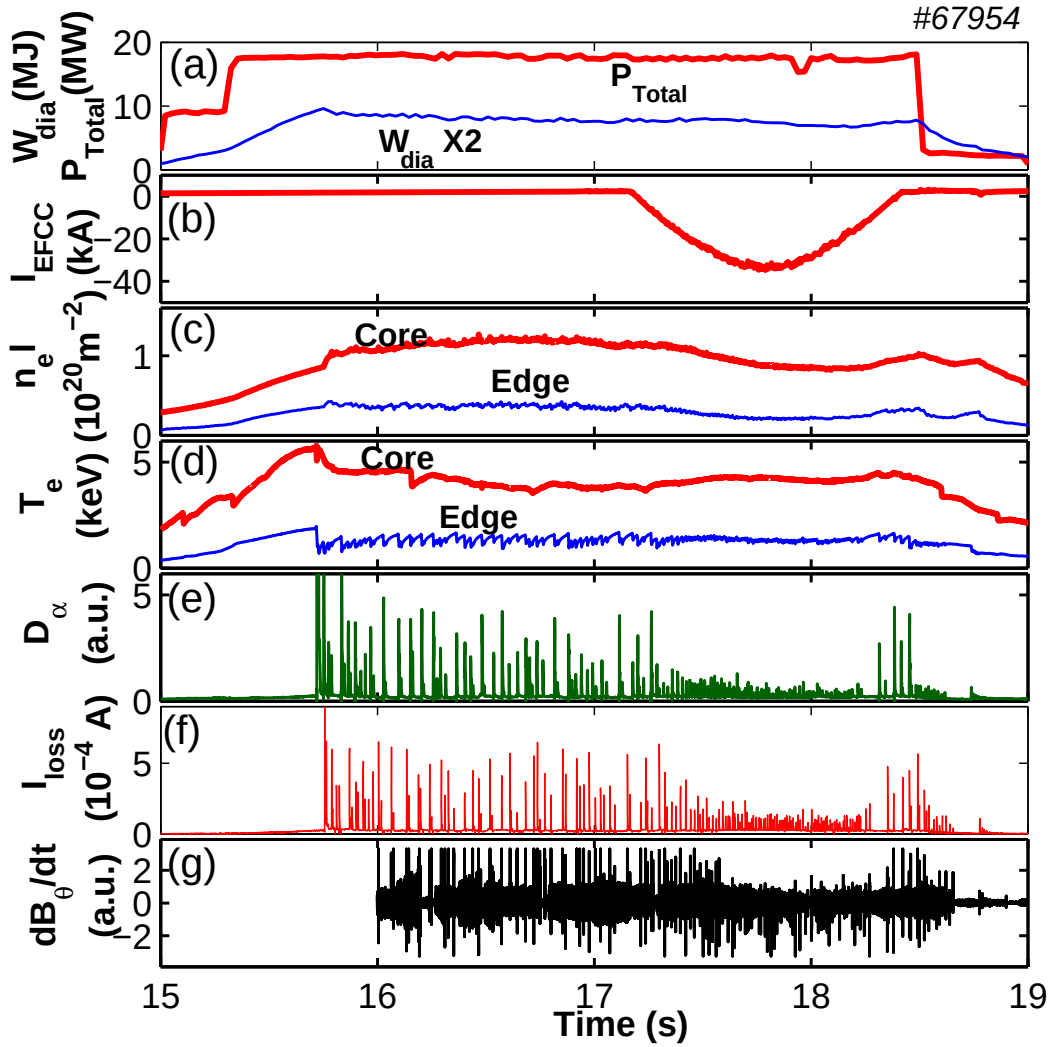

Figure 4.3: Overview on a typical ELM mitigation experiment with the EFCCs in $n = 1$ configuration (taken from [50]).

tures. A further important common point with DIII-D is that the energy confinement factor $H_{98(y,2)}$ (see chapter 2 for a definition) stays constant during the EFCCs pulse. The plasma toroidal rotation however behaves somewhat differently from the DIII-D low collisionality experiments, in the sense that here a clear drop of the toroidal rotation is observed on the whole profile, whereas in the DIII-D low collisionality experiments there was a spin-up at the edge (but a braking more towards the core)[1]. It was also observed that the EFCCs in $n = 1$ configuration can trigger an $n = 1$ locked mode, in particular at low q_{95} (∼3.0-3.5) (see subsection 4.2.2). It can finally be noticed that the operational domain of ELMs mitigation with the EFCCs was extended towards ITER parameters, i.e. low collisionality ($\nu_e^* \sim 0.09$), high triangularity ($\delta^u \simeq 0.45$, $\delta^l \simeq 0.4$) and high normalized beta ($\beta_N \sim 3$) [54].

[1]On the other hand, in the DIII-D high collisionality experiments, a drop of the rotation was observed on the whole profile, like in JET.

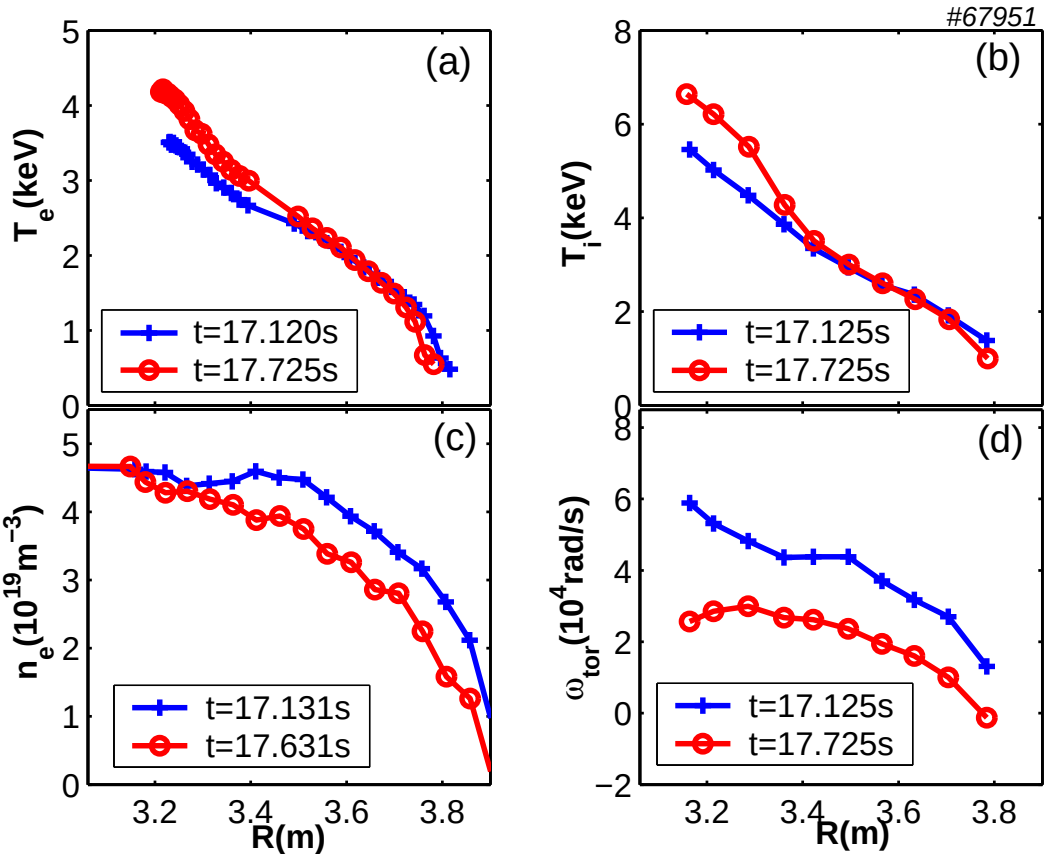

Figure 4.4: Comparison of plasma profiles (taken at the plasma midplane) before (+) and during (o) the EFCCs shot. (a) Electron temperature, (b) ion temperature, (c) electron density and (d) toroidal rotation frequency.

Experiments in $n = 2$ configuration

Experiments in $n = 2$ configuration (see fig. 4.5) have shown a phenomenology almost identical to experiments in $n = 1$ configuration, namely an increase in the frequency and decrease in the amplitude of ELMs (although less marked than for $n = 1$), a density pump-out, an increase in the electron and ion temperatures, as well as a similar braking of the toroidal rotation [55].

Relevance of the results to ITER

The results obtained so far are promising. However, in order to make type I ELMs harmless in ITER, most recent estimations are that a reduction of the ELMs energy losses by a factor $\simeq 8$ is required (from 17MJ to 2MJ typically, see section 1.6.1). Here, only a reduction by a factor $\simeq 4$ was obtained, which, even though it is already a considerable achivement, is still insufficient by a factor 2. Furthermore, the impact of low n core perturbations, as well as the large non-resonant perturbations produced by EFCCs-like coils may be a limiting factor for an application to ITER, see chapter 5.

4.2.2 Modelling for the $n = 1$ experiments

RMPs spectrum

The RMPs spectrum calculated with ERGOS for the JET EFCCs in $n = 1$ configuration is presented on fig. 4.6. It is smoother than the spectrum of the DIII-D I-coils shown in chapter 3 and also does not display several "valleys" and "ridges". This is because the JET EFCCs are "monopole" coils, i.e. there is only one row of coils, whereas the DIII-D I-coils, distributed in two rows, are "multipole" coils.

Analysis of a q_{95} scan

Fig. 4.7 shows time traces of I_{EFCC} and D_α for four shots with different q_{95} values: 4.8, 4.0, 3.5 and 3.0. ELMs mitigation was obtained in all cases, showing the robustness of the method with respect to variations in q_{95}[2]. It can however be observed on fig. 4.7 that ELMs mitigation does not start from the very beginning of the EFCCs ramp up. This seems to suggest that there exists a threshold in I_{EFCC} for ELMs mitigation (although a shot-to-shot scan in I_{EFCC} would be required in order to establish this rigorously). On the other hand, if I_{EFCC} is pushed to too high values, a locked mode can be triggered. This is the case for the shots with $q_{95} = 3.5$ and $q_{95} = 3.0$ (the time of ocurrence of the locked mode is marked by a vertical dashed line on fig. 4.7). In all four shots shown here, there thus exists an operational window in terms of I_{EFCC} for ELMs mitigation, in-between the threshold for ELMs mitigation and the threshold for locked mode triggering (remark: in the cases $q_{95} = 4.8$ and $q_{95} = 4.0$, no locked mode was observed at the maximal explored value of $I_{EFCC} = 36.8$kAt, so that the upper end of the operational window is not known). This operational window can be seen on fig. 4.8, which represents,

[2]This is the occasion to recall that in the DIII-D experiments, there was a very narrow q_{95} window (with a typical width of a few 0.1) for total ELMs suppression. However, it should also be kept in mind that (as mentioned above), outside the resonant window, an effect on the ELM similar to the one observed at JET was seen in DIII-D experiments [53].

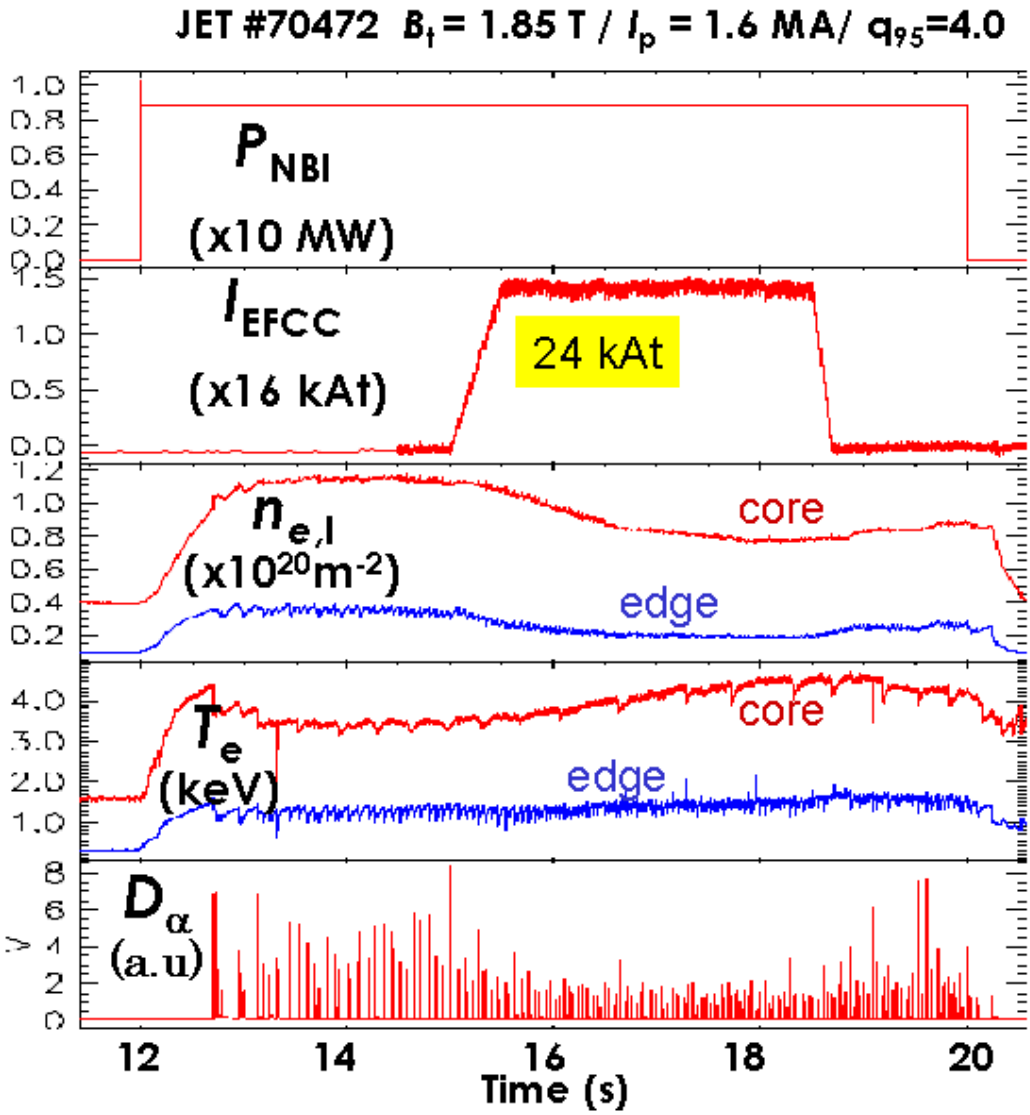

Figure 4.5: Overview on a typical experiment in $n = 2$ configuration. From [55].

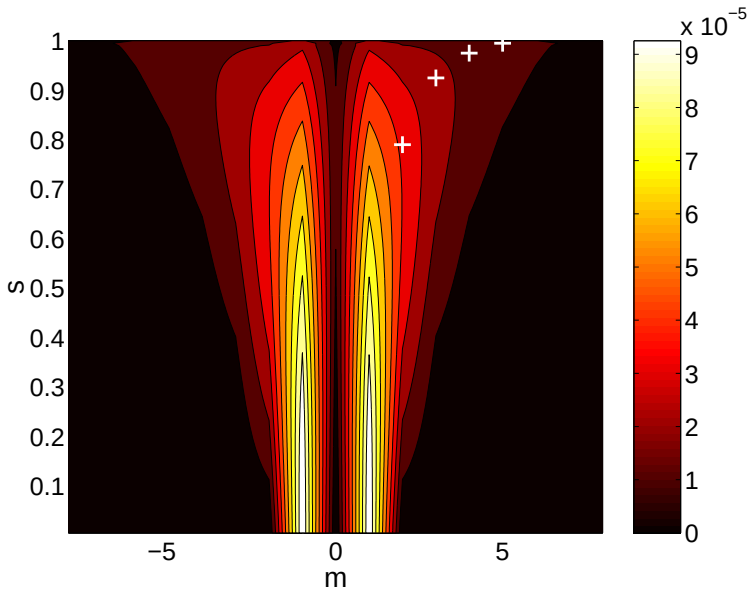

Figure 4.6: Spectrum of $2|\tilde{b}^1_{m,-1}|$ (dimensionless quantity) as a function of m and the radial coordinate s, for shot 67954 at 57.3s and for 1kAt in the EFCCs in $n = 1$ configuration, with crosses showing the position of the resonant harmonics, $\tilde{b}^1_{res}$.

for these four shots, the thresholds for ELMs mitigation[3] and the thresholds for locked mode triggering (or the maximal I_{EFCC} value of 36.8kAt for the shots with $q_{95} = 4.8$ and $q_{95} = 4.0$). It can be observed that the operational window becomes narrower as q_{95} becomes smaller, due to both an increase in the threshold for ELMs mitigation and a decrease in the threshold for locked mode triggering.

In what follows, we present calculations of the RMPs and Poincaré plots that we performed for these four shots and discuss on the possible interpretation of the dependency of the threshold for ELMs mitigation on q_{95}. In each case, we use the equilibrium calculated by the EFIT code [56] which we recalculate with more accuracy using the HELENA code [42] for the concerned shots at the time of onset of ELMs mitigation. On fig. 4.9, we present, for these four shots, the q profile together with symbolic magnetic islands produced by the $n = 1$, $n = 2$ and $n = 3$ components of the RMPs spectrum from the EFCCs. The plots are done at the time of onset of ELMs mitigation and with the corresponding experimental value of I_{EFCC} (which is considered to be the threshold current for ELMs mitigation). The corresponding RMPs profile for shot 67954 can be seen on fig. 4.10.
In order to make accurate estimations of the threshold currents for ergodization, the plots from fig. 4.9 are however not sufficient. Indeed, as explained for DIII-D in section 3.3, there are higher order islands that are not taken into account on these plots but that do play a role in the ergodization process. We thus use colored Poincaré plots, as presented in section 3.2.5 (fig. 3.8) and scan I_{EFCC} to see at which values the ergodic region extends

[3]It is considered here that the threshold current for ELMs mitigation is the value of I_{EFCC} at the time when ELMs mitigation starts. In other words, it is supposed that ELMs mitigation is an instantaneous effect. But, as stated above, shot-to-shot scans of I_{EFCC} would be more appropriate although more demanding in terms of experimental time.

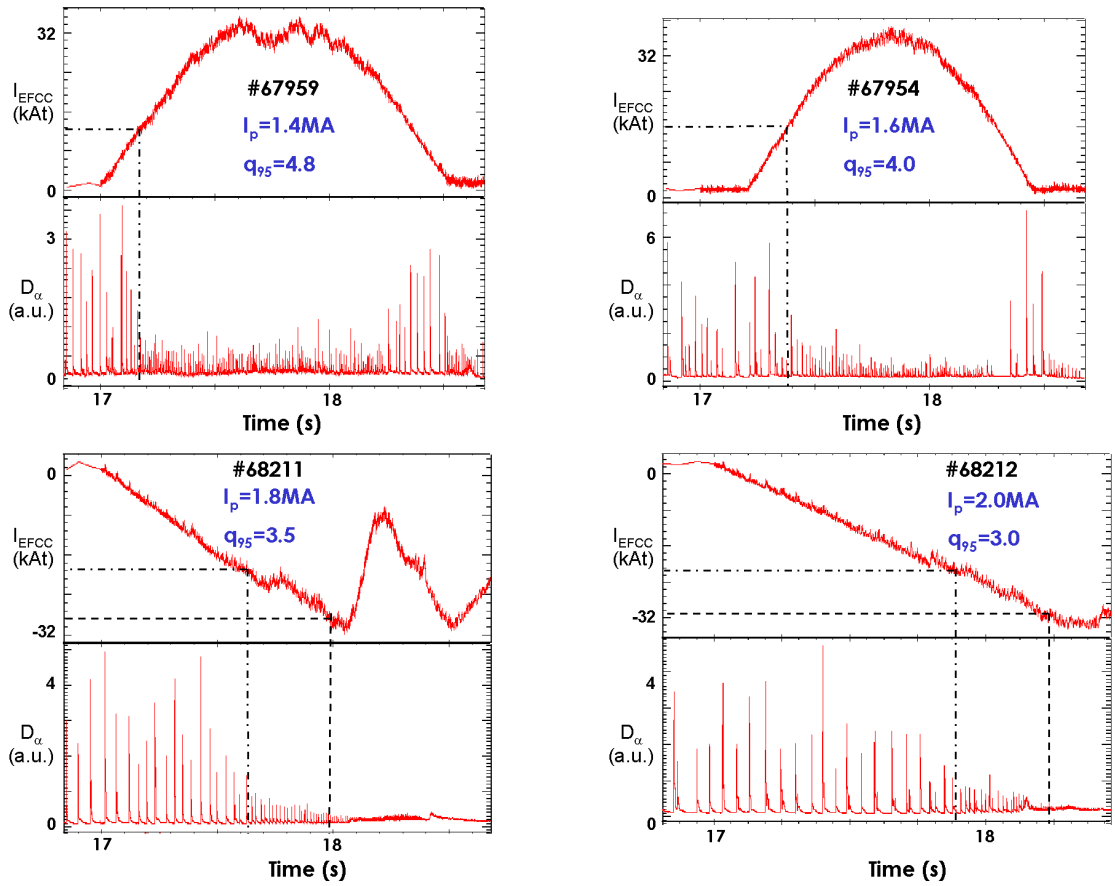

Figure 4.7: Time traces of I_{EFCC} and D_α for 4 shots with different q_{95} values. The dash-dotted (resp. dashed) lines indicate the time and I_{EFCC} of occurence of ELMs mitigation (resp. a locked mode [for the bottom cases only, since no locked mode occurred for the top cases]). From [51].

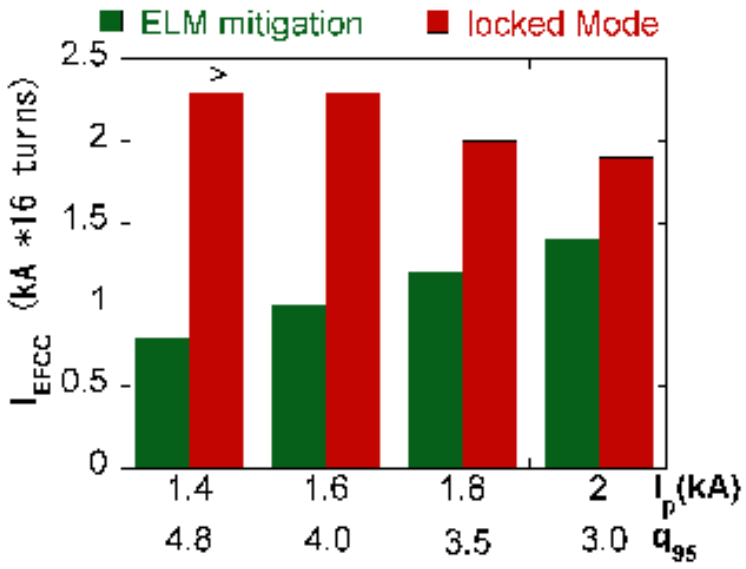

Figure 4.8: Operational window for ELMs mitigation for 4 shots with different values of q_{95}. For each shot, the threshold for ELMs mitigation is indicated by the left bar and the threshold for locked mode triggering (or the maximal I_{EFCC} value of 36.8kAt for the two left shots, since no locked mode was triggered in these shots) is indicated by the right bar. From [51].

abruptly from the edge towards the core by englobing one more $n = 1$ islands chain. An example is given for shot 67959 on fig. 4.11, where we see that the threshold for the ergodic region to extend from the 5/1 islands chain up to the 4/1 islands chain is between 12kAt and 14kAt roughly (notice that judging by fig. 4.9, it was not really possible to see that the ergodic region extended up to the 4/1 islands chain, because there seemed to be gaps in-between the $q = 4$ and $q = 5$ surfaces, which shows again the important role of higher order islands chains, in particular the 9/2 one here).
Repeting this for the four shots, we constructed table 4.2.2, in which we wrote, for each shot, the threshold current for the extension of the ergodic region from one $n = 1$ islands chains to the neighbouring one (going inwards radially), as well as the experimental threshold for ELMs mitigation. It appears on this table that, for shots 67959 and 68211, there is a good agreement between ELMs mitigation and extension of the ergodic zone up to the 4/1 (for 67959) or 3/1 (for 68211) islands chains. On the other hand, for shots 67954 and 68212, the experimental ELMs mitigation thresholds are somewhat above the required currents for the extension of the ergodic zone up to the 4/1 (for 67954) or 3/1 (for 68212) islands chains. It should be noticed, however, that an obvious source of error resides in the reconstruction of the q profile at the very edge. Indeed, in reality, q goes to infinity at the separatrix and so does the magnetic shear dq/ds, whereas in the reconstructed equilibirums that we used here, both q and dq/ds have a finite value at the separatrix. In the case of shots 67954 and 68212, where there are islands chains at the very edge (that play a non-negligible role in the results shown in table 4.2.2), we therefore strongly suspect that our results are "polluted" by the necessarily incorrect size of these islands chains. It is likely that in reality these islands are much smaller, so that the threshold currents we found for overlapping of these islands with the neighbouring chains of islands (towards the core) are underestimated. This qualitatively reconciles our results with the experimental thresholds for these two shots. Notice that for shots 67954 and 68211, we do not expect such problems, because there are no large islands chains really close to the separatrix. We should also mention that there are other possible sources of errors, among which:

- the fact that we have not taken into account the bootstrap current, which typically induces a local flattening of the q profile, changing the size and position of the islands chains;
- the difficulty to determine when exactly, on the experimental D_α traces, ELMs mitigation starts.

Nevertheless, our results tend to show that there is a correlation between ELMs mitigation and an extension of the ergodic region up to the second $n = 1$ islands chain from the separatrix[4]. We need to recall here that our modelling is done in the vacuum approximation. Our findings thus also tend to indicate that the vacuum approximation is correct.
Our results are consistent with recent DIII-D studies of the correlation between the extension of the ergodic region and the suppression of the ELMs [53]. In the JET experiments, the ergodic region extends typically to $s \sim 0.92 - 0.95$, whereas for DIII-D (in the q_{95} window) we had found an extension up to $s \sim 0.9$, see section 3.2.5. Thus, the ergodic region has a smaller radial extent in JET than in DIII-D, which could be at the origin

[4]We mean: in the reconstructed equilibria, where q has a finite value at the separatrix, and thus where "the second $n = 1$ islands chain from the separatrix" has a meaning.

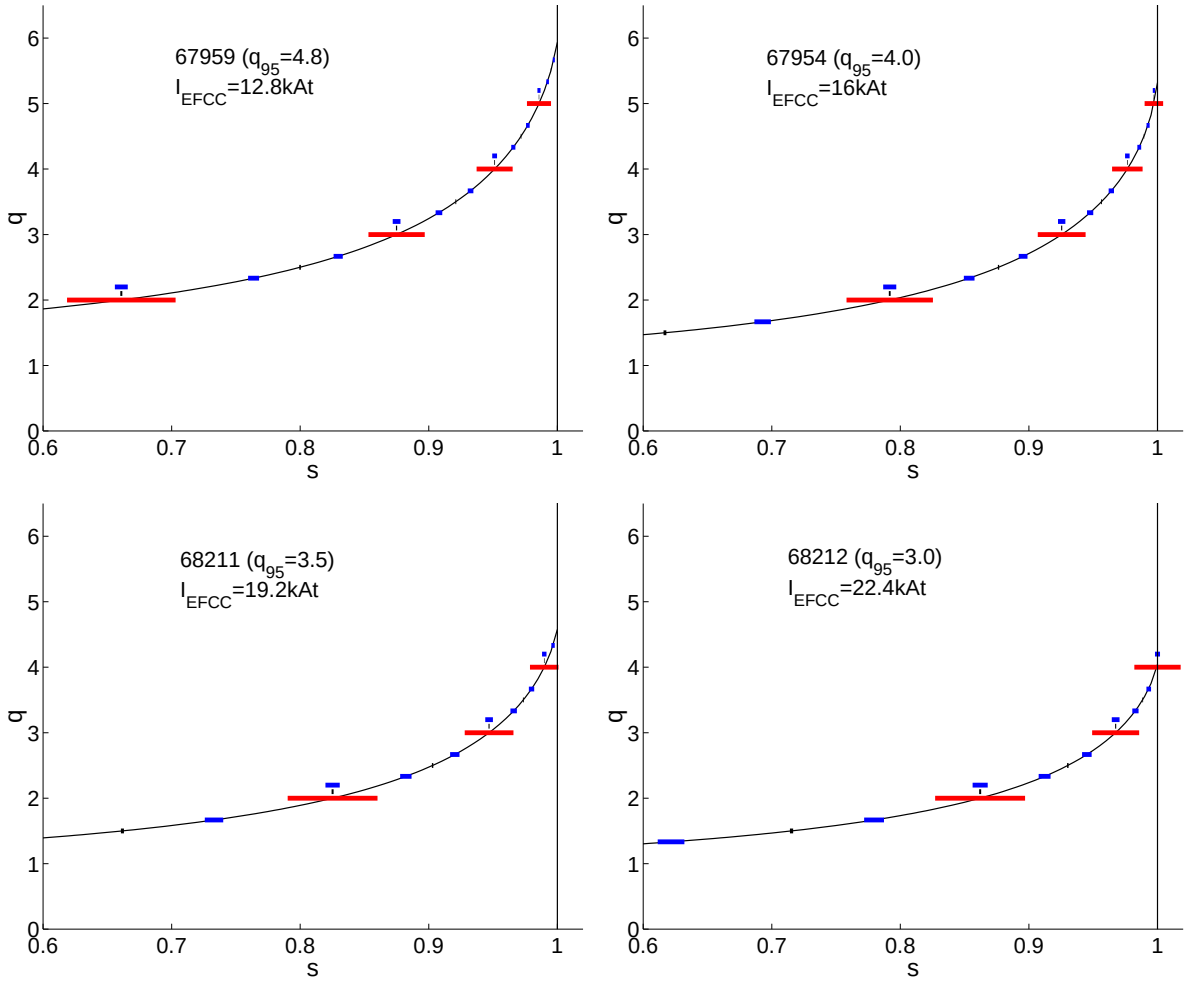

Figure 4.9: q profiles for the four shots of the q_{95} scan together with islands symbolized by horizontal bars, the widths of which were calculated as explained in chapter 3. Here are represented the islands generated by the $n = 1$ (lower, red bars), $n = 2$ (middle, black bars) and $n = 3$ (upper, blue bars) components of the RMPs spectrum produced by the EFCCs in $n = 1$ configuration. Each plot is done at the time of onset of ELMs mitigation, with the corresponding experimental current (considered to be the threshold current for ELMs mitigation).

of the difference in the impact of RMPs on ELMs. Calculations of the extension of the ergodic region in DIII-D experiments outside the resonant q_{95} window should be done in order to see if there is a similarity with the JET experiments.

Concerning the locked modes, although a precise modelling would be required, we can give a qualitative argument to explain why they are more eager to occur for the shots with the lowest q_{95} values. Looking at fig. 4.9, we can see that the radius of the $q = 2$ surface increases as q_{95} decreases. This means that the toroidal rotation and temperature at the $q = 2$ surface are smaller at small q_{95} (since these two quantities typically decrease when going from the core to the edge, see for instance fig. 4.4). Through its temperature dependency, resistivity (which is proportional to $T_e^{-3/2}$) is thus larger at the $q = 2$ surface for small q_{95}. Toroidal rotation and resistivity are two parameters play a key role in the process of mode locking and islands penetration, as will be explained in chapter 6, with a small value of the former and a large value of the latter corresponding to easier mode

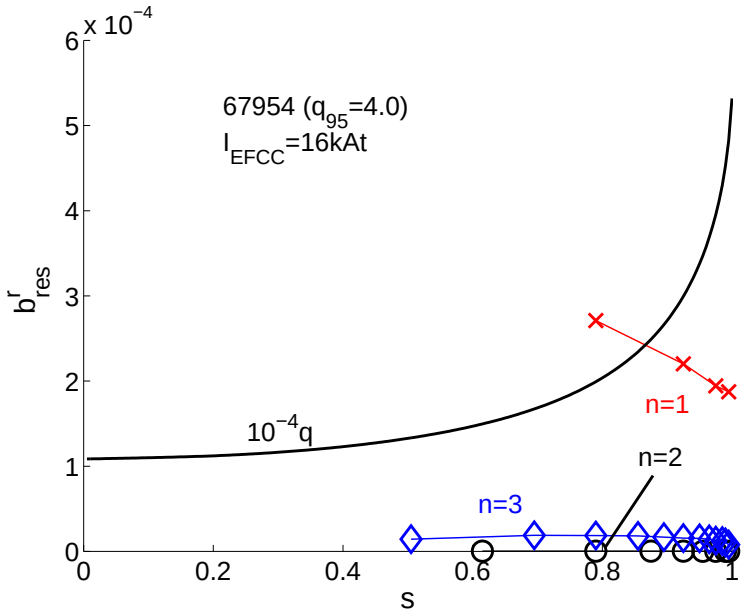

Figure 4.10: RMPs profile for shot 67954 with 16kAt in the EFCCs, corresponding to the upper right plot in fig. 4.9.

locking, we can understand why locked modes occur more easily at low q_{95}.

Magnetic footprints

In spite of the rather positive results described above, further study would be required in order to fully establish the relation between edge ergodization and ELMs mitigation. In this respect, an interesting feature to investigate in the future are the magnetic footprints in presence of the EFCCs. The term "magnetic footprint" designates the area where large heat and particles fluxes are deposited on the plasma facing components and in particular on the divertor. This corresponds in principle to the area where field lines arrive. Without any magnetic perturbation, i.e. with a pure axisymmetric equilibrium, magnetic footprints are typically reduced to the two so-called "strike points" (which are in fact lines rather than points), one on the high field side (the Inner Strike Point, ISP) and the other on the low field side (the Outer Strike Point, OSP). In presence of a magnetic perturbation, the strike points can widen and in certain toroidal locations split into several bands, exhibiting a non-axisymmetric aspect.
This effect has been studied in the past, in particular in view of reducing the thermal constraints on the divertor [57]. A convincing experimental investigation of magnetic footprints was done at TEXTOR in recent years [58]. For the DIII-D high collisionality ELMs control experiments, magnetic footprints were also calculated, showing a triple splitting of the outer strike point. These were compared to experimental D_α images and reconstruction of the heat flux from infrared camera images, which also showed a splitting of the strike point. The conclusion was that the experimental splitting was about 3 times larger than the one expected from field line tracing in the vacuum approximation, indicating a possible amplification of the RMPs by the plasma [59].
Here, we only present results from our numerical modelling for JET EFCCs in $n = 1$ configuration. A comparison to experimental measurements has not been done yet. On

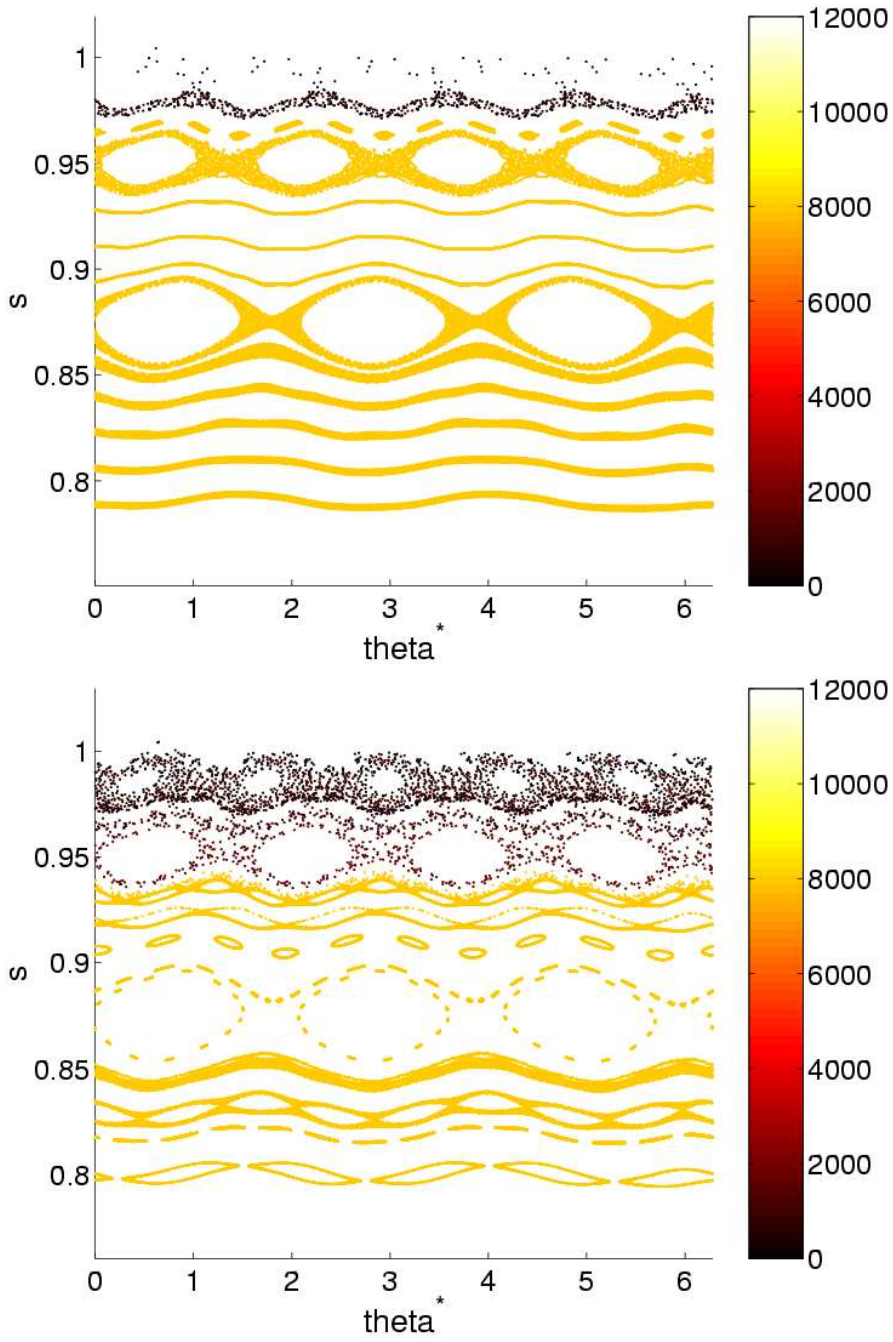

Figure 4.11: Colored Poincaré plots following the same rules as fig. 3.8 from section 3.2.5, for shot 67959, with $I_{EFCC} = 12$kAt (upper plot) and $I_{EFCC} = 14$kAt (lower plot).

Shot number	Overlap. of ... @ ...	Overlap. of ... @ ...	Overlap. of ... @ ...	Exp. thresh. for ELMs mitig.
67959 ($q_{95} = 4.8$)	sep.$\leftrightarrow q = 5$ @ 7-8kAt	$q = 5 \leftrightarrow q = 4$ @ 12-14kAt		$\sim$12.8kAt
67954 ($q_{95} = 4.0$)	sep. $\leftrightarrow q = 5$ @ 2-3kAt	$q = 5 \leftrightarrow q = 4$ @ 9-10kAt	$q = 4 \leftrightarrow q = 3$ @ 23-24kAt	$\sim$16kAt
68211 ($q_{95} = 3.5$)	sep. $\leftrightarrow q = 4$ @ 9-10kAt	$q = 4 \leftrightarrow q = 3$ @ 20-21kAt		$\sim$19.2kAt
68212 ($q_{95} = 3.0$)	$q = 4 \leftrightarrow q = 3$ @ 16-17kAt			$\sim$22.4kAt

Table 4.1: Table showing, for the 4 shots of the q_{95} scan, the calculated required currents for the extension of the ergodic region from a chain of $n = 1$ islands (or the separatrix) to the neighbouring one (going inwards radially), as well as the experimentally estimated required current for ELMs mitigation.

fig. 4.12, one can see the calculated footprints for shot 67954 at $t = 57.3$s for both the inner and the ISP and OSP, and for two values of I_{EFCC}: 20kAt and 40kAt. The plots are done in the following way. We follow 1000 field lines (10 departure points in s between 0.9 and 0.99, 10 in θ^* between 0 and 2π and 10 in φ between 0 and 2π) until they hit the horizontal plane $Z = -1.7$, Z being the usual vertical coordinate (if, however, a field line does not hit this plane before 200 toroidal rotations, we stop following it). This plane is used here as a very rough model for the divertor, but a more realistic geometry of the divertor could be included in the model. We then represent the hit points as a function of the major radius R and the toroidal angle φ. Fig. 4.12 evidences the appearance of a clear non-axisymmetric structure, at both the ISP and OSP. Its width varies with φ, with a maximum of about 7cm at the ISP and 4cm at the OSP for 20kAt. If this structure really exists, it should thus be easy to observe experimentally (and easier to observe at the ISP than at the OSP), either from D_α measurements or infrared imaging or Langmuir probe measurements (JET is equipped with an array of Langmuir probes covering a large part of the divertor). Furthermore, the comparison of the 20kAt and 40kAt plots shows that the width of the structure grows almost linearly with I_{EFCC}, meaning that it is a quite sensitive diagnostic to measure the RMPs amplitude. The potential powerfulness of the method thus seems clear and appeals for an analysis of the experimental data.

4.2.3 Modelling for the $n = 2$ experiments

We will be more brief on the modelling of the $n = 2$ experiments and show only the RMPs spectrum (fig. 4.13), a q profile together with symbolic islands (fig. 4.14) and a colored Poincaré plot (fig. 4.15) for a typical shot. It can be noticed that the $n = 1$ component of the RMPs is considerable, as appears on fig. 4.13. This is due to the fact that one of the EFCCs (the coils in octant 3) is not exactly built on the same model as the three others (which are exactly identical to each other): its vertical bars are closer to the plasma than for the other coils. On fig. 4.14 one can see that if we calculate the islands widths from the $n = 1$ and $n = 2$ components independently, we find, on integer q surfaces, $n = 1$ and $n = 2$ islands of approximately the same width. In reality, on these surfaces, there are neither pure $n = 1$ nor pure $n = 2$ islands but combinations of the

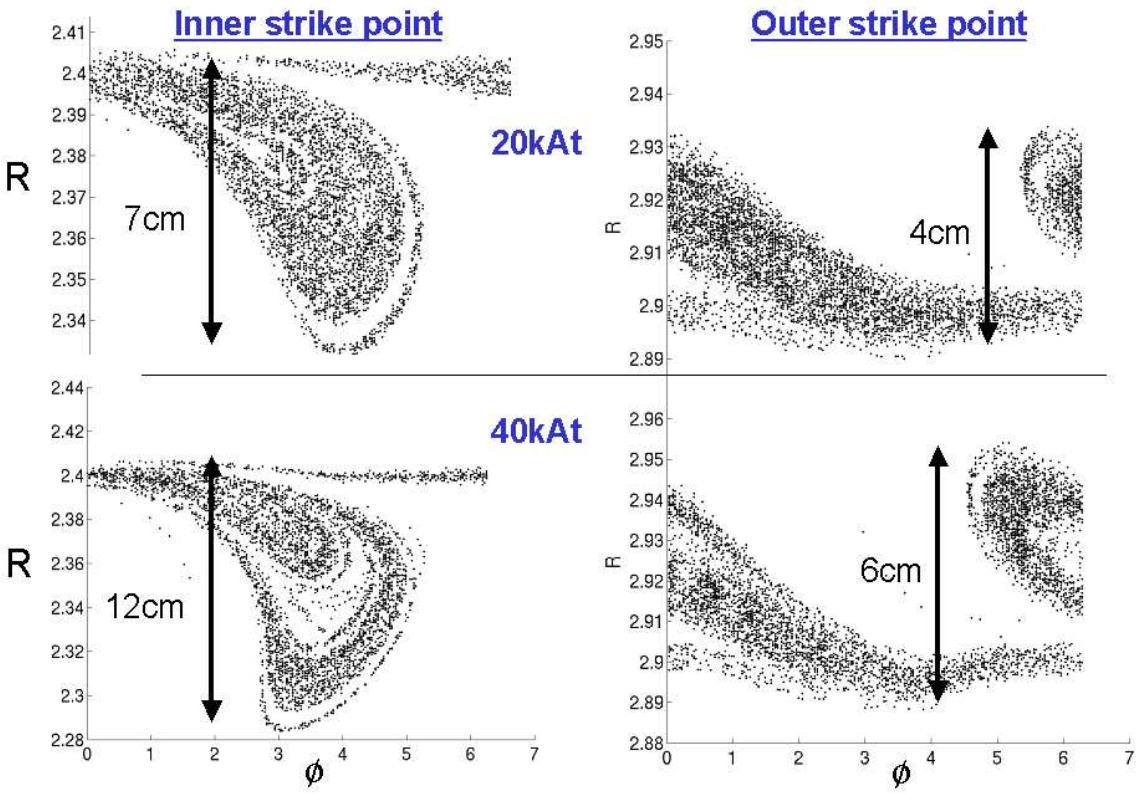

Figure 4.12: Calculated magnetic footprints for shot 67954 at the ISP (left plots) and OSP (right plots), for I_{EFCC} =20kAt (upper plots) and I_{EFCC} =40kAt (lower plots).

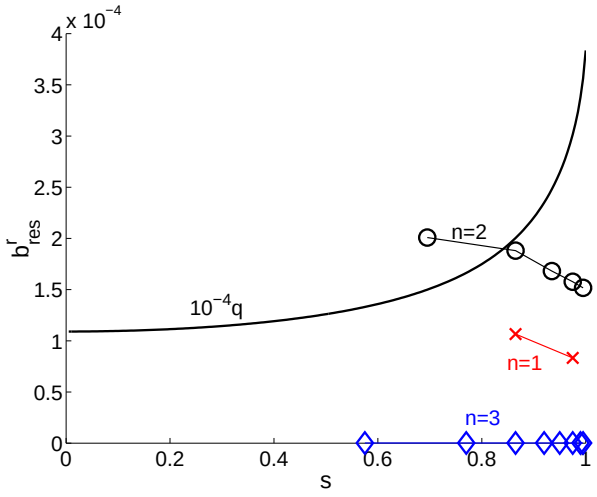

Figure 4.13: Effective normalized radial RMPs profile for shot 70475 with the EFCCs in $n = 2$ configuration and I_{EFCC} =24kAt (the experimental value).

two which appear as "peanut-like" structures, as can be observed on the Poincaré plot (fig. 4.15). From the Poincaré plot, one can also see that the magnetic field at the edge is ergodized up to $s \simeq 0.95$. These calculations demand to be pursued and an analysis of a q_{95} scan, similar to the one done for the $n = 1$ configuration, would be interesting.

4.3 ELMs control by the Error Field Correction Coils at MAST

So-called "spherical tokamaks" are characterized by a small aspect ratio R/a (major over minor radius), typically around 1.3, while standard tokamaks have aspect ratios of the order of 3 to 4. The Mega Amp Spherical Tokamak, referred to as "MAST", with $R \simeq 0.85$m and $a \simeq 0.65$m, belongs to this category (other typical MAST parameters are a plasma current $I_p \leq 2$MA and a vacuum toroidal magnetic field at $R = 0.85$m, $B_\varphi \simeq 0.6$T). MAST can run in H-mode and is subject to ELMs [60].
The MAST EFCCs (see fig. 4.16) are very similar to the JET EFCCs in the sense that there are 4 square coils equally spaced toroidally, which can be phased in $n = 1$ or $n = 2$ configurations. The maximal current is 5kA times 3 turns, i.e. 15kAt. Similarly to JET, experiments aiming at controlling the ELMs were done successively in $n = 1$ and $n = 2$ configurations and we will briefly describe them in what follows.

Experiments in $n = 1$ configuration

We participated on site to the $n = 1$ experiments. Preliminary calculations with ERGOS (see figs. 4.17 and 4.18) showed the ability of the EFCCs in $n = 1$ configuration to push the Chirikov parameter above 1 for $s \geq 0.95$, corresponding approximately to the DIII-D reference case.
In a first series of shots, the EFCCs were turned on before the L to H transition and it was observed that they affected the transition (typically the transition occurred more lately in the discharge). In order to be able to make a clean comparison to the reference

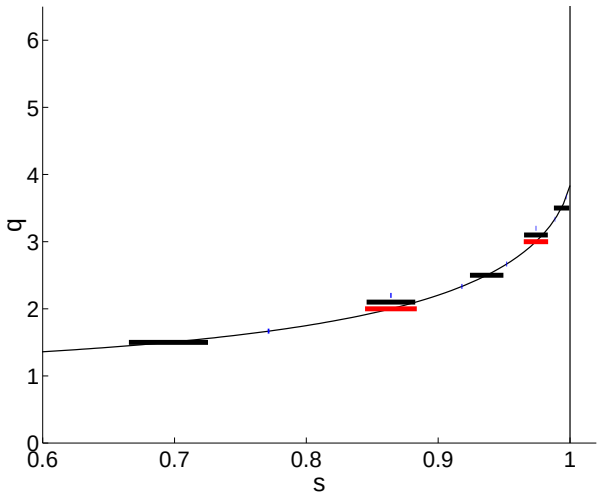

Figure 4.14: q profile for shot 70475 together with islands symbolized by horizontal bars, the widths of which were calculated as explained in chapter 3. Here are represented the islands generated by the $n = 1$ (lower, red bars), $n = 2$ (middle, black bars) and $n = 3$ (upper, blue bars) components of the RMPs spectrum produced by the EFCCs in $n = 2$ configuration.

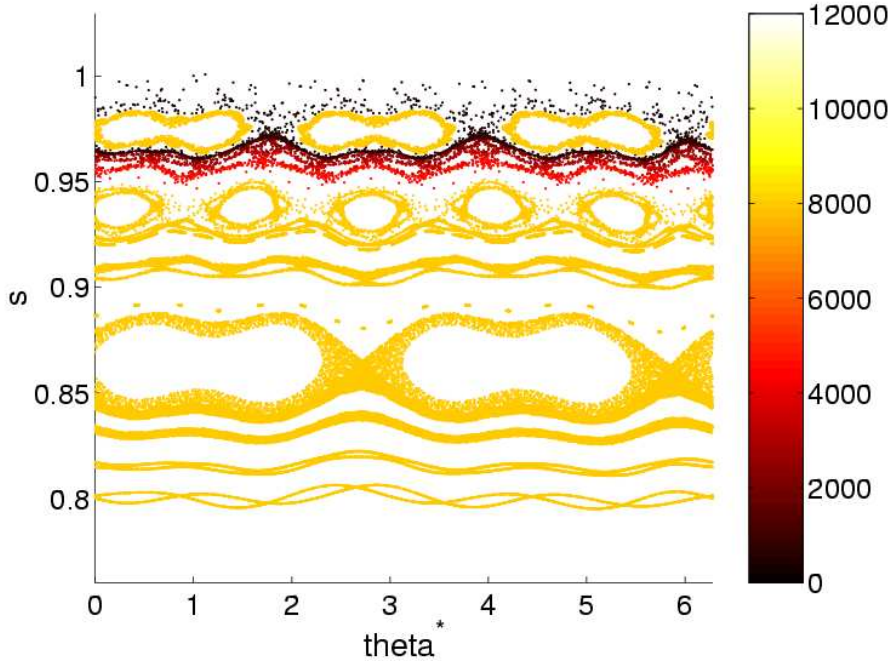

Figure 4.15: Colored Poincaré plots following the same rules as fig. 3.8 from section 3.2.5, for shot 70475, with the EFCCs in $n = 2$ configuration and $I_{EFCC} = 24$kAt.

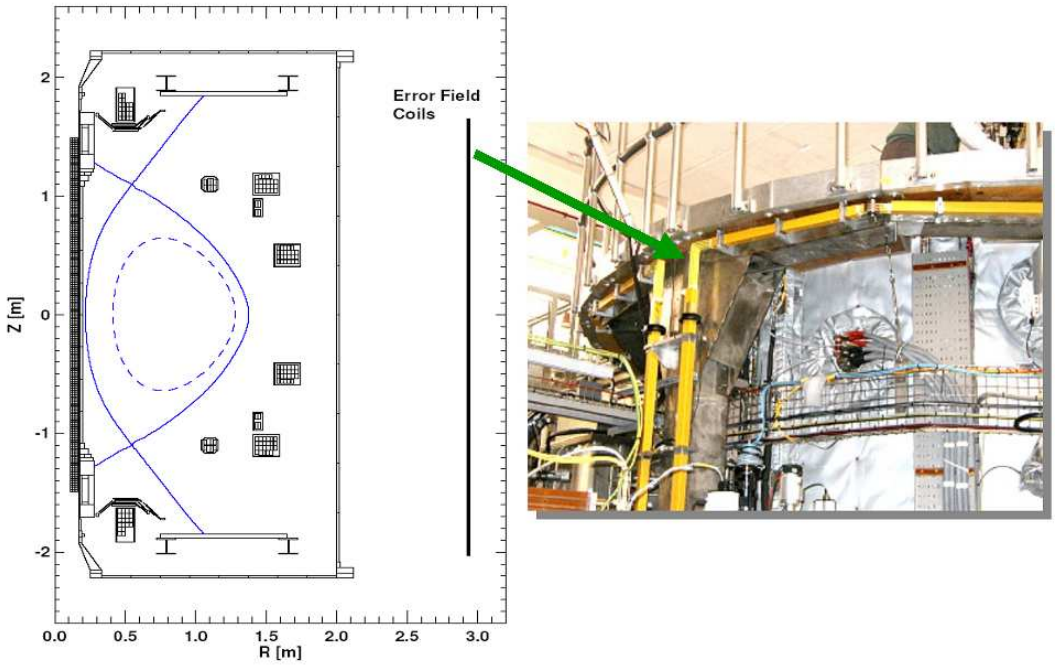

Figure 4.16: Design of the MAST EFCCs. (courtesy A. Kirk)

case (without EFCCs), it was thus decided to turn on the EFCCs after the L to H transition. An effect of the EFCCs on the ELMs could not be clearly observed, but this could be due in part to the fact that the reference case had only a few (and furthermore irregular) ELMs during the whole shot[5], see fig. 4.19. A slight pump-out (decrease of the density), remindful of the DIII-D and JET results, and a slight increase of the electron temperature at the top of the pedestal were nonetheless observed when comparing the shot with EFCCs on to the reference case without EFCCs, see fig. 4.20. However, in many cases, a locked mode (again remindful of the JET experiments with the EFCCS in $n = 1$ configuration) and/or an H to L backtransition were observed.

Experiments in $n = 2$ configuration

In the experiments in $n = 2$ configuration, two of the four EFCCs (the "A" coils) were kept in error field correction mode in order to compensate for the $n = 1$ error field of the machine, and the two others (the "B" coils) were used in order to produce $n = 2$ RMPs. Calculations again showed the possibility of pushing the Chirikov parameter above 1 for $s \geq 0.95$ in this configuration if the B coils were fed with ∼12kAt. The experiments showed a possible effect of the EFCCs on the ELMs (see fig. 4.21) with no locked mode or H to L backtransition, but again the reference case did not display frequent and regular enough ELMs in order to make a clear statement. The drop in the pedestal density and increase in the pedestal temperature seen in the $n = 1$ experiments were also observable

[5]This was because of the relatively low value of P_{inj} (only one neutral beam injector was operational), which made the rebuilding time of the pressure profile after an ELM rather long.

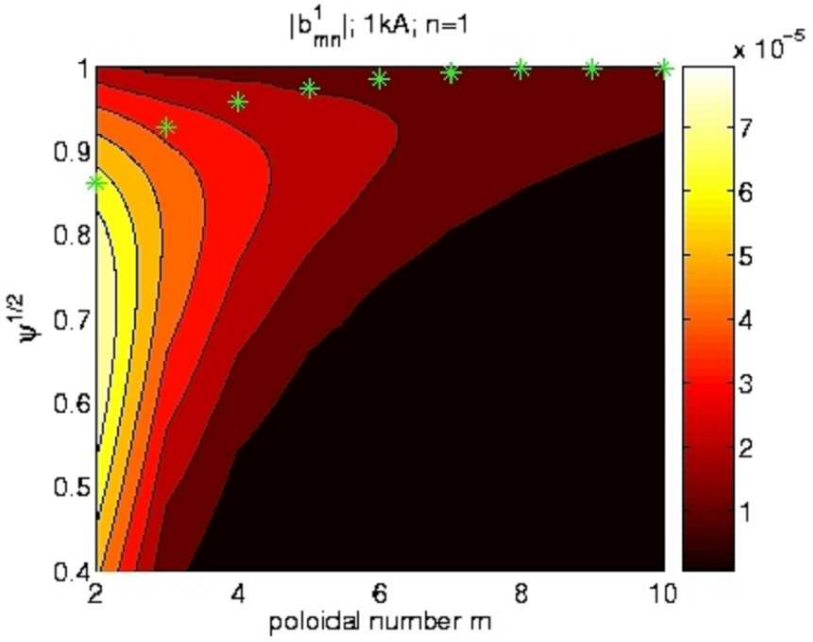

Figure 4.17: Spectrum of $|b^1_{m,1}|$ (dimensionless quantity) as a function of the poloidal mode number and the radial coordinate for 1kAt in the EFCCs in $n = 1$ configuration, with stars showing the position of the resonant harmonics.

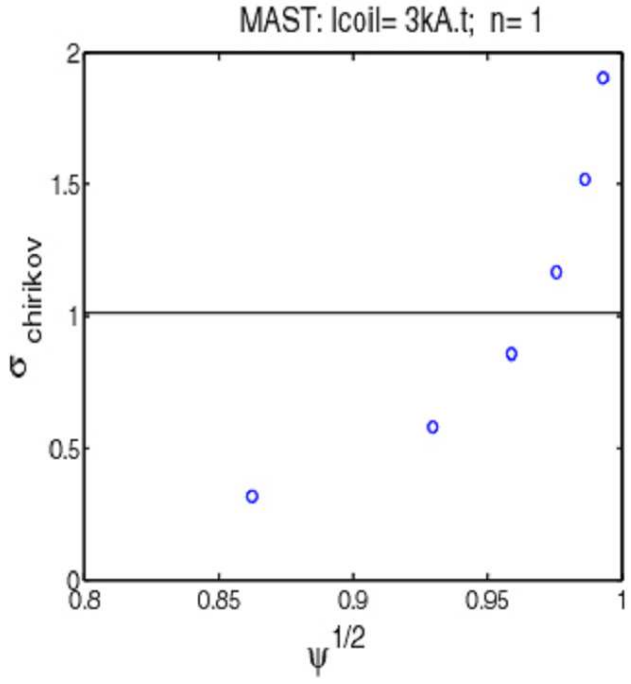

Figure 4.18: Profile of the Chirikov parameter for 3kAt in the EFCCs in $n = 1$ configuration.

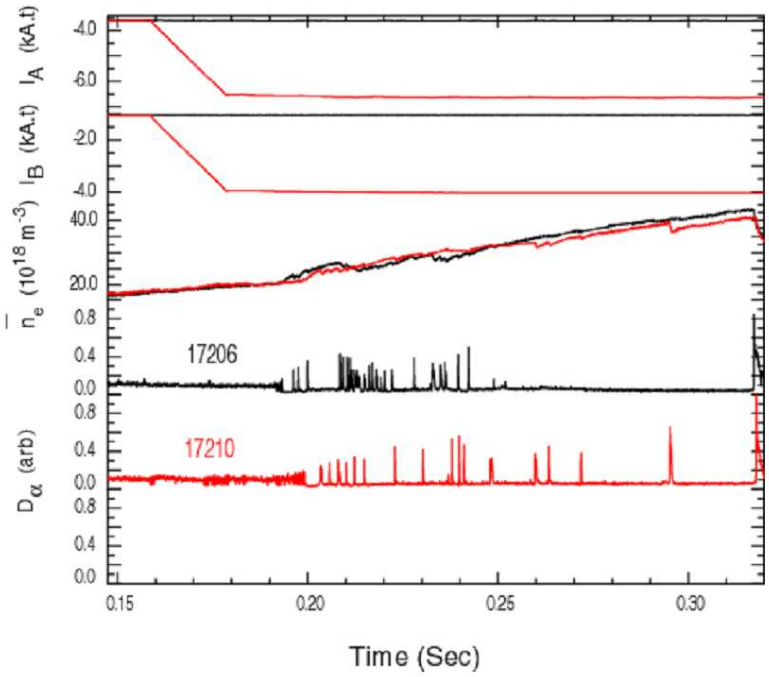

Figure 4.19: Comparison between a reference shot (17206, black traces) and a shot with the EFCCs in $n = 1$ configuration fed with 3kAt (17210, red traces). The traces represent, from top to bottom, the current in EFCCs A (two of the four EFCCs), the current in EFCCs B (the other two), the line-integrated electron density (which rises all along the discharge, a typical feature of MAST), and the D_α traces for the two shots. (courtesy A. Kirk)

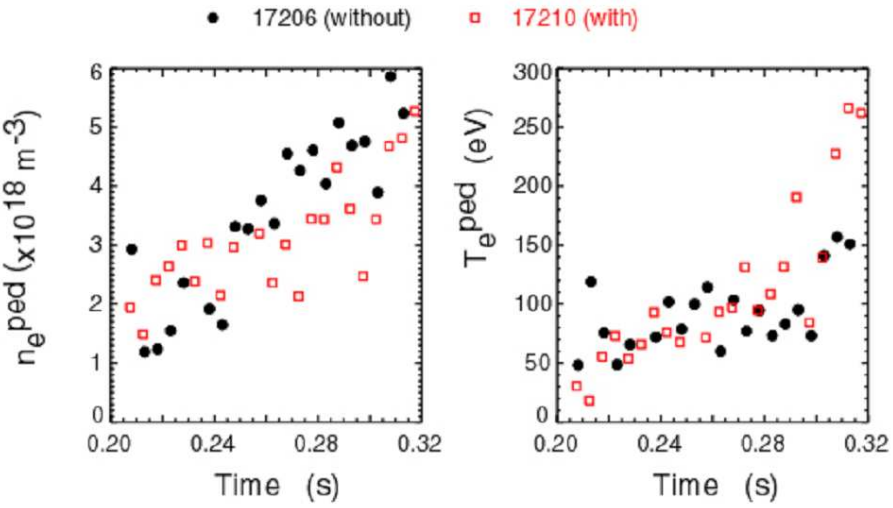

Figure 4.20: Experimental measurements at the top of the pedestal, of the electron density (left) and electron temperature (right) for the same shots as in fig. 4.19. (courtesy A. Kirk)

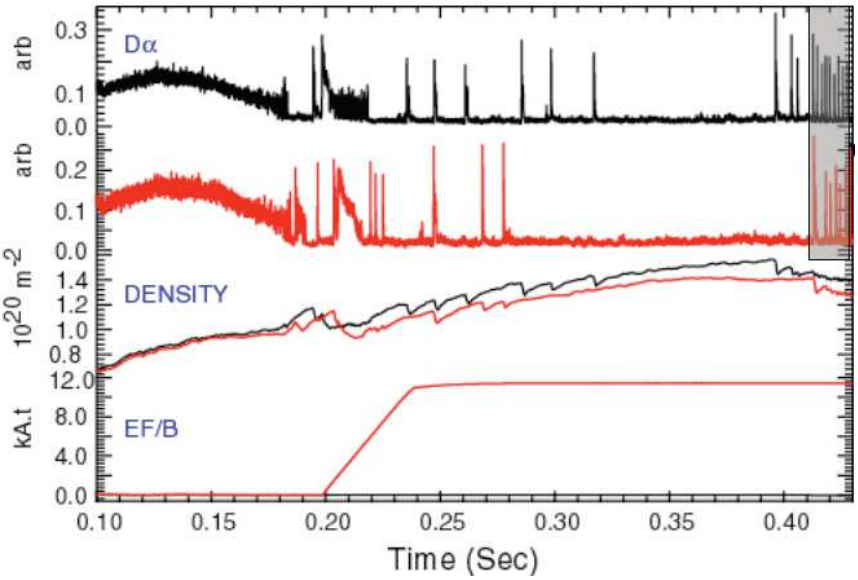

Figure 4.21: Comparison between a reference shot (black traces) and a shot with EFCCs B in $n = 2$ configuration fed with 12kAt. From top to bottom: D_α emission for the reference shot and the shot with EFCCs (the ELMs observable in the shadowed area on the right are due to the current ramp-down at the end of the discharge), line-integrated electron density, and current in EFCCs B. (courtesy A. Kirk)

in the $n = 2$ experiments.

4.4 Summary

Experiments were done at JET and MAST aiming at controlling the ELMs with coils that were designed for other purposes: the EFCCs. Preliminary ERGOS calculations showed that EFCCs, which can run either in $n = 1$ or $n = 2$ configurations, were able to ergodize the magnetic field at the edge of the plasma on both machines and in both configurations. These calculations constituted a support in order to prepare the experiments and require machine time to do them.

The experiments on JET were successful at mitigating the ELMs, the typical effect being an increase in their frequency associated to a decrease in their amplitude (both by a factor ~ 4). This effect is different from what was observed at DIII-D inside the resonant q_{95} window but remindful of what was observed outside this window. Furthermore, the main effect of the EFCCs on the profiles was to lower the density, the effect on the electron temperature being smaller, very similarly to the DIII-D observations. The fact that there is such a similarity between the JET and DIII-D results in spite of the very clear difference in the system of coils used ($n = 1$ or $n = 2$ monopole coils versus $n = 3$ multipole coils) suggests that the physical mechanisms at play do not depend on the exact aspect of the perturbation coils but rather on their ability to ergodize the magnetic field at the edge.

The experiments on MAST showed a possible effect of the EFCCs on the ELMs, but

the judgement was made difficult by the fact that there were only a few irregular ELMs in the reference shots with the EFCCs off.

In both machines, the experiments in $n = 1$ configuration showed locked modes whereas $n = 2$ experiments did not show any locked mode. This suggests that the design of ELMs control coils for other tokamaks and in particular for ITER should have n as high as possible. It is interesting to notice that in the $n = 1$ experiments, the eagerness of the locked mode to occur was correlated to the fact that q_{95} was rather low, meaning that the $q = 2$ surface was near the edge of the plasma, where rotation is slower and resistivity larger.

At JET, a scan in q_{95} showed that the threshold current for ELMs mitigation increases as q_{95} decreases. An ERGOS modelling was done in order to determine if there is a correlation between the threshold for ELMs mitigation and the threshold for edge ergodization. Among the four shots from the q_{95} scan that we studied, two showed very good correlation while for the two others we could identify clearly the reason for the less good correlation, which resides in the unperfect equilibrium reconstruction. We can thus say that ELMs mitigation seems well correlated with edge ergodization, although more work should be done to confirm this statement.

We also calculated the theoretical magnetic footprints (in the vacuum hypothesis) for JET, which show a clear asymmetric structure and are broad enough ($\sim$ 5cm) to be observable experimentally. Experimental data should be analyzed and compared to our calculations and this could constitute a powerful tool to determine the actual amplitude of the magnetic perturbations in the plasma and test the vacuum hypothesis.

Chapter 5

Design of ELMs control coils for ITER

5.1 Context

The idea to use RMPs for ELMs control in ITER was proposed in 2002 as a collaborative effort between CEA and General Atomics (the company owning the DIII-D tokamak) [62] but was considered as a somewhat hypothetical method until its successful experimental demonstration on DIII-D (see chapter 2). The DIII-D results were a strong motivating factor for our group to investigate, on the one hand, the physical mechanisms at play in ELMs control by RMPs, and on the other hand, the possibilities of designs of ELMs control coils for ITER [63, 65, 64] (as well as for other existing machines: JET [45], MAST and COMPASS-D).
Our pioneer work on the subject of designing ELMs control coils for ITER was acknowledged by the attribution to our group of the two years (end 2005 - beginning 2007) modelling European Fusion Development Agreement (EFDA) Task CEFDA05-1336 TW5-TPO-"ERGITER": "Design studies of Resonant Magnetic Perturbation (RMP) coils for Type I ELMs mitigation in ITER". Almost all of the results presented in this chapter were obtained in the frame of this EFDA-CEA contract. This work was realised in a wide international collaboration and in particular with EFDA and ITER engineers in order to establish technical and spatial constraints and propose realistic designs for ITER. The main results on the ERGITER contract were published in [64, 66, 67, 68, 69].
Moreover, later on (in the spring of 2007), the ITER Design Review activity started, aiming at improving the present ITER design by including new physics and technology. During this process, the installation of RMPs coils for ELMs control is recognized as a first order priority. In this activity a strong effort is coming from associations including our group, as well as the US Burning Plasma Organisation (USBPO) group [70], the two working in close collaboration. Most of the following results were used in the development of the final design of RMPs coils for ITER. At the time this manuscript is being written down, the final decision is not taken. However, two options are likely to be retained by our ITER design review group: coils wound around the equatorial port plugs or coils similar to the ones wound around the blanket modules (see section 5.5.2) but possibly installed at a slightly different location (for instance just behind the blanket and the first wall of the vacuum vessel).

5.2 Goal and constraints

The assumption that underlies all the work of design for ELMs control coils for ITER is that ELMs mitigation is due to the ergodization of the magnetic field at the edge. From the vacuum calculations done for the DIII-D case with the even parity I-coils fed with 4kAt (see chapter 3), we saw indeed that the magnetic field is ergodized at the edge. More precisely, the Chirikov parameter gets above the value of 1 for $s \geq 0.95$ (s being the square root of the normalized equilibrium poloidal magnetic flux, as defined in section 3.2.2), with a maximal value (at the very edge) of $\simeq 3$, and there is an ergodic layer extending from the edge of the plasma towards the core up to $s \simeq 0.9$. This case constitutes our **reference case**.
Since we do not know exactly what features are required in order to achieve ELMs control (large enough width of the ergodic layer? large enough value of the Chirikov parameter at the very edge? ...) and since all of the DIII-D features cannot *a priori* be matched together, there is necessarily some uncertainty on the value of the current required in the coils.
Furthermore, the possibility of matching the DIII-D case should exist **for the three ITER reference scenarios** (standard H-mode, hybrid scenario and steady-state scenario [also referred to as "Internal Transport Barrier" (ITB) scenario]) [71]. It should also be a **robust property** with respect to the value of plasma parameters such as the poloidal beta β_p and internal inductance l_i (see section 5.6 for the definition of these parameters), which can vary during a discharge.
We call attention on the fact that the requirement of ergodicity at the edge is different from a requirement in terms of amplitude of the RMPs, b^r_{res}. The importance of this remark will appear in particular when considering the case of the hybrid and steady-state scenarios for which we will see that, in spite of the fact that b^r_{res} will in general smaller than for the standard H-mode, edge ergodization will still be possible thanks to the higher magnetic shear.

In terms of constraints, one can distinguish "technical constraints" and "physics related constraints".

Technical constraints are:

- that the coils should be concretely possible to insert into the ITER design (i.e. basically that there should be room for them and for their current supplies);
- that the coils should be able to hold the mechanical forces they will undergo in the machine, in particular Laplace ($\vec{j} \times \vec{B}$) forces, in steady-state conditions as well as during abnormal events such as disruptions (which could exert severe constraints on the coils);
- that the coils should be able to hold the thermal constraints coming from Joule heating and possibly heating by the fusion neutrons;
- that the coils should resist the neutron flux coming from the plasma;
- if possible, that the coils should be maintainable.

The fulfillment of the technical constraints cannot be easily translated into general rules: each design should be studied specifically. However, one feature that has a key role with respect to most of the technical problems mentioned above is the current required in the coils. Thus, we will be particularly looking for designs with a **required current as small as possible**.

Physics related constraints mainly concern **core perturbations** and **plasma rotation braking**[1] (the two being strongly linked together), which **should both be minimized**. Let us discuss this. In the DIII-D and JET ELMs control experiments, the toroidal rotation was due principally to the momentum source from the Neutral Beam Injection (NBI). This will also be the case in ITER [71]. There are two mechanisms by which external magnetic perturbations can brake down the plasma (both of which have theoretical as well as experimental backgrounds):

- resonant braking [75] caused by $\vec{j} \times \vec{B}$ forces localized at the resonant surfaces (see chapter 6 for more details) and function of only the resonant components of the magnetic perturbations (i.e. the RMPs);
- non-resonant braking due to the so-called "neoclassical toroidal viscosity" [76, 77, 78], which is due to both the resonant and non-resonant components of the magnetic perturbations.

A too large braking down of the plasma rotation can lead to the growth of so-called "Resistive Wall Modes" (RWMs) [73], which are MHD modes usually stabilized by the finite penetration time of magnetic perturbations into the wall of the machine combined to plasma rotation. It can also lead to the penetration of the magnetic islands induced by the RMPs [75] (which we want to happen at the edge but not in the core), a phenomenon which we will briefly explain here, and which will be studied in chapter 6. In general, in presence of rotation, static RMPs coming from external sources are screened (i.e. islands are smaller than the vacuum islands) by currents that are induced around the resonant surfaces. The larger the rotation and the smaller the plasma resisitivity, the more efficient the screening (hence, the screening is generally much more efficient in the core than in the edge plasma, because of both larger rotation and larger temperature, i.e. smaller resistivity). However, when the rotation is reduced, the screening becomes less efficient and also the resonant braking by $\vec{j} \times \vec{B}$ forces around the resonant surfaces becomes stronger, so that the plasma rotation can be almost completely stopped in the region neighbouring a resonant surface, and RMPs can penetrate (i.e. islands can reach the size of vacuum islands[2]), a phenomenon known as "mode penetration". Large core islands cause, at least, a degradation of the energy confinement time τ_E, since the very strong parallel transport short-circuits the perpendicular transport on the width of the islands. But they can also be at the origin of so-called Neoclassical Tearing Modes (NTMs) [73]. These modes are MHD modes which are linearly stable, but which can grow non-linearly if there exist so-called "seed islands" in the plasma. NTMs can have deleterious effects, in particular the low-n ones, such as the $m/n = 2/1$ and $3/2$ ones, which are known to be the departure point of certain disruption scenarios. Seed islands can be of different origins (for instance, they can be induced by a sawtooth crash) and there is a critical

[1] We speak here about the toroidal rotation, since the poloidal rotation is expected to be fixed to its neoclassical value by the so-called "neoclassical poloidal viscosity" [74].

[2] or even larger in case of an amplification by plasma effects [75]

islands width above which islands become seed islands that trigger an NTM. In designing ELMs control coils for ITER, we should therefore ensure that the coils will not create core islands above the critical size for NTM triggering[3].

The abovementioned physical considerations linked to core MHD phenomena and plasma rotation are complex, because they involve non-linear phenomena and cannot *a priori* be considered independently from each other. Quantitative constraints on the magnetic perturbations created by the ELMs control coils cannot be given for now, but on the qualitative point of view, it seems clear that we have to look for coils that produce:

- **as small as possible core RMPs**;
- **as small as possible non-resonant perturbations**.

A last physical constraint is that the ELMs control coils should not produce too much "ripple", i.e. non-axisymmetric modulations of the intensity of the magnetic field along field lines [2]. In ITER, ripple is expected to be detrimental with respect to the confinement of fast ions coming either from fusion reactions (α particles) or from heating systems (NBI, Ion Cyclotron Resonance Heating [ICRH]) [35]. A common source of ripple in tokamaks is the finite number of Toroidal Field (TF) coils (see section 5.5.4) but it is forecasted to install ferritic inserts in ITER in order to compensate for most of this ripple [35]. When designing ELMs control coils, we should thus ensure that they do not create a too large additional ripple.

5.3 Method

The results presented below were obtained with the ERGOS suite of codes presented in chapter 3. All of the notations used below without being explicitely defined (such as s, σ_{Chir}, etc.) were already defined in that chapter. In order to produce realistic designs, we had to take into account the geometry of the machine and available space. We will see in section 5.5 that there is in fact not much space available to put the coils. The number of possibilities to be investigated was nonetheless quite large *a priori*. However, we limited this number by first studying which toroidal mode number n of the magnetic perturbations was most appropriate, as presented in section 5.4. We found that $n = 3$ is the most promising choice. This led us to restrict ourselves to studying $n = 3$ concepts, which are presented and compared in section 5.5. In these first two sections, the calculations were done for a standard H-mode equilibrium, with a fusion amplification factor $Q = 10$, a fusion power $P_{fus} = 400$MW, a plasma current $I_p = 15$MA, a vacuum toroidal magnetic field on axis $B_0 = 5.3$T, a safety factor at 95% of the poloidal magnetic flux $q_{95} = 3.15$, a poloidal beta $\beta_p = 0.64$ and an internal inductance $l_i = 0.8$. We obtained this equilibrium by running the HELENA code [42], taking as inputs the separatrix position and pressure and safety factor profiles from the ASTRA simulation described in [72]. The sensitivity of the coils performances on the scenario, in particular on the q profile, which changes significantly between the three ITER reference scenarios, as shown on fig. 5.1, as well as on β_p and l_i, and its impact on the evaluation of the different designs, are discussed in section 5.6. Finally, section 5.7 makes a synthesis of the results.

[3]It must be noticed however that there exist means of control of the NTMs, see [73].

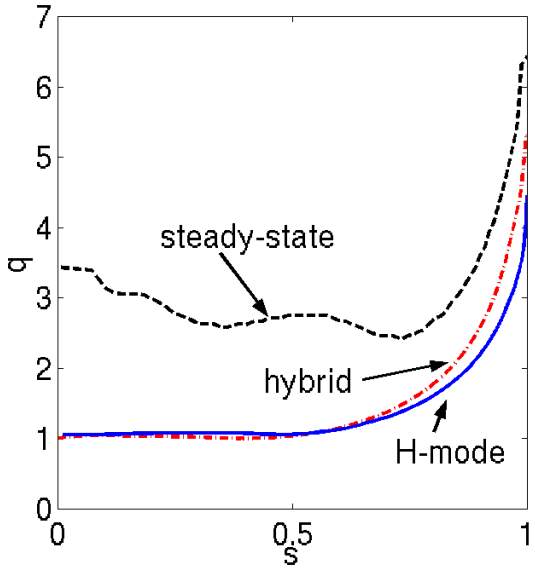

Figure 5.1: q profiles for the three reference ITER scenarios, modelled in [72], which we used in the present study.

5.4 Selection of the toroidal mode number of the coils configuration

It is a key point of the present design study that the selection of the toroidal and poloidal structures of the coils configuration[4] are made independently, one after the other. From a practical point of view, this allows us to strongly reduce the number of possibilities to investigate. The justification for making the selection of the toroidal and poloidal structures independently will appear be given at the end of the next subsection.

5.4.1 Single n possibilities

In order to compare the different possibilities for n, we did a series of calculations for a particular type of coils, namely large coils fixed on the Poloidal Field (PF) coils (see fig. 5.23) and centered on the midplane. We varied n from 1 to 5, i.e. we varied the number of coils from 2 to 10. Fig. 5.2 presents the $n = 1$, $n = 3$ and $n = 5$ designs. Each coil is fed with a current of 200kAt, which is an acceptable current for such coils, and the direction of the current alternates as one moves toroidally from one coil to another.

Fig. 5.3 represents the widths of the islands and the profiles of the Chirikov parameter obtained for these five designs. One can see that the widths of the islands decrease strongly as n increases. This is due to both the n dependency of the islands half-widths (at constant $\tilde{b}^1_{res}$):

$$\delta = \left(\frac{4q^2\tilde{b}^1_{res}}{q'm}\right)^{1/2} = \left(\frac{4q\tilde{b}^1_{res}}{q'n}\right)^{1/2} \propto n^{-1/2} \tag{5.1}$$

and to the fact that RMPs are stronger for lower n's, as can be seen on fig. 5.4.

[4] i.e. basically number of coils and extension of the coils in the toroidal and poloidal directions

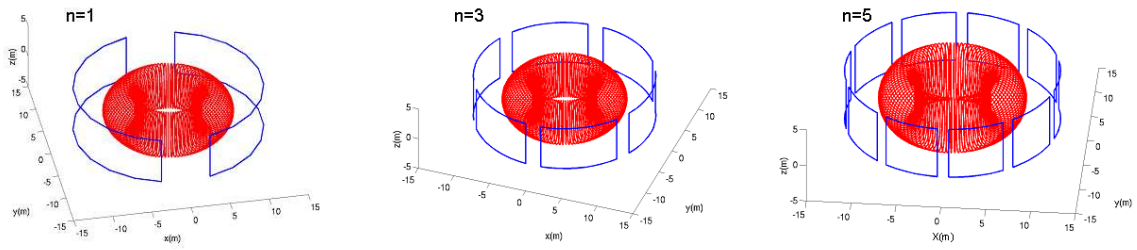

Figure 5.2: Three of the five coils designs used for the comparison of different n possibilities.

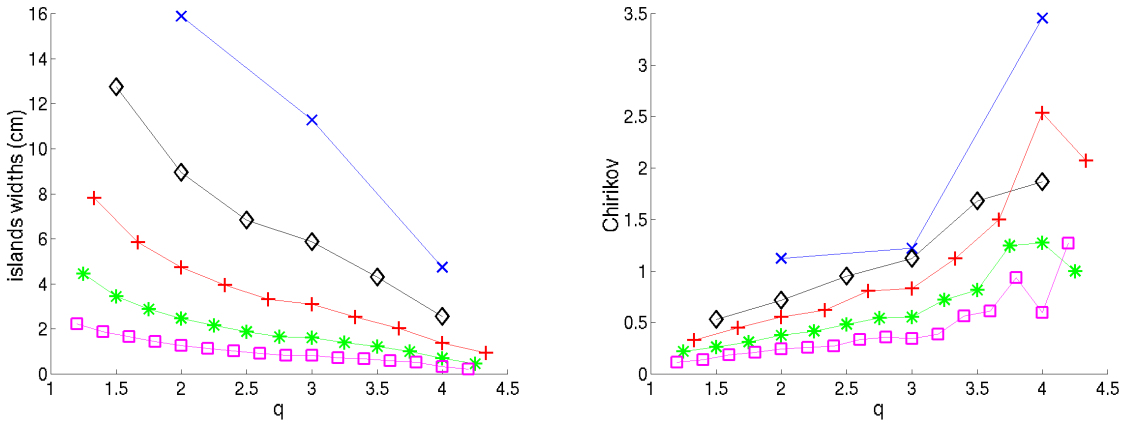

Figure 5.3: Islands widths and Chirikov parameter profiles for the compared designs (q is used as a radial coordinate). Blue x's: $n = 1$; black diamonds: $n = 2$; red +'s: $n = 3$; green stars: $n = 4$; magenta squares: $n = 5$.

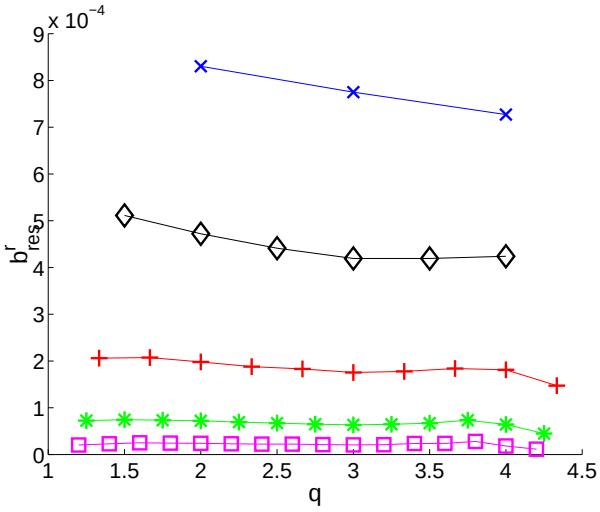

Figure 5.4: Profile of b^r_{res} (dimensionless quantity) for the compared designs (q is used as a radial coordinate). Blue x's: $n = 1$; black diamonds: $n = 2$; red +'s: $n = 3$; green stars: $n = 4$; magenta squares: $n = 5$.

As to the Chirikov parameter, we can notice that it is highest at the edge (and above 1) for lowest n designs. This was not obvious *a priori* since higher n's imply a higher radial density of islands chains, which has a positive influence on the Chirikov parameter. We stress the fact that the large value of σ_{Chir} at $q = 4$ for the $n = 1$ design should be looked at with caution, since this value is very sensitive to the position of the $q = 4$ surface. In the results presented here, that surface is very close to the separatrix, which explains the large value of σ_{Chir}.

Looking for a compromise between the possibility to ergodize the magnetic field at the edge for a reasonable value of the current in the coils, which is easier for lower n's, and the avoidance of large core islands/RMPs, which requires to use large enough n's[5], it appears, judging from these results, that the $n = 3$ design is the best solution. It should also be noticed that $n = 3$ designs are likely to be compatible with the ITER design, which has a natural $n = 18$ symmetry (in particular, there are eighteen TF coils).

From the single preceding example, the statement that $n = 3$ is the best possibility whatever the poloidal structure of the coils could appear as too strong. However, as we will see in section 5.5, there is not much flexibility on the poloidal spectrum of the magnetic perturbations[6], so that the results of calculations similar to those exposed above for other poloidal structures of the coils would be quite similar.

Possibly, $n = 4$ would also appear satisfying for designs that produce large m RMPs, such as the coils wound around the blanket modules presented in section 5.5.3. Using $n = 4$ would furthermore be safer in terms of core perturbations. This can explain why the USBPO group is working on $n = 4$ concepts.

5.4.2 Multiple n's possibilities

The preceding section was focused on single n configurations. However, configurations with several non-negligible toroidal harmonics should also be considered. For instance, one can think of using a configuration producing both $n = 1$ and $n = 2$ RMPs (cf. fig. 5.5, concept (C)). As compared to configurations producing only $n = 1$ (concept (A)) or only $n = 2$ (concept (B)) perturbations, the islands widths, δ, can be reduced. Indeed, while the $n = 1$ (resp. $n = 2$) concept requires islands of half-widths (in terms of q, used here as a radial coordinate [cf. fig. 5.5]) $\delta \sim 1/2$ (resp. $\delta \sim 1/4$) in order to have islands overlapping, the mixt concept can reach the same objective with, for instance, integer q (resp. $q = m/2$) islands[7] of half-widths $\delta \sim 1/3$ (resp. $\delta \sim 1/6$), i.e. 3/2 times smaller. Since the islands widths are proportional to the square root of the RMPs, this means that the current in the coils can be multiplied by a factor $(2/3)^2 = 4/9$, so that some current can be saved. Core RMPs are also made smaller in that case. However, it is likely that they would still cause problems. Other combinations of different n's could be considered, but we do not see how any of these would be better than a "pure" $n = 3$ configuration.

[5]Recall also that the $m/n = 2/1$ and 3/2 NTMs are the most dangerous ones, which dissuades even more from using $n = 1$ or $n = 2$.

[6]In particular, core and edge RMPs are correlated, meaning that there does not exist any low n concept which is able to ergodize the edge without producing large core RMPs.

[7]which in that case would be a composite of $n = 1$ and $n = 2$ islands

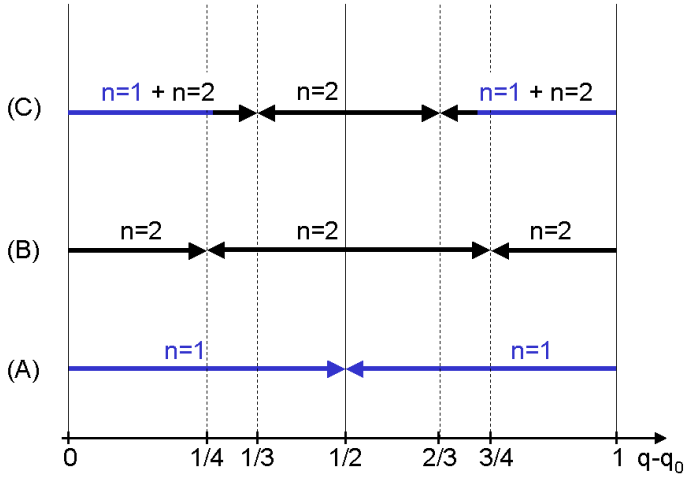

Figure 5.5: Conceptual sketch representing different possibilities for the spectrum in n of the coils configuration: (A) $n = 1$ only; (B) $n = 2$ only; (C) both $n = 1$ and $n = 2$. The arrows represent magnetic islands, $q - q_0$ (with q_0 an integer number, typically 3 or 4) being used as a radial coordinate.

5.5 Selection between different $n = 3$ possibilities

Now that we have determined that $n = 3$ designs offer the best compromise between ergodization of the magnetic field at the edge for a reasonable cost in terms of coils current and not too large core perturbations, we study different possibilities of $n = 3$ designs. We first present the three designs that have come out of the ERGITER project as the most promising ones and been discussed during the ITER design review. We then present other designs that were studied but rejected for different reasons.

5.5.1 Coils external to the vacuum vessel

This first design is based on coils that are external to the Vacuum Vessel (VV), i.e. quite far away from the plasma, see fig. 5.6. It consists of two rows of eighteen coils each, one above and one below the midplane, somewhat similarly to the DIII-D I-coils (although there are only six I-coils per row). For each row, the direction of the current in the coils alternates toroidally by groups of three coils so as to produce $n = 3$ perturbations. A poloidal cut of the normalized radial magnetic perturbation b^r (see section 3.2.2 for a definition) produced by these coils is shown in fig. 5.7.

The RMPs and Chirikov parameter profiles for 400kAt can be seen on fig. 5.8, demonstrating that 400kAt is a sufficient current in these coils in order to match the DIII-D reference case in terms of the Chirikov parameter profile ($\sigma_{Chir} \geq 1$ for $s \geq 0.95$ and $\sigma_{Chir}(s = 1) \simeq 3$).

The core perturbations correspond to an islands chain on the $q = 4/3$ surface of width $w_{4/3} = 2\delta_{4/3} \simeq 8$cm. We will see that this value is in the range of what is found with the other designs.

When doing a Poincaré plot with a color coding for the field line escape length,

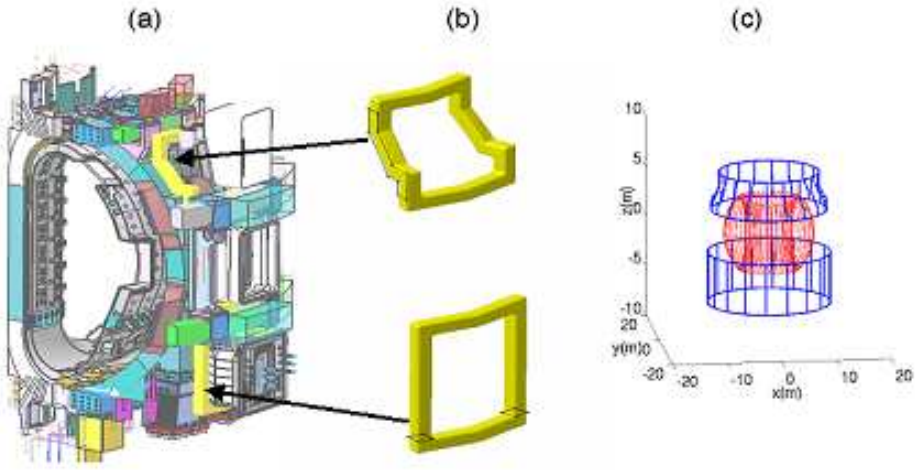

Figure 5.6: Design of a realistic concept with two rows of eighteen external coils, with implantation on the machine (left) and 3D view with zero-thickness wires, as used in the modelling (right).

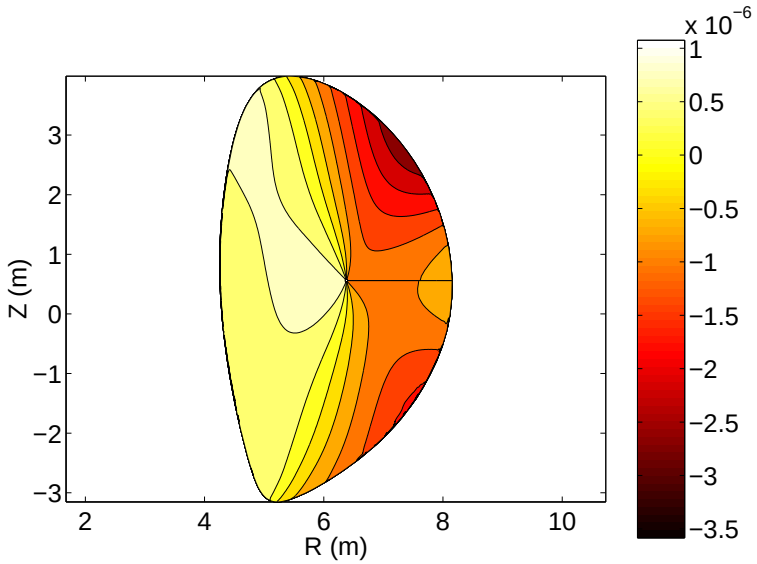

Figure 5.7: Poloidal cut of the normalized radial magnetic perturbation b^r produced by the two rows of eighteen external coils fed with 1kAt.

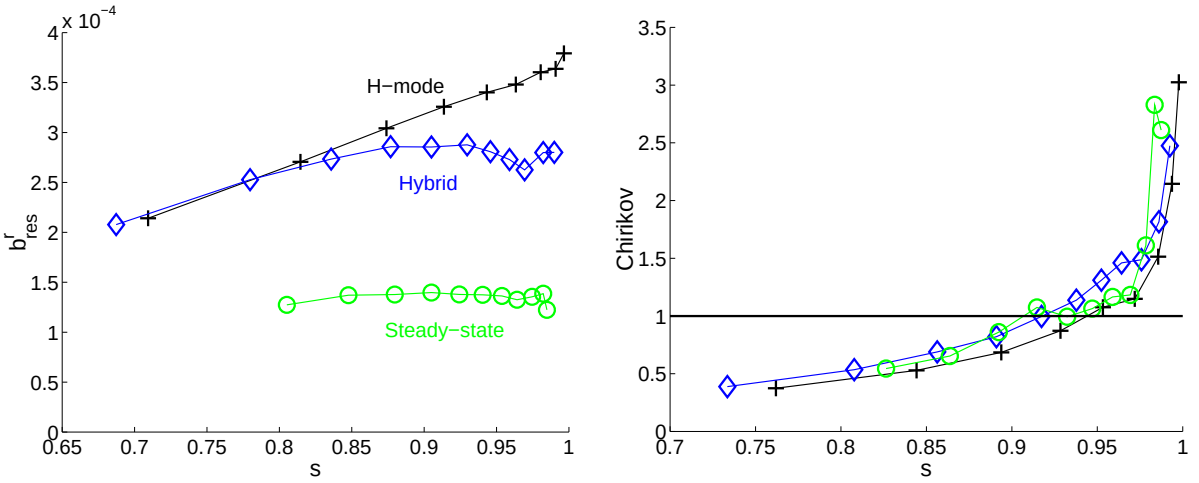

Figure 5.8: Crosses: profiles of b^r_{res} (left) and σ_{Chir} (right) for the design with two rows of eighteen external coils fed with 400kAt (diamonds [resp. circles] correspond to a hybrid-like [resp. steady-state-like] q profile, see section 5.6).

following the same rules as for fig. 3.8 in section 3.2.4, we find (cf. fig. 5.9) that the ergodic region extends towards the core up to $s \simeq 0.87$ for 400kAt, which is more than for the DIII-D reference case (where it was rather $s \simeq 0.9$). If we consider that the criterion for matching the DIII-D reference case is to ergodise the magnetic field up to $s \simeq 0.9$, this reduces the required current to 320kAt (see on fig. 5.10 the colored Poincaré plot for 320kAt).

Regarding non-resonant perturbations, it must be noticed that they are strong compared to other designs (see next sections). It can indeed be seen on fig. 5.11 that the magnetic perturbations spectrum is largely dominated by low m non-resonant harmonics[8].

5.5.2 Coils wound around the equatorial port plugs

A second possibility would be to wind the coils around the equatorial (midplane) port plugs of the machine (fig. 5.12), which presents the advantage to allow the coils to be much closer to the plasma. There will be eighteen equatorial port plugs in ITER, equally spaced toroidally, which will be used as points of access for heating systems (NBI, RF) as well as for different diagnostics and remote handling systems.

For first calculations, we assumed all of these port plugs to be available to wind coils around them, and we phased the coils by groups of three so as to produce $n = 3$ perturbations, similarly to the coils presented in the preceding section. In the calculations presented here we took a realistic design, with solenoid-like coils made of eleven windings that span a radial width of 0.5m. A poloidal cut of the normalized radial magnetic perturbation b^r produced by these coils is shown in fig. 5.13. We found that a current of 100kAt is sufficient to match the DIII-D reference case in terms of the Chirikov parameter

[8] In this manuscript, our estimation of the non-resonant magnetic perturbations is limited to a "visual" one obtained by looking at the RMPs spectra. A more quantitative treatment of the problem requires to apply the theory of neoclassical viscosity [76]. As this manuscript is being written down, these aspects are starting to be investigated by our ITER Design Review group.

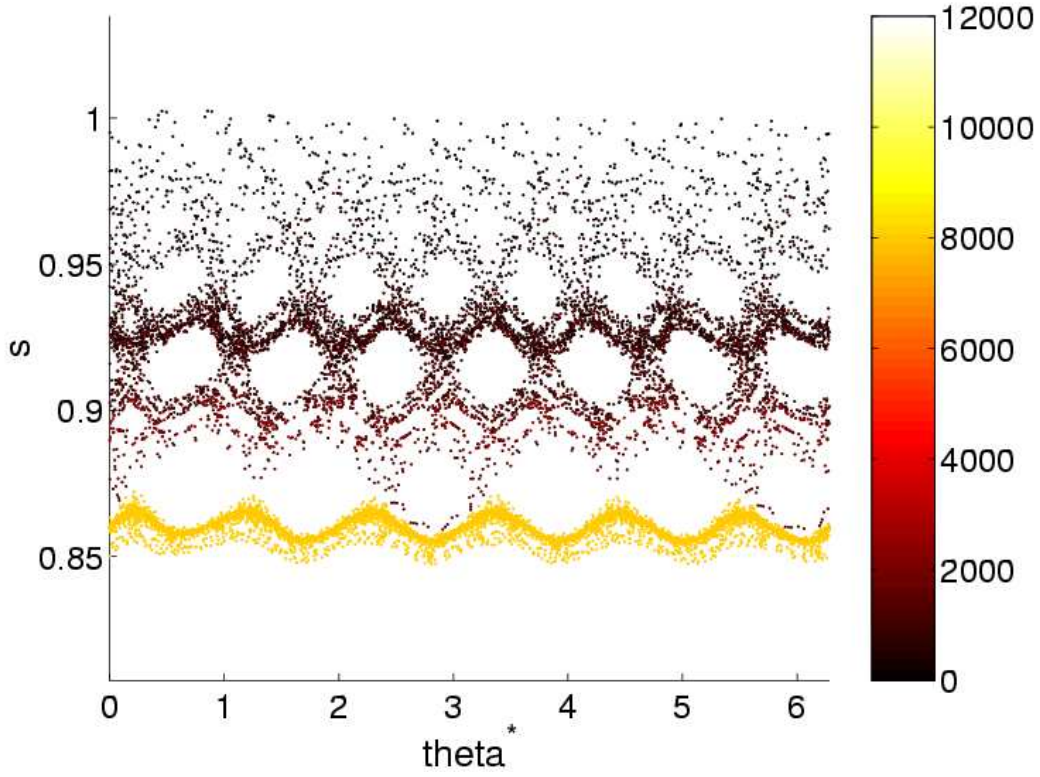

Figure 5.9: Poincaré plot with a color coding following the same rules as for fig. 3.8 in section 3.2.4, for the design with two rows of eighteen external coils each (with no toroidal phase shift between the rows) and for 400kAt in the coils.

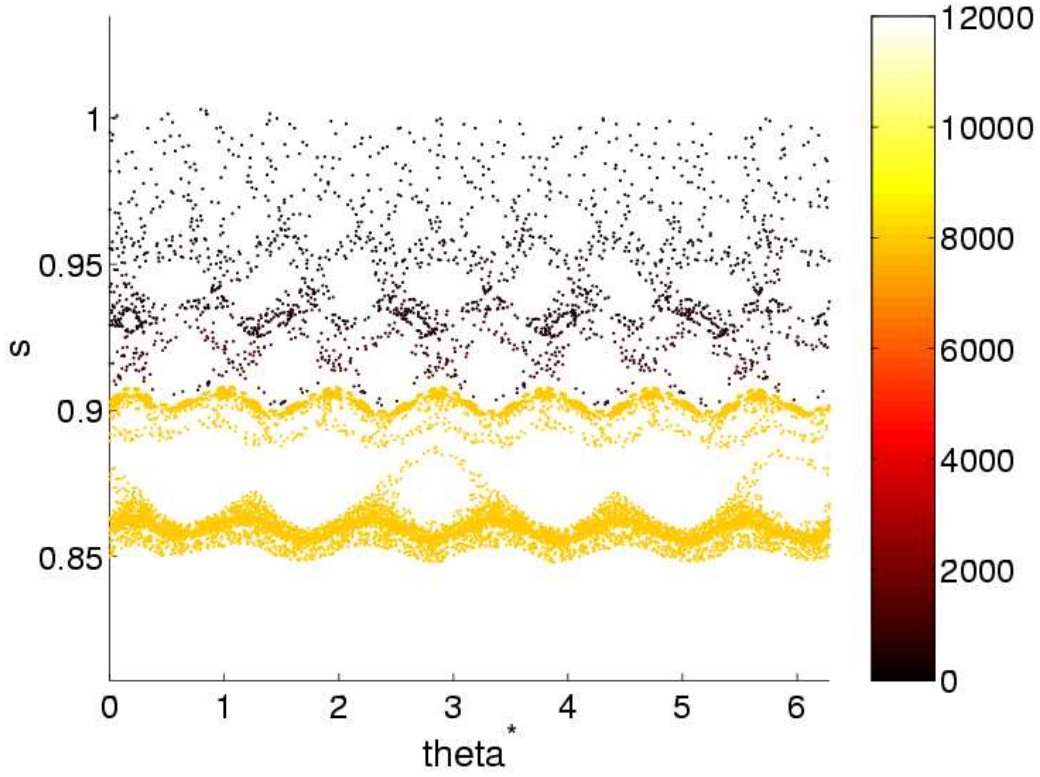

Figure 5.10: Same as fig. 5.9 but for 320kAt in the coils.

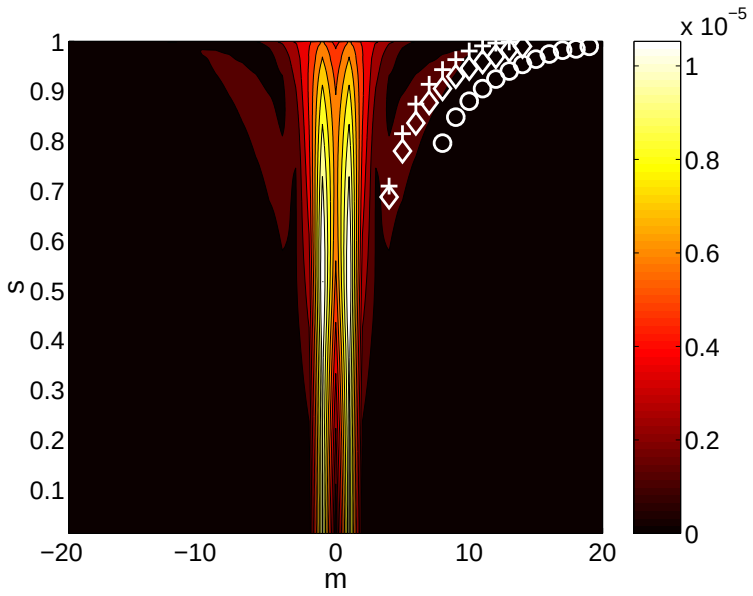

Figure 5.11: Spectrum of $2|\tilde{b}^1_{m,-3}|$ (dimensionless quantity) as a function of m and the radial coordinate s, for the design with two rows of eighteen external coils each (with no toroidal phase shift between the rows) fed with 1kAt, with crosses showing the position of the resonant harmonics, $\tilde{b}^1_{res}$ (diamonds [resp. circles] correspond to a hybrid-like [resp. steady-state-like] q profile, see section 5.6).

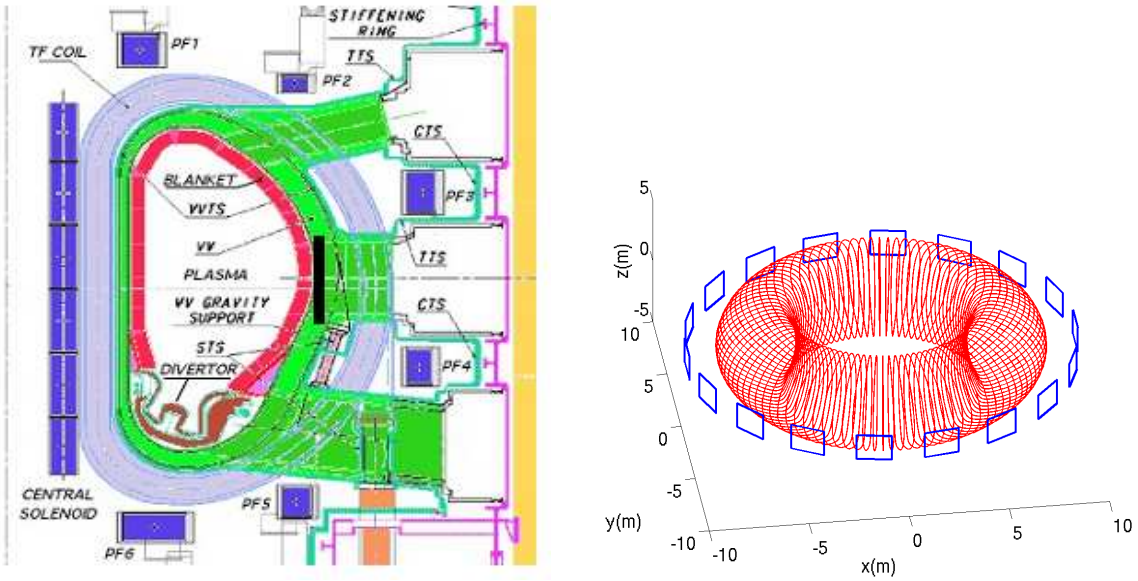

Figure 5.12: Design for the coils wound around the eighteen equatorial port plugs.

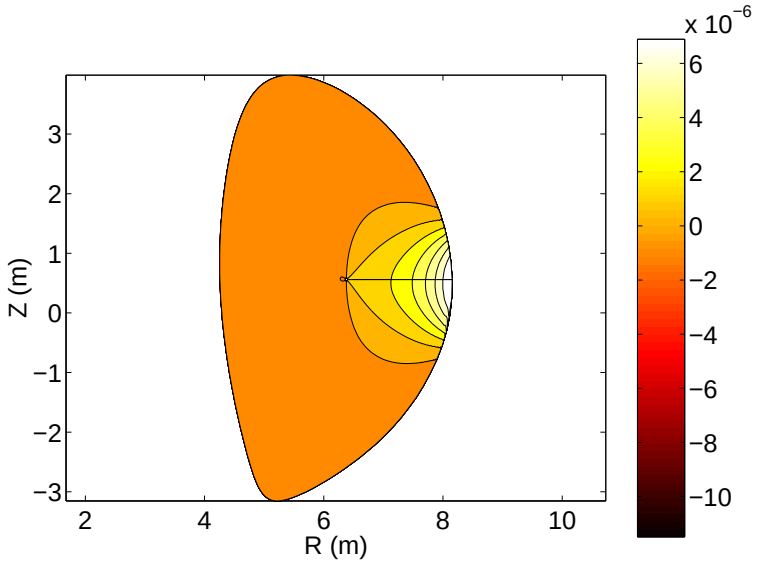

Figure 5.13: Poloidal cut of the normalized radial magnetic perturbation b^r produced by the coils wound around the eighteen equatorial port plugs fed with 1kAt.

profile, but, judging from Poincaré plots, as for the preceding section, 70kAt are in fact enough in order to ergodize the magnetic field up to $s \simeq 0.9$. Core perturbations are larger than for the coils presented in last section, but the difference is not huge: $b^r_{res}\,(q = 4/3) \simeq 3 \cdot 10^{-4}$ ($w_{4/3} \simeq 9.5$cm). This is the occasion to recall what was observed in section 3.3, i.e. that, due to the θ^* effect, the RMPs at $q = 4/3$ and at $q = 12/3$ are strongly correlated. We shoud not be surprised, thus, to find that all the designs have similar ratios of core to edge RMPs.

A crucial point is that in fact it is very unlikely that all of the eighteen midplane port plugs will be available to wind ELMs control coils around them. Indeed, ports 4 through 7 will be occupied by NBI systems and ports 13 through 15 by antennas for RF heating. Winding coils carrying ∼100kAt around such systems could perturb them strongly. Some of the eighteen coils would therefore have to be "sacrificed", with implications on the required current of the other coils, and the problem to still be able to create "clean" $n = 3$ RMPs (i.e. not to have too strong low n components which could perturb the core plasma and brake down the plasma toroidal rotation). In this respect, it can be interesting to consider the situation where only nine of the eighteen coils are available: ports 1 through 3, 7 through 9, and 13 through 15. Indeed, the ports to avoid, after discussion in particular with RF physicists, could be restrained to ports 4 through 6. In order to create clean $n = 3$ perturbations, we feed all the coils with the same current in the same direction. We then find that 200kAt are required to match the Chirikov parameter profile from DIII-D (see fig. 5.14) and ∼120kAt to ergodize the magnetic field up to $s \simeq 0.9$ (see fig. 5.15). Non-resonant perturbations are much smaller than for the design presented in last section, as can be seen on fig. 5.16. Studies relative to this concept have to be continued in order to reach a realistic design. It is likely that, in any case, the RMPs spectrum will not contain only $n = 3$ harmonics, but also lower n harmonics. Then, it should be determined if a compensation of these harmonics by the PF coils or EFCCs would be possible or not.

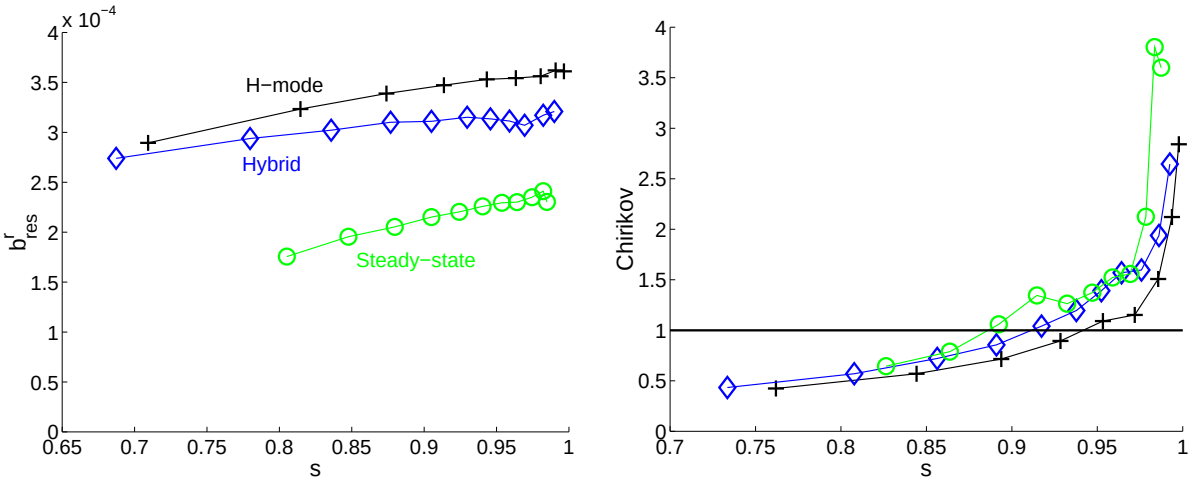

Figure 5.14: Crosses: profiles of b^r_{res} (left) and σ_{Chir} (right) for the nine coils wound around the midplane port plugs, for 200kAt (diamonds [resp. circles] correspond to a hybrid-like [resp. steady-state-like] q profile, see section 5.6).

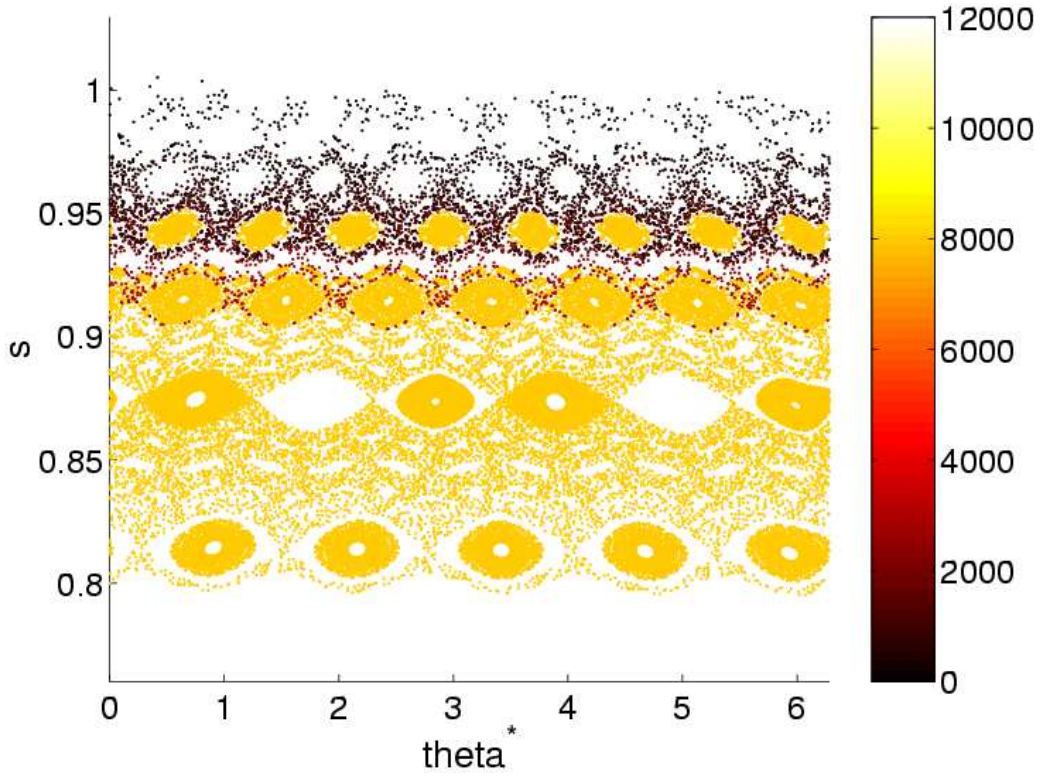

Figure 5.15: Poincaré plot with a color coding following the same rules as for fig. 3.8 in section 3.2.4, for the nine coils wound around the midplane port plugs fed with 120kAt.

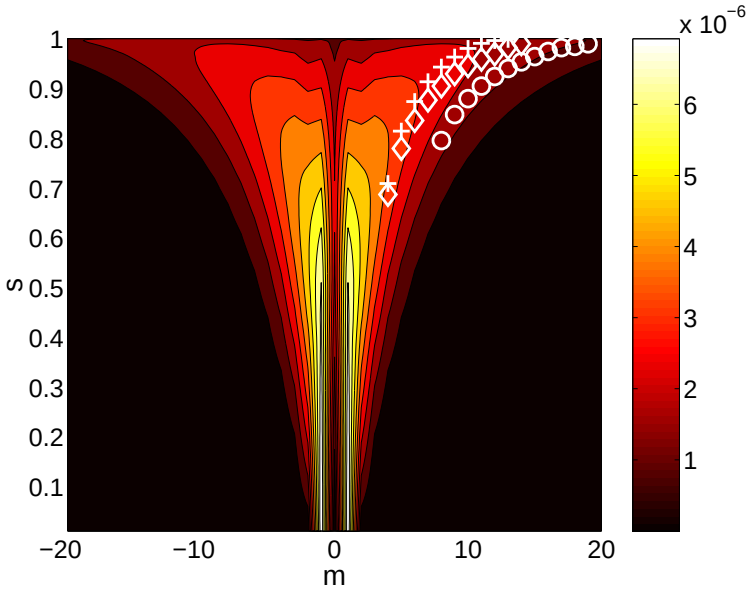

Figure 5.16: Spectrum of $2|\tilde{b}^1_{m,-3}|$ (dimensionless quantity) as a function of m and the radial coordinate s, for the nine coils wound around the midplane port plugs, all fed with 1kAt, with crosses showing the position of the resonant harmonics, $\tilde{b}^1_{res}$ (diamonds [resp. circles] correspond to a hybrid-like [resp. steady-state-like] q profile, see section 5.6).

5.5.3 Coils wound around the blanket modules

Yet another possibility would be to wind the coils around the blanket modules of the machine. This is the option in which coils are closest to the plasma. ITER is equipped with a blanket facing the plasma, whose role is primarily to shield external components from the fusion neutrons coming from the plasma. This blanket is made of several rows, each of these rows being itself constituted of thirty-six modules[9], each module spanning a $\triangle\varphi$ of 10° [79]. The concept we present here uses four of these rows (see fig. 5.17), with one coil wound around each blanket module and coils phased by groups of five toroidally (one coil out of six being left with no current in it) in order to produce $n = 3$ perturbations. A poloidal cut of the normalized radial magnetic perturbation b^r produced by these coils, in the configuration where all four rows are in phase toroidally, the so-called "0/0/0/0" configuration (where each number represents the toroidal phase shift of a row, from top to bottom), is shown in fig. 5.18.

Using the 0/0/0/0 configuration, the reference Chirikov parameter profile can be matched with a current of 28kAt (see fig. 5.19) and edge ergodization up to $s \simeq 0.9$ be reached with 22kAt (see fig. 5.21). The 4/3 islands widths for 28kAt is $w_{4/3} \simeq 7.5$cm. As to the non-resonant perturbations, the blanket coils design offers good performances compared to the two designs described in the preceding sections, as can be seen on fig. 5.20. This phasing is however not optimized and about 40% of the current could be saved by using the optimal phasing, which is given by a toroidal shift by $\Delta\varphi_{shift} = -\pi/6$, i.e. -3 blanket modules for row 2 (second row from the top, cf. fig. 5.17) and by $\Delta\varphi_{shift} = \pi/6$, i.e. +3 blanket modules for row 3. We call this configuration the 0/-3/+3/0 or "optimized phasing" configuration. It can be seen on fig. 5.22 (bottom plot) that 17kAt are enough

[9]except for rows that pass in front of ports since there are no blanket modules in front of the ports

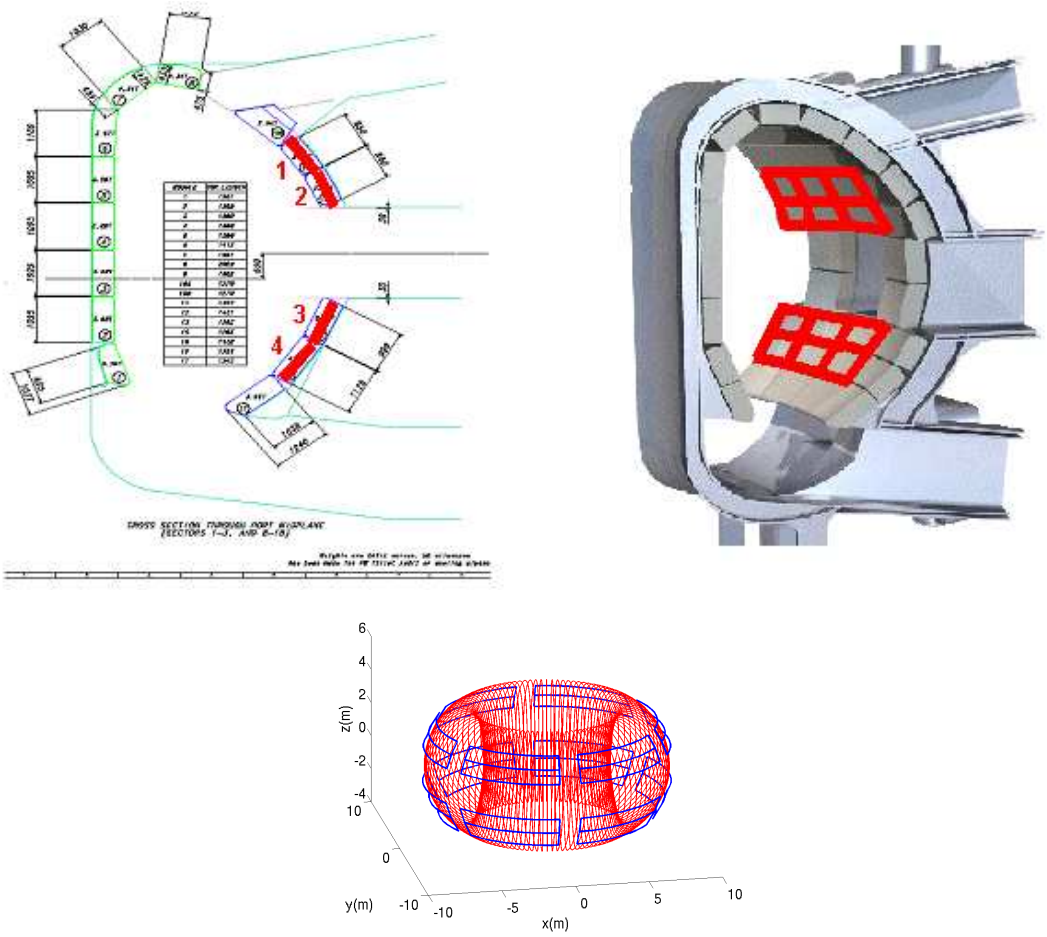

Figure 5.17: Design of the coils wound around the blanket modules.

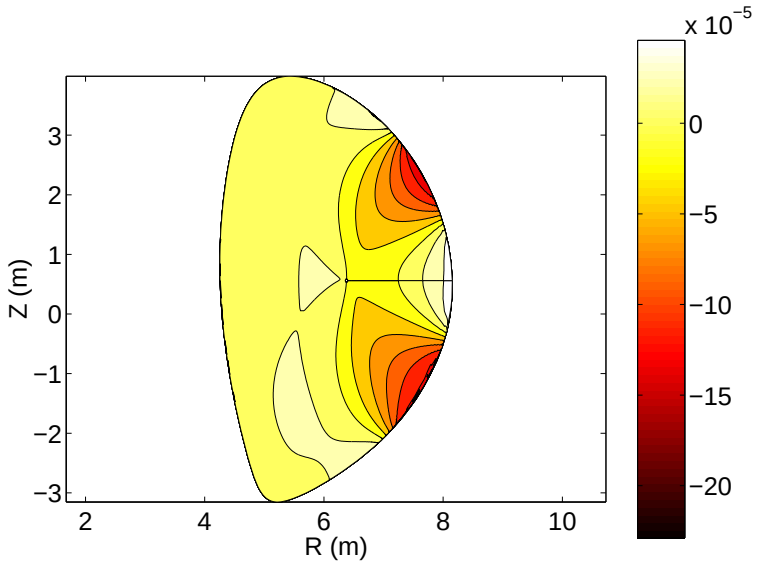

Figure 5.18: Poloidal cut of the normalized radial magnetic perturbation b^r produced by the coils wound around the blanket modules, in 0/0/0/0 configuration, fed with 1kAt.

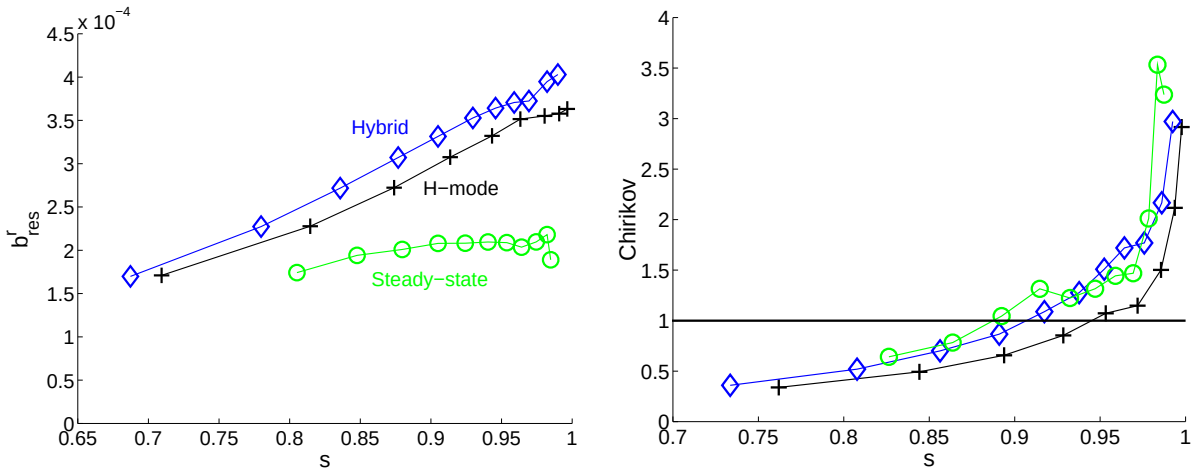

Figure 5.19: Crosses: profiles of b^r_{res} (left) and σ_{Chir} (right) for the coils wound around the blanket modules in 0/0/0/0 configuration fed with 28kAt (diamonds [resp. circles] correspond to a hybrid-like [resp. steady-state-like] q profile, see section 5.6).

to obtain the same RMPs amplitude at the edge ($b^r_{res} \sim 3.7 \cdot 10^{-4}$) with this configuration than with 28kAt in the 0/0/0/0 configuration. Looking at the spectrum of the magnetic perturbations (fig. 5.22, top plot), we can see that the resonant ridge has been displaced so as to be aligned with the set of resonant points shown by the crosses. It is also clear from the spectrum that the non-resonant perturbations are smaller in this configuration than in the 0/0/0/0 one.

Although it is not the scope to detail engineering concerns here, it should be said that, while very attractive in terms of physics and required current, these coils pose serious technical problems, because they will be subject to a high neutron flux, to large forces during disruptions and it would be almost impossible to access to them for maintenance or replacement of certain coils. Furthermore, these coils require a redesign of the blanket which represents an important engineering cost.

Finally, it should be mentioned that USBPO has studied very similar designs but with the coils located just behind the blanket, i.e. in-between the blanket and the first wall of the VV or in-between the VV walls[10], and in $n = 4$ configuration. These concepts have performances close to those of the concept presented above, and may be easier to realize from a technical point of view.

5.5.4 Other designs

Error Field Correction Coils

ITER will be equipped with three sets of six Error Field Correction Coils (EFCCs) each (see fig. 5.23): “top”, “side” and “bottom” EFCCs [73]. Since, for each set of EFCCs, there are six coils equally spaced in the toroidal direction, it is possible to produce $n = 3$ perturbations with the EFCCs. It is thus obviously worthwile investigating if these coils have the ability to control the ELMs.

Our calculations showed that edge ergodization could be reached using the side (resp. top, resp. bottom) EFCCs in $n = 3$ configuration using 400kAt (resp. 4.3MAt, resp.

[10]The VV is indeed constituted of two walls

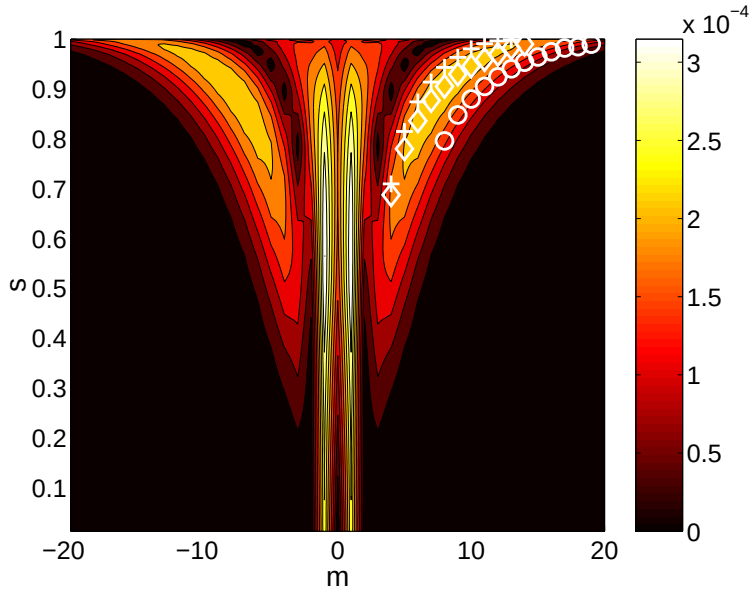

Figure 5.20: Spectrum of $2|\tilde{b}^1_{m,-3}|$ (dimensionless quantity) as a function of m and the radial coordinate s, for the coils wound around the blanket modules (with no toroidal phase shift between the rows) fed with 1kAt, with crosses showing the position of the resonant harmonics, $\tilde{b}^1_{res}$ (diamonds [resp. circles] correspond to a hybrid-like [resp. steady-state-like] q profile, see section 5.6).

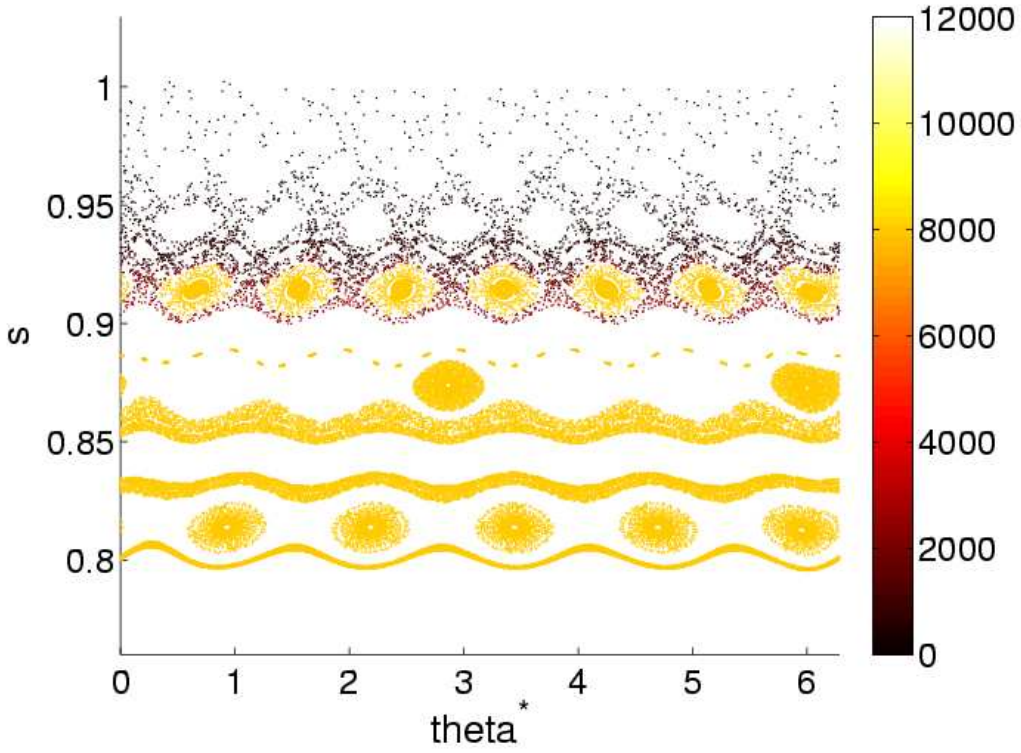

Figure 5.21: Poincaré plot with a color coding following the same rules as for fig. 3.8 in section 3.2.4, for the coils wound around the blanket modules (with no toroidal phase shift between the rows) fed with 22kAt.

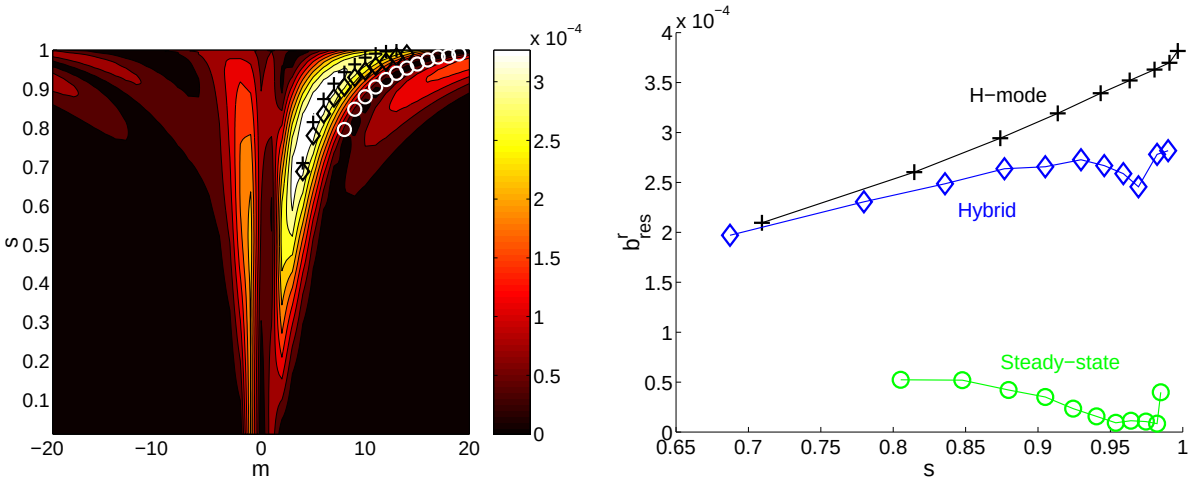

Figure 5.22: Top: same as fig. 5.20 but for the "optimized phasing" (0/-3/+3/0) configuration. Bottom: corresponding profile of b^r_{res} for 21kAt in the coils (diamonds [resp. circles] correspond to a hybrid-like [resp. steady-state-like] q profile, see section 5.6).

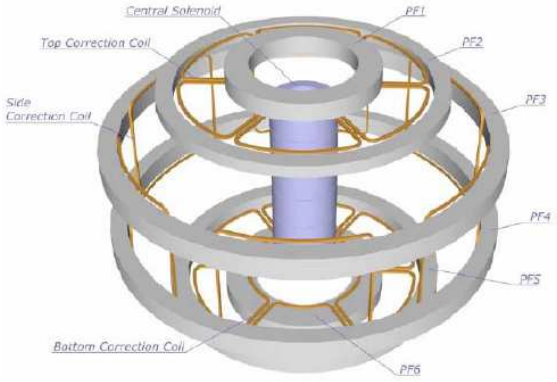

Figure 5.23: Sketch of the ITER PF coils (in gray) together with the EFCCs (in brown). From [73].

7.6MAt). The fact that the currents required in the top and bottom coils are much larger than the ones required in the other coils is an illustration of what was said in section 3.3, i.e. that, in order to benefit from the θ^* effect, one should produce magnetic perturbations localized on the LFS. The EFCCs were designed for current capabilities of 140kAt (10kA times 14 turns) for the top ones, 280kAt (10kA times 28 turns) for the side ones and 180kAt (10kA times 18 turns) for the bottom ones. Thus, there is only a factor $\sim$1.4 between the nominal side EFCCs current and the current required for edge ergodization, which suggests the idea of upgrading the current capabilities of these coils.

It can be noticed, however, that the core perturbations from these coils are quite large ($b^r_{res}(q = 4/3) \simeq 4 \cdot 10^{-4}$, corresponding to islands widths $w_{4/3} \simeq 11$cm) and also that the non-resonant magnetic perturbations are very large, which led our ITER Design Review group to reject the idea of using the EFCCs for ELMs control.

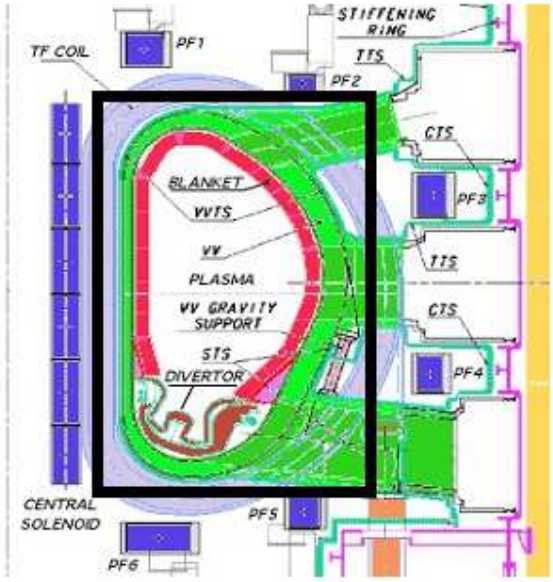

Figure 5.24: Approximate TF coils design (in black) used for the calculations presented here (to compare with the actual TF coils, appearing here in light blue).

"Ripple coils": modulations of the current between the different toroidal field coils

Just as for the EFCCs, it is worthwhile investigating what can be done from other already existing coils: the TF coils. Here, we approximated the TF coils by rectangles, as can be seen on fig. 5.24.

It is interesting, first, to calculate the RMPs produced by the TF coils in their standard configuration, i.e. all fed with 10MAt. Due to the fact that there are eighteen TF coils equally spaced in the toroidal direction, the TF coils indeed produce, in addition to the main axisymmetric toroidal field of 5.2T at $R = 6.2$m, a small $n = 18$ field with a radial component. These $n = 18$ perturbations to the axisymmetric field comprise radial RMPs which decrease very fast when going towards the plasma centre (see fig. 5.25 [upper left plot]) and produce very small vacuum islands (typical width ~ 3mm) at the edge (fig. 5.25 [upper right plot]) which can however overlap due to the even smaller distance between them, resulting in a Chirikov parameter above 1 at the very edge, i.e. at $s \simeq 0.98$ (fig. 5.25 [lower plot]). Since it seems that ELMs suppression requires a much wider ergodic layer, we can say that these $n = 18$ perturbations from the TF coils should, by far, not allow to supress the ELMs. However, it is instructive to know that TF coils in their standard configuration produce a rather strong ergodization of the magnetic field for $s \geq 0.98$ (if the vacuum field approximation holds).

Now, we can also study the possibility of producing RMPs by intentionally modulating the current in the TF coils. Here, we show results obtained by modulating the current in one out of three TF coils, alternating positive and negative modulations, thus producing principally $n = 3$ perturbations. On fig. 5.26 (right), one can see that for a modulation of 800kAt (i.e. 8% of the nominal TF coils current), the DIII-D reference Chirikov parameter profile can be matched. Core perturbations (see fig. 5.26 [left]) are slightly larger than

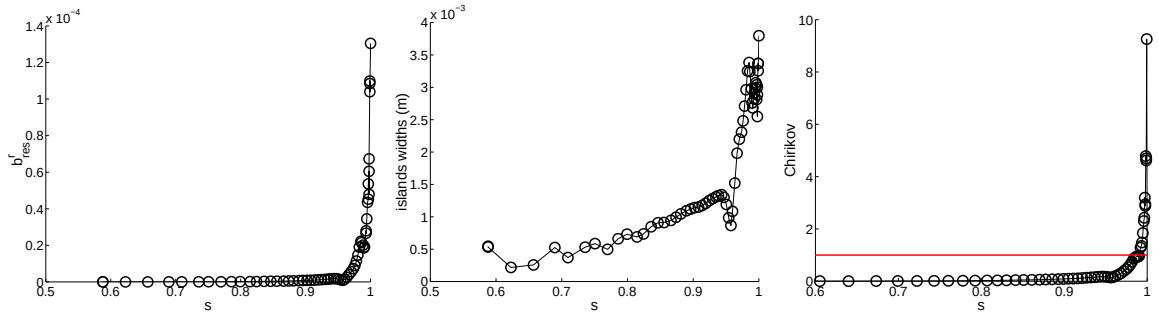

Figure 5.25: All plots for 10MAt in the eighteen TF coils. Upper left: profile of the radial-like $n = 18$ RMPs. Upper right: profile of the $n = 18$ islands widths. Lower: profile of the Chirikov parameter.

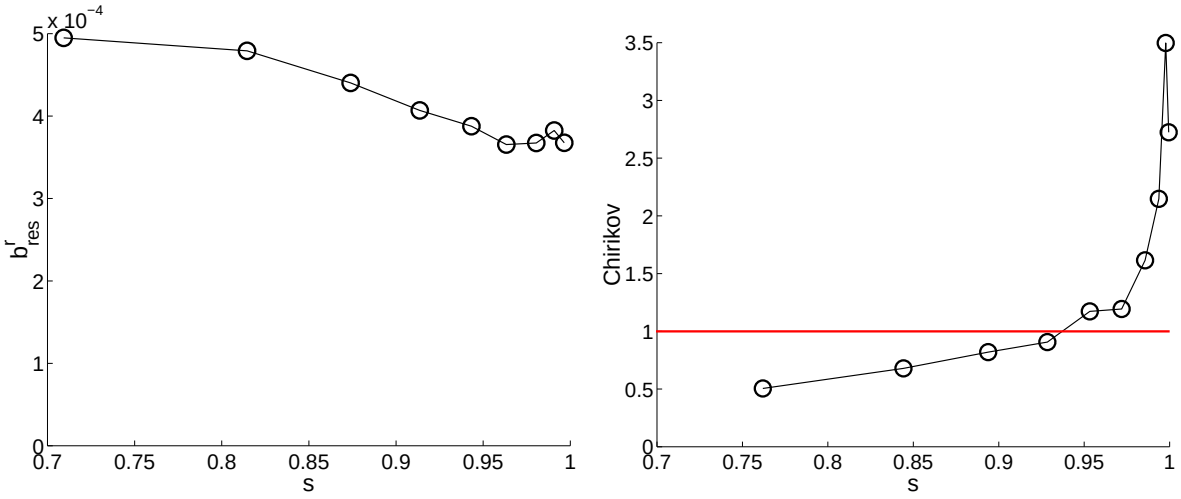

Figure 5.26: All plots for modulation of 800kAt in one out of three TF coils, alternating positive and negative modulations. Left: profile of the $n = 3$ radial-like RMPs. Right: profile of the Chirikov parameter.

for other designs studied above. Non resonant perturbations are also very large. But the main problem could reside in the fact that the ripple produced by these coils is of the order of 1%, whereas other designs are closer to 0.3%, as can be seen on fig. 5.27.

Further designs

Further considered but rejected designs are shown on fig. 5.28 and presented in the ERGITER reports, in particular in [67]. The results of our calculations for these designs appear in the recapitulative table in section 5.7. Here, we only present these designs very briefly:

- Designs (1) (cf. fig. 5.28) and (2) are older versions of the design presented in section 5.5.1 (and they have less good performances).
- Design (3) is the model we took for the side EFCCs, already presented above.
- Design (4) used coils fixed on the inner side of the TF coils. This design requires very large currents in the coils (nearly 1MAt) because of their small area.

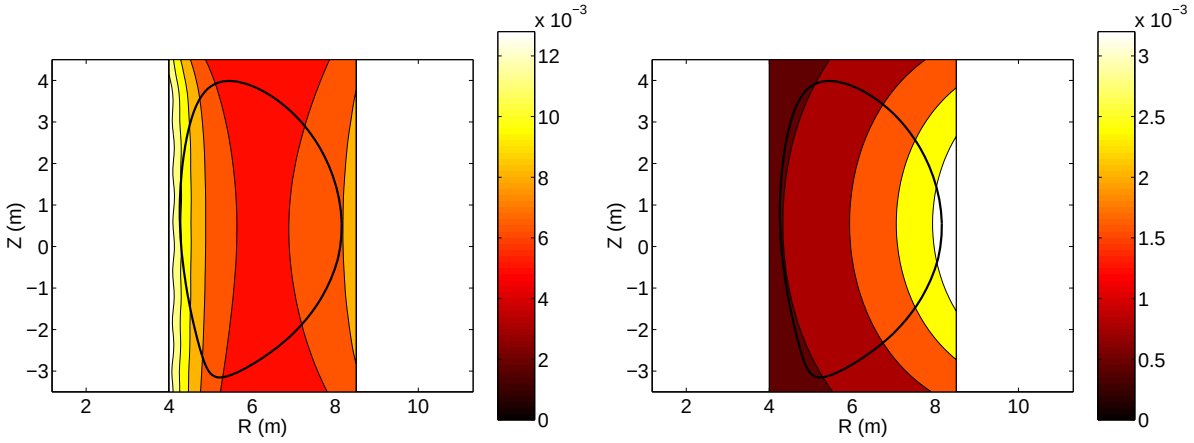

Figure 5.27: Amplitude of the $n = 3$ harmonic of the TF normalized to the local axisymmetric TF, for the design using a modulation of the current in one out of three TF coils (left) and for the side EFCCs-like design (right), both fed with the current corresponding to a matching of the reference case, i.e. 800kAt and 400kAt, repectively.

- Finally, design (5) intended to exploit the apparently unoccupied space in between the VV and the TF coils but the required current was too large.

5.6 Sensitivity to changes in scenario and plasma parameters (q profile, β_p, l_i)

All of the calculations shown above were done for a standard H-mode with $q_{95} \simeq 3$. However, as stated in section 5.2, one of or goals is to propose a design that is also adapted to the hybrid ($q_{95} \simeq 4$) and the steady-state ($q_{95} \simeq 5$) scenarios and that is robust to variations in equilibrium parameters such as the poloidal beta β_p and the internal inductance l_i (which are defined in section 5.6.4).

5.6.1 Effect of changing the q profile only

In this section, we study the effect of changing the q profile only, keeping the equilibrium coordinates system unchanged (i.e. keeping the equilibrium coordinates system from the standard H-mode). It should be noticed that we loose consistency in the equilibrium proceeding this way. Nevertheless, this method is convenient because it allows to calculate the magnetic perturbations spectrum only once for each design, changes in the RMPs profiles coming only from changes in the positions of the resonant harmonics. In next section, we will compare the results given by this method to the more rigorous approach, which consists in recalculating a self-consistent equilibrium when changing the q profile.

The position of the resonant harmonics for q profiles typical of a hybrid scenario and of a steady-state scenario appear in the magnetic perturbations spectra shown above (figs. 5.11, 5.16 and 5.20, for the two rows of eighteen external coils, the nine coils wound around the midplane ports and the blanket coils in 0/0/0/0 configuration, respectively). Generally speaking, a degradation of the amplitude of the RMPs can be observed with increasing q_{95} (there is only one exception: for the blanket coils, the hybrid-like q profile

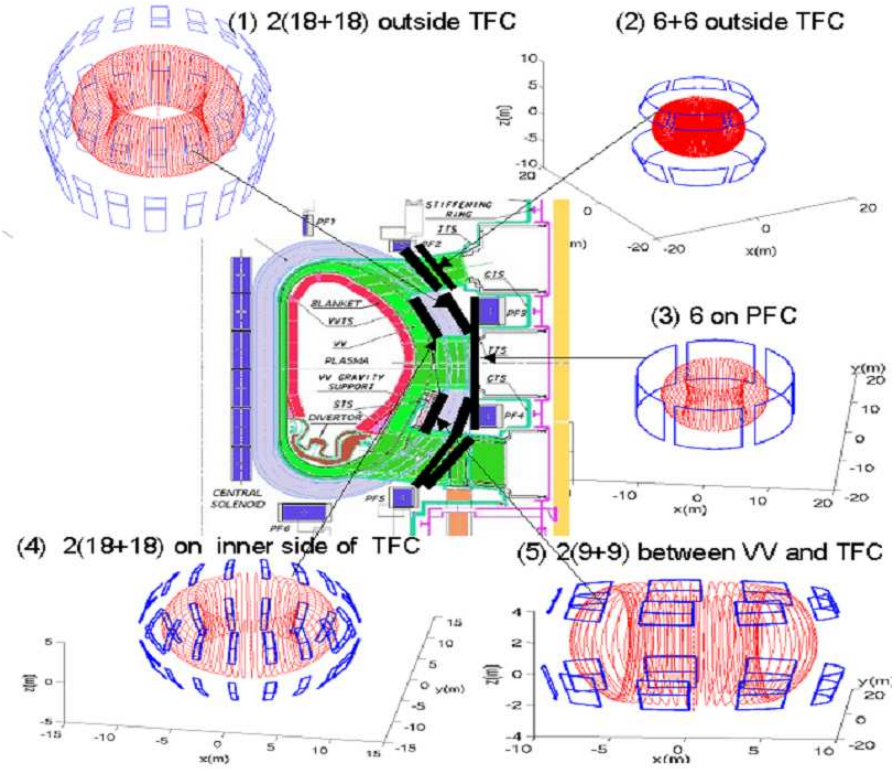

Figure 5.28: Several considered and rejected designs.

has slightly larger RMPs than the H-mode q profile). This can be observed clearly on the b^r_{res} profiles from figs. 5.8, 5.14 and 5.19 (left plots). However, in terms of Chirikov parameter, this is compensated by the larger magnetic shear at the edge associated to larger q_{95}: we can see indeed on figs. 5.8, 5.14 and 5.19 (right plots) that the Chirikov parameter profiles are not degraded (and are even slightly raised) for the hybrid-like or the steady-state-like q profiles. Hence, edge ergodization should be possible for all three ITER reference scenarios for the values of the current in the coils given above.

5.6.2 Calculations for the hybrid scenario

We now compare the preceding method to the rigorous approach which consists in re-calculating a consistent equilibrium (based on an ASTRA simulation) for each ITER scenario. The comparison shown here is for the hybrid scenario and for the design with two rows of eighteen external coils. The two b^r_{res} profiles given by the two methods are shown in fig. 5.29. It appears that differences exist but remain in a reasonable range ($\sim$10% or less), which gives credibility to the approach used in last section.

5.6.3 Adaptability of the blanket coils

It is important to notice that the fact that RMPs are smaller for the hybrid and steady-state scenarios, even if it does not prevent from ergodizing the edge (in the vacuum approximation) thanks to the higher magnetic shear, could be a problem regarding RMPs penetration. Indeed, theory and experiments show that in order to penetrate into the

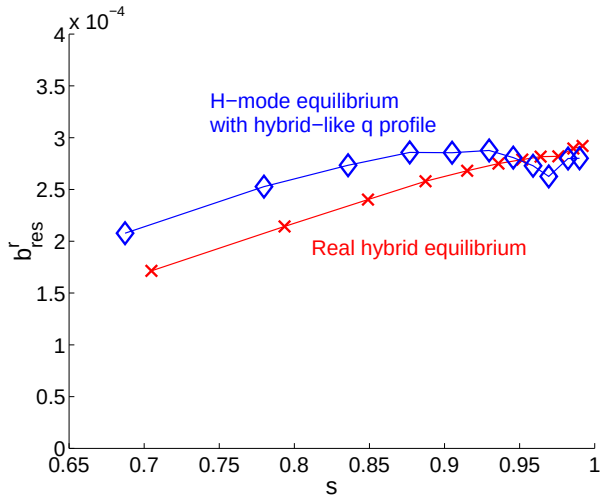

Figure 5.29: Comparison of calculations done with the H-mode equilibrium using a hybrid-like q profile (diamonds) and calculations with a real, self-consistent, hybrid equilibrium (crosses). Profiles of b^r_{res} for the design from section 5.5.1 fed with 400kAt.

plasma, RMPs need to have their amplitude larger than a certain threshold (cf. chapter 6). However, this threshold is not known at present (it is one of the main objectives of chapter 6 to address this question).

In this respect, the blanket coils (i.e. the coils wound around the blanket modules) present an interesting feature: the possibility to adapt to different values of q_{95}. The possibility of phase optimization was already shown in section 5.5.3 for the H-mode. On fig. 5.30, we now present results obtained for a configuration optimized for $q_{95} \simeq 5$, i.e. for the steady-state scenaio. This configuration is the -3/5/6/0 one (toroidal shift by -3 blanket modules for the top row, by +5 for the second row, etc.). We can see on the right plot that 20kAt are enough in order to reach b^r_{res} values at the edge of $\sim 3.7 \cdot 10^{-4}$, i.e. the typical values for the H-mode obtained with 28kAt in the 0/0/0/0 configuration or 17kAt in the 0/-3/3/0 (the optimized one), which demonstrates the adaptability of these coils.

In comparison, the coils wound around the midplane port plugs do not offer any possibility of adaptation (since they are monopole coils), while the two rows of eighteen external coils, even if they offer some adaptability, are far from being as performing as the blanket coils. This can be understood when looking at fig. 5.31, which presents the radial magnetic perturbations on the $s = 0.95$ surface as a function of φ and θ^*, together with a $q = 5$ field line, for the external coils and for the blanket coils (with optimized phasing for $q_{95} = 5$). It indeed appears on this figure that the zones of positive and negative radial magnetic perturbations produced by the external coils have a too large extension in θ^* to allow for a good adaptability to $q_{95} = 5$, whatever the relative phasing of the upper and lower coils, whereas the blanket coils are perfectly adapted.

5.6.4 Sensitivity to changes in β_p and l_i

The goal is now to address the question of what happens if the equilibrium is different from the reference ASTRA equilibrium taken in the above calculations, which will necessarily occur in reality. Two parameters in particular are susceptible to vary: the poloidal beta,

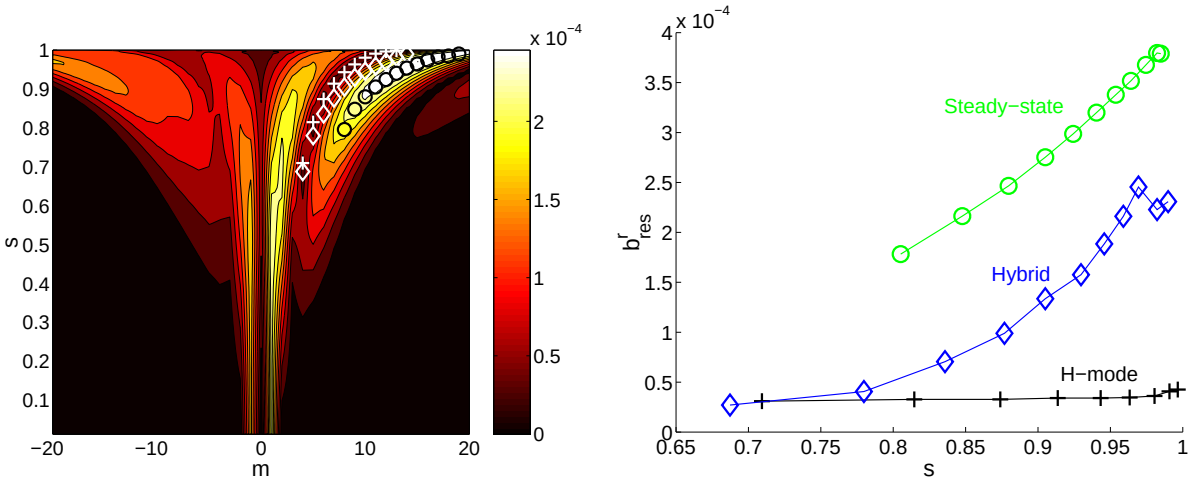

Figure 5.30: Left: spectrum of $2|\tilde{b}^1_{m,-3}|$ (dimensionless quantity) for the blanket coils with an optimized phasing for $q_{95} = 5$, with symbols showing the resonance (white +'s for the H-mode, blue diamonds for the hybrid-like q profile and green circles for the steady-state-like q profile). Right: corresponding profile of b^r_{res} for 20kAt in the coils (diamonds [resp. circles] correspond to a hybrid-like [resp. steady-state-like] q profile, see section 5.6).

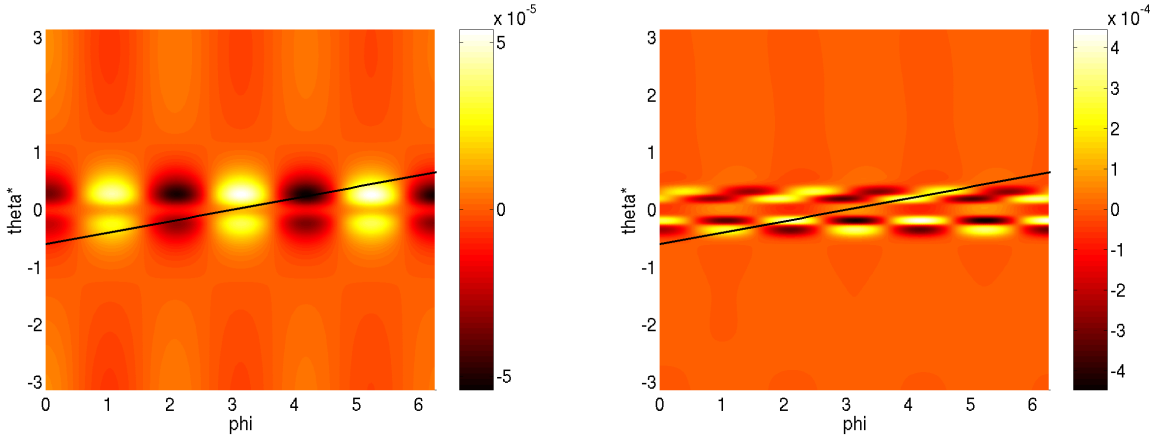

Figure 5.31: Colour plots of the normalized radial magnetic perturbations b^r on the $s = 0.95$ surface as a function of φ and θ^*, together with a $q = 5$ field line, produced by the two rows of eighteen external coils (left) and the blanket coils with optimized phasing for $q_{95} = 5$ (right), for 1kAt.

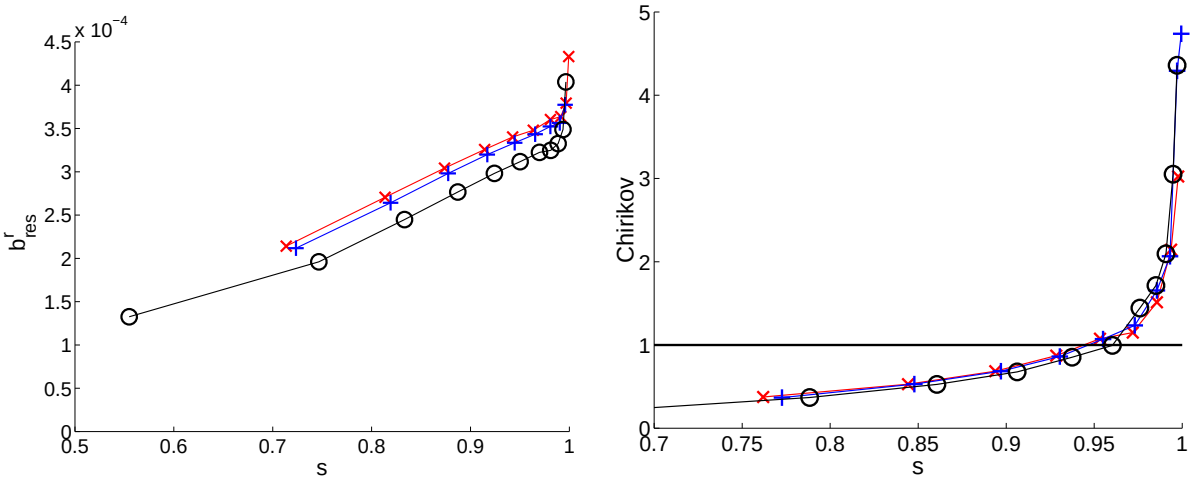

Figure 5.32: Profiles of b^r_{res} (left) and σ_{Chir} (right) for the two rows of eighteen external coils fed with 400kAt, with variations in β_p and l_i: red x's for $\beta_p \simeq 0.64$ and $l_i \simeq 0.8$, black circles for $\beta_p \simeq 0.6$ and $l_i \simeq 1$, and blue +'s for $\beta_p \simeq 1.2$ and $l_i \simeq 0.8$.

β_p, and the internal inductance, l_i. The poloidal beta [2] is defined as:

$$\beta_p \equiv \frac{8\pi a}{R_0 I^2} \iint_{PCS} p dS, \tag{5.2}$$

where a is the minor radius of the machine, R_0 its major radius, I the plasma current, p the plasma pressure, and where the integral is taken on a poloidal cross section (in the area limited by the separatrix). It gives a measure of the ratio of the kinetic energy accumulated in the plasma to the magnetic energy of the poloidal magnetic field. The internal inductance [2] is defined as:

$$l_i \equiv \frac{2}{(\mu_0 I)^2 \langle R \rangle} \iiint_{plasma} {B_p}^2 dV, \tag{5.3}$$

where μ_0 is the magnetic permeability of vacuum, $\langle R \rangle$ is the plasma volume divided by the plasma cross section area, B_p is the poloidal magnetic field, and the integral is taken over the confined volume of plasma (i.e. the volume inside the separatrix). Fig. 5.32 presents the results obtained for the design with two rows of eighteen external coils, for three different values of (β_p, l_i): $(0.64, 0.8)$, $(0.6, 1)$ and $(1.2, 0.8)$, which are in the range of typical possible variations for ITER. The variations in b^r_{res} and σ_{Chir} with (β_p, l_i) appear to be small, which shows the robustness of this design, and this result can in fact be generalized to all designs.

Variations in (β_p, l_i) should therefore not be a problem with respect to ELMs control by RMPs in ITER.

5.7 Synthesis

In this chapter, we have presented our design studies for ELMs control coils for ITER. This work was done in international collaboration, in particular with EFDA and ITER physicists and engineers, first under the ERGITER EFDA-CEA contract and later in the

process of the ITER Design Review. Designing an ELMs control system is a high priority task of the ITER Design Review to which this work contributed significantly.

The study is based on vacuum calculations with the ERGOS suite of codes presented in chapter 3. We took a DIII-D case with the I-coils in even parity configuration fed with 4kAt, also presented in chapter 3, as a reference in terms of Chirikov parameter profile / width of the ergodized layer. Our goal was to match the reference case for the three ITER reference scenarios (standard H-mode, hybrid and steady-state scenarios) with robustness with respect to the poloidal beta β_p and internal inductance l_i. Our constraints were the technical feasibility of the coils system, for which a low required current is always an advantage, as well as the avoidance of large core RMPs and Non-Resonant Perturbations (NRPs), which could trigger nefast core MHD modes and/or brake the plasma toroidal rotation.

We started with studying which toroidal mode number n of the magnetic perturbations was best adapted. It appeared that the answer to this question results from a compromise between low required current (for which a low n is better) and avoidance of large core RMPs (for which a large n is better). Configurations producing $n = 3$ perturbations were thought to be the best compromise.

We then studied many possibilities of such configurations. These possibilites appear in table 5.7. The numbers given in this table for the required current and the widths of the islands on the $q = 4/3$ surface (which is an indicator of the level of core RMPs) correspond to calculations for a standard H-mode equilibrium (from an ASTRA simulation). When we give two values for the required current, the first one corresponds to the extension of the ergodic region up to $s = 0.9$ and the second one to $\sigma_{Chir}(s = 0.95) = 1$. Indeed, we do not know which of these two features (which are both present for our reference case) is required for ELMs suppression. As to NRPs, we only give a qualitative evaluation, - (resp. =, +) meaning large (resp. medium, small) NRPs, judging only by the magnetic perturbations spectrum. NTV theory is starting to be applied by our ITER Design Review collaborators to progress towards a quantitative evaluation. Three concepts were considered as the most interesting and proposed by us to our ITER Design Review group:

- two rows of eighteen external coils;
- nine coils wound around the midplane port plugs;
- four rows of thirty-six coils wound around the blanket modules.

As this manuscript is being written, the first proposition was rejected, in particular because of its large NRPs and because the ITER schedule implied to fix definitively the design of the cryostat (which would have required adaptation to implement these coils). The chosen design will then be one of the last two ones. The coils wound around the blanket modules are clearly better in terms of physics performances but are much more difficult to implement from the technical point of view than the coils wound around the miplane ports. In any case, there will probably be modifications to the designs presented above in order to make them even more realistic.

We saw that changes in the scenario do not present problems for edge ergodization, in the vacuum approximation: indeed, even if the RMPs amplitude typically decreases when q_{95} increases, this is compensated by the larger magnetic shear. However, the weaker RMPs could constitute a problem with respect to their penetration into the plasma. In

Design	Required current (kAt)	Islands widths (cm) on $q = 4/3$	Non res. pert.	Comments
A) 2 rows of 18 external coils	320-400	8	-	
B) 9 coils around midplane ports	140-200	9	=	Needs modif. to avoid NBI/RF ports; not "clean" $n = 3$
C) Blanket coils (4 rows, 0° tor. shift between rows)	22-28 (40% less if opt. phas.)	7.5	+	Good adaptability to $\neq$ scenarios
D) 18 coils around midplane ports	70-100	9	=	Not possible (some ports not free)
E) Side EFCCs	400	11	-	Nominal EFCCs current = 280kAt
F) (6+6) outside TF coils	600	8	-	Older version of A)
G) 2.(18+18) outside TF coils	600	8	-	Older version of A)
H) 2.(18+18) inside TF coils	900	8	-	Too large req. current
I) 2.(9+9) between VV and TF coils	300 upper / 720 lower	9	=	Too large req. current

Table 5.1: Summary of the $n = 3$ designs possiblities of ELMs control coils for ITER studied.

this respect, the coils wound around the blanket modules offer an interesting possibility of adaptation to q_{95}, which the other designs do not offer.

Finally, our calculations showed that variations in β_p and l_i do not constitute a problem since the RMPs amplitude is weakly sensitive on these parameters.

Chapter 6

Non-linear MHD modelling

6.1 Motivation

This last chapter is dedicated to a numerical modelling of ELMs control by RMPs with the aim to progress in the understanding of the physical mechanisms at play. It is indeed important in view of an application of this method of ELMs control to ITER to answer a number of open questions, such as:

1. Is the vacuum field approximation (that we used in all the work described in the preceding chapters and in particular in the work of design of ELMs control coils for ITER) correct? In other words: do the magnetic perturbations from the ELMs control coils penetrate into the plasma without being modified, or are they screened or, oppositely, enhanced by plasma effects?

2. What will be the impact of the ELMs control coils on the plasma toroidal rotation in ITER?

3. What mechanisms are responsible for the density pump-out observed in the experiments described in chapters 2 and 4?

4. Why are the energy confinement time and electron temperature not affected significantly by the ELMs control coils?

5. Is there a direct interaction between the magnetic perturbations from the ELMs control coils and the MHD P-B instabilities at the origin of ELMs?

The model that we used is non-linear reduced MHD. It is well adapted to address, at least partially, all the questions listed above. In a first subsection, we will explain what reduced MHD is. We will then describe our numerical simulations.

We will start with describing simulations for DIII-D in realistic geometry done with the JOREK code. The plasma magnetic response, with or without toroidal rotation, will be studied. In the case with toroidal rotation, we will see that the RMPs are screened by currents induced in the plasma, near the resonant surfaces. As we will explain, these rotation results should however not be considered as definitive since there are several key physics elements missing presently in JOREK. We will then see that the magnetic perturbations create interesting plasma convection cells near the unperturbed separatrix which could be playing a role in the experimental pump-out.

In order to progress in the physical understanding of the interaction of plasma rotation and external RMPs and implement the new physics elements needed for a correct modelling, it is convenient to use another non-linear reduced MHD code which is much simpler than JOREK and less demanding to run, due to the fact that it deals with a cylindrical geometry. We will present the results obtained so far with this code, which constitute a reference basis for future developments.

6.2 The reduced MHD model

The MHD equations [13, 82] are a combination of fluid and Maxwell equations that describe in a self-consistent way the evolution of the magnetic field $\vec{B}$, electric field $\vec{E}$, plasma mass density ρ, pressure p, velocity $\vec{v}$ and current density $\vec{j}$. The equations are:

$$\begin{aligned}
\partial_t \rho + \vec{\nabla} \cdot (\rho \vec{v}) &= 0, && (6.1)\\
\rho d_t \vec{v} &= \vec{j} \times \vec{B} - \vec{\nabla} p, && (6.2)\\
d_t (p/\rho^\gamma) &= 0, && (6.3)\\
\vec{E} + \vec{v} \times \vec{B} &= \eta \vec{j}, && (6.4)\\
\vec{\nabla} \times \vec{E} &= -\partial_t \vec{B}, && (6.5)\\
\vec{\nabla} \times \vec{B} &= \mu_0 \vec{j}, && (6.6)\\
\vec{\nabla} \cdot \vec{B} &= 0, && (6.7)
\end{aligned}$$

where $d_t \equiv \partial_t + \vec{v} \cdot \vec{\nabla}$ is the convective derivative, $\gamma = 5/3$ is the ratio of specific heats, η is the plasma resistivity (in ideal MHD, $\eta = 0$), and $\mu_0 = 4\pi.10^{-7}$ is the magnetic permeability of vacuum. These non-linear equations cannot be tackled analytically (except in particular, very simple cases) and thus require a numerical treatment. However, they demand quite large computational resources.

Reduced MHD is a simplified model, derived from the above equations, in which the number of scalar fields to be advanced in time is reduced and hence an analytical treatment is more feasible and, in the case of a numerical treatment, computational requirements are more reasonable. The first article introducing the reduced MHD equations, in cylindrical geometry and assuming a low plasma pressure, was written by Strauss in 1976 [83]. Several articles came later which introduced toroidal effects [85, 86] and a higher plasma pressure [84]. A recent rigorous derivation of the generalized reduced MHD equations can be found in [87].

Let us briefly outline the derivation of the reduced MHD equations. It is based on the assumption that the plasma is "strongly magnetized" along one given direction (typically the toroidal direction in tokamaks). Placing ourselves in cylindrical geometry and taking the axial direction z to be the direction of strong magnetization, this means that the plasma kinetic and thermal energies are small with respect to the magnetic energy corresponding to B_z: ρv^2 and $p \ll B_z^2/2\mu_0$. Under this assumption, it can be shown that the plasma motion is, to first order, incompressible and perpendicular to the direction of strong magnetization:

$$\vec{v} = \vec{v}_\perp = \vec{e}_z \times \vec{\nabla} u, \tag{6.8}$$

where u is thus the velocity potential (and also, to a factor B_z, the electric potential ϕ: $u = \phi/B_z$), $\vec{e}_z$ is the unitary vector in the z direction and the $=$ symbols should be

understood as "equal at first order". It can also be shown that B_z remains constant in time in first approximation, which makes it convenient to express the magnetic field in the following way:

$$\vec{B} = B_z \vec{e}_z + \vec{e}_z \times \vec{\nabla}\psi, \tag{6.9}$$

where ψ is the poloidal magnetic flux. Assuming a homogeneous plasma density and neglecting pressure terms, the reduced MHD model consists in only two equations, which are (in cylindrical geometry):

$$\partial_t \psi = \partial_z u + [\psi, u] + \eta J, \tag{6.10}$$
$$\partial_t w = [w, u] + [\psi, J] + \nu \triangle_\perp w, \tag{6.11}$$

where $w \equiv \triangle_\perp u \equiv \vec{e}_z \cdot (\vec{\nabla} \times \vec{v})$ is the vorticity in the z direction and $J \equiv \triangle_\perp \psi \equiv \vec{e}_z \cdot (\vec{\nabla} \times \vec{B})$ is (to a μ_0 factor) the current density in the z direction. The brackets are so-called "Poisson brackets", defined as: $[A, B] \equiv (\vec{\nabla} A \times \vec{\nabla} B) \cdot \vec{e}_z$ (Poisson brackets of the type $[A, u]$ represent an advection of the quantity A). These equations are those solved by the cylindrical code for which we will present results in section 6.4.

6.3 DIII-D simulations in realistic geometry using the JOREK code

This section is a reproduction with small modifications of an article accepted for publication in Physics of Plasmas [88]. The objective of this work was to simulate a DIII-D with ELMs control shot by the I-coils. We will begin by presenting the code adapted to our problem and then describe our results, which concern the plasma magnetic response to the I-coils perturbation with or without toroidal rotation and the plasma flows and transport induced by the I-coils perturbation. We will try to quantify the level of the induced transport in order to see if it could be playing a role in the experimentally observed density pump-out.

6.3.1 The JOREK code adapted to our problem

The JOREK code [80] is a 3D non-linear reduced MHD code able to simulate poloidally diverted tokamak plasmas in realistic geometry, including the X-point and the Scrape-Off Layer (SOL). The main purpose for which it was developed is the simulation of ELMs [81]. The JOREK equations are more complicated than equations 6.10 and 6.11 because they take into account the toroidal effects and do not consider the plasma density as

homogeneous. They however contain essentially the same physics. The equations are:

$$\partial_t \psi = (1+\varepsilon x)[\psi, u] + \eta J - \varepsilon \partial_\varphi u, \tag{6.12}$$

$$\begin{aligned} \hat{\rho}\partial_t w = & -\vec{\nabla}\hat{\rho}\cdot\vec{\nabla}u + (1+\varepsilon x)\hat{\rho}[w,u] + 2\varepsilon\hat{\rho}w\partial_y u \\ & -(1+\varepsilon x)\vec{\nabla}\hat{\rho}\cdot[u,\vec{\nabla}u] + \varepsilon\partial_y u\left(\vec{\nabla}\hat{\rho}\cdot\vec{\nabla}u\right) \\ & -\frac{\varepsilon}{(1+\varepsilon x)^2}\partial_\varphi J + \frac{1}{(1+\varepsilon x)}[\psi, J] + \nu\Delta_\perp w, \end{aligned} \tag{6.13}$$

$$\partial_t \rho = (1+\varepsilon x)[\rho, u] + 2\varepsilon\rho\partial_y u + \vec{\nabla}\cdot\left(D_\perp\vec{\nabla}_\perp\rho + D_\parallel\vec{\nabla}_\parallel\rho\right), \tag{6.14}$$

with the following definitions:

$$J \equiv \Delta^*\psi = (1+\varepsilon x)\partial_x\left(\frac{1}{(1+\varepsilon x)}\partial_x\psi\right) + \partial^2_{yy}\psi, \tag{6.15}$$

$$w \equiv \Delta_\perp u = \frac{1}{(1+\varepsilon x)}\partial_x\left((1+\varepsilon x)\partial_x u\right) + \partial^2_{yy}u, \tag{6.16}$$

$$\hat{\rho} \equiv \frac{R^2}{R_0^2}\rho, \tag{6.17}$$

and where the coordinates system (R, Z, φ) (R being the major radius, Z the vertical coordinate and φ the toroidal angle) has been used in the normalized form (x, y, φ), which is such that $R = R_0(1+\varepsilon x)$ and $Z = \varepsilon R_0 y$. R_0 is the major radius of the machine and $\varepsilon \equiv a/R_0$ is its inverse aspect ratio, with a the minor radius. The plasma mass density ρ is normalized to its value on axis ρ_0, all lengths are normalized to a, ψ is normalized to aB_0 with B_0 the toroidal magnetic field on axis, and time is normalized to the Alfvén time $\tau_A \equiv a(\mu_0\rho_0)^{1/2}/B_0$ (which is a typical MHD timescale). The Poisson brackets are defined by $[A, B] \equiv \partial_x A\partial_y B - \partial_x B\partial_y A$. Resistivity and viscosity have a dependency on the plasma density: $\eta \propto \nu \propto \rho^{-3/2}$. The SOL is modelled as a very low density plasma (typically, $\rho_{SOL} = 3\cdot 10^{-2}\rho_0$) which thus has a very large resistivity and viscosity. Only the $n = 0$ and $n = 3$ (the main component of the magnetic perturbations from the I-coils) toroidal harmonics are taken into account, and these harmonics interact with each other.

Our simulations are done for a realistic DIII-D equilibrium. We indeed take the equilibrium magnetic flux and current profile reconstructed by the EFIT code [56] for DIII-D shot 122336 and impose them in JOREK[1]. During the simulations, the equilibrium current profile is maintained by an appropriate toroidal electric field and the equilibrium poloidal magnetic flux is maintained constant at the boundary of the computation domain. We calculate the I-coils perturbation in terms of magnetic potential using the Biot and Savart formula:

$$\vec{A} = \frac{\mu_0}{4\pi}\sum_{i_{coil}=1}^{n_{coils}}\left(\oint_{coil_{i_{coil}}}\frac{I_{i_{coil}}d\vec{r}}{r}\right), \tag{6.18}$$

[1]To be precise, the equilibrium magnetic flux, $\psi^{n=0}$, is only imposed at the boundary of the computation domain. This piece of data, together with the current profile, is indeed sufficient for JOREK to calculate the complete equilibrium.

where $\vec{r}$ is the vector between the point where the magnetic potential $\vec{A}$ is calculated and the point moving along the coils during the integration. We then use this calculation in order to impose the external magnetic perturbations through the boundary conditions for $\psi^{n=3}$, the $n = 3$ harmonic of the poloidal magnetic flux[2]. Indeed, at the boundary, we impose:

$$\psi^{n=3} = (1 + \varepsilon x) A_{\varphi}^{n=3}. \tag{6.19}$$

The $(1 + \varepsilon x)$ factor comes from the fact that, in JOREK, in order to have $\vec{\nabla} \cdot \vec{B} = 0$, $\vec{B}$ has the following expression:

$$\vec{B} = \frac{B_0 R_0}{R} \vec{e}_{\varphi} + \frac{R_0}{R} \vec{e}_{\varphi} \times \vec{\nabla} \psi \tag{6.20}$$

$$= \frac{B_0 R_0}{R} \vec{e}_{\varphi} - \vec{\nabla} \times \left(\frac{\psi}{1 + \varepsilon x} \vec{e}_{\varphi} \right) \tag{6.21}$$

(in fact, there should also be a minus sign, but this just corresponds to a toroidal phase shift by 60°, which is not important). In the simulations, a perturbation corresponding to a current of 4kAt in the I-coils is switched on at $t = 0$, with a switch-on time of $100\tau_A$. More precisely, the current in the I-coils has the following expression:

$$I_{I-coils}[kAt] = 4 \cdot (1 - e^{-t/100\tau_A}). \tag{6.22}$$

6.3.2 Plasma magnetic response with or without rotation

A Poincaré plot obtained by field line integration for vacuum fields and for an I-coils current of 4kAt can be seen on fig. 6.1. This Poincaré plot for vacuum fields is used here as a basis of comparison for the Poincaré plots including the plasma response obtained with JOREK.

We first present a case without any toroidal rotation and where the parameters are: $S = Re = 10^5$, $D_{\perp} = 5 \cdot 10^{-7}$, $D_{\parallel} = 0$. Here, S is the Lundquist number, defined as: $S \equiv \frac{\tau_R}{\tau_A}$, with $\tau_R \equiv \frac{\mu_0 a^2}{\eta_0}$ the resistive time (η_0 being the resistivity on axis), and Re is the magnetic Reynolds number, defined as: $S \equiv \frac{\tau_V}{\tau_A}$, with $\tau_V \equiv \frac{a^2}{\nu_0}$ the viscous time (ν_0 being the viscosity on axis). A Poincaré plot done after an evolution of $700\tau_A$ is shown on fig. 6.2 (top). The islands are clearly smaller than the vacuum islands, which evidences the finite penetration time of the RMPs. There are indeed currents that develop inside the plasma in response to the magnetic perturbations and that slow down their penetration. These currents, which are mainly localized around the resonant surfaces, are represented on fig. 6.3. After a transient phase, however, the currents organize differently (but they do not disappear), so that at steady-state, the RMPs have fully penetrated. This can be seen on the Poincaré plot at $1200\tau_A$ (fig. 6.2, bottom). In other words, at steady-state, there are currents flowing in the plasma due to RMPs, but these currents do not modify significantly the islands widths.

Now, one of the main elements that affects the plasma magnetic response is known to be the toroidal rotation [75]. Unfortunately, it is not yet possible to simulate a toroidal

[2]We should underline here the fact that the I-coils are left outside of the computation domain. It would be more physical to include the I-coils inside the computation domain and model them directly as current distributions, but this would demand quite significant modifications of the code.

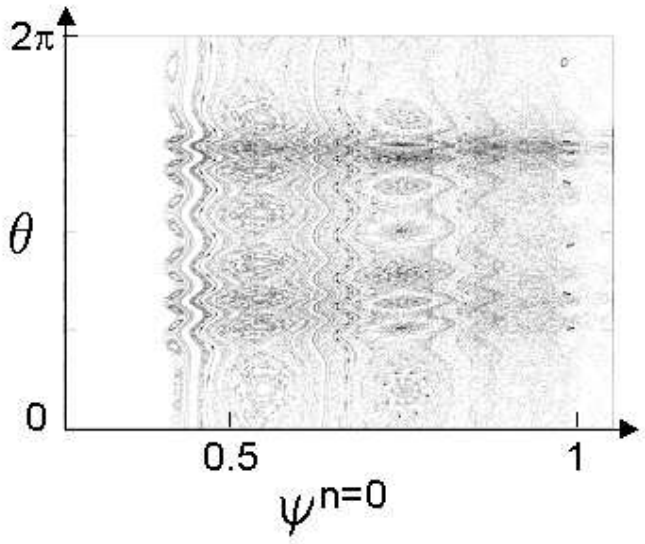

Figure 6.1: Poincaré plot for vacuum fields produced by the I-coils in even parity configuration, fed with 4kAt.

rotation of the plasma self-consistently with JOREK because the toroidal velocity v_φ is assumed to be null in the code (a version of JOREK including v_φ is under development with the help of the cylindrical code presented in section 6.4). Instead, a toroidal rotation of the external magnetic perturbations in front of a toroidally static plasma can be performed by replacing φ by $\varphi - \Omega_{rot}t$ in the boundary conditions for $\psi^{n=3}$, which become: $\psi^{n=3}(R,Z,\varphi,t) = \psi^{n=3}(R,Z)cos(3(\varphi - \Omega_{rot}t)$. This is assumed to be equivalent to a solid-body-like rotation of the plasma in front of static I-coils. Notice that this is quite restrictive since in reality the toroidal rotation of the plasma is strongly sheared, i.e. far from a solid body rotation. Also, since v_φ is assumed to be null, the effect of the toroidal torque exerted by the I-coils on the plasma (a key ingredient in the physics of RMPs penetration into a rotating plasma, as explained in section 6.4.2) cannot be observed. In the example given here, the rotation pulsation (normalized to the inverse of the Alfvén time) is $\Omega_{rot} = \frac{2\pi \cdot 10^{-3}}{3}$, which corresponds approximately to the experimental value for the pedestal ($\sim$ 2kHz) in DIII-D [36]. Parameters are still $S = Re = 10^5$. One can see on the Poincaré plots at $700\tau_A$ (fig. 6.4, top) and $1200\tau_A$ (fig. 6.4, bottom) that the islands are thinner (by a factor $\sim$2) than in the case without rotation, evidencing a screening of the RMPs due to the toroidal rotation. We however stress that these results are not definitive. This is due, on the one hand, to the key physics elements missing in JOREK (in particular self-consistent plasma rotation including braking by magnetic perturbations[3]) and, on the other hand, to the very unrealistic value of the resistivity and viscosity (two parameters which are known to play a central role in RMPs penetration

[3]but also other phenomena which will be presented in section 6.4.2, such as diamagnetic rotation, neoclassical poloidal viscosity, ...

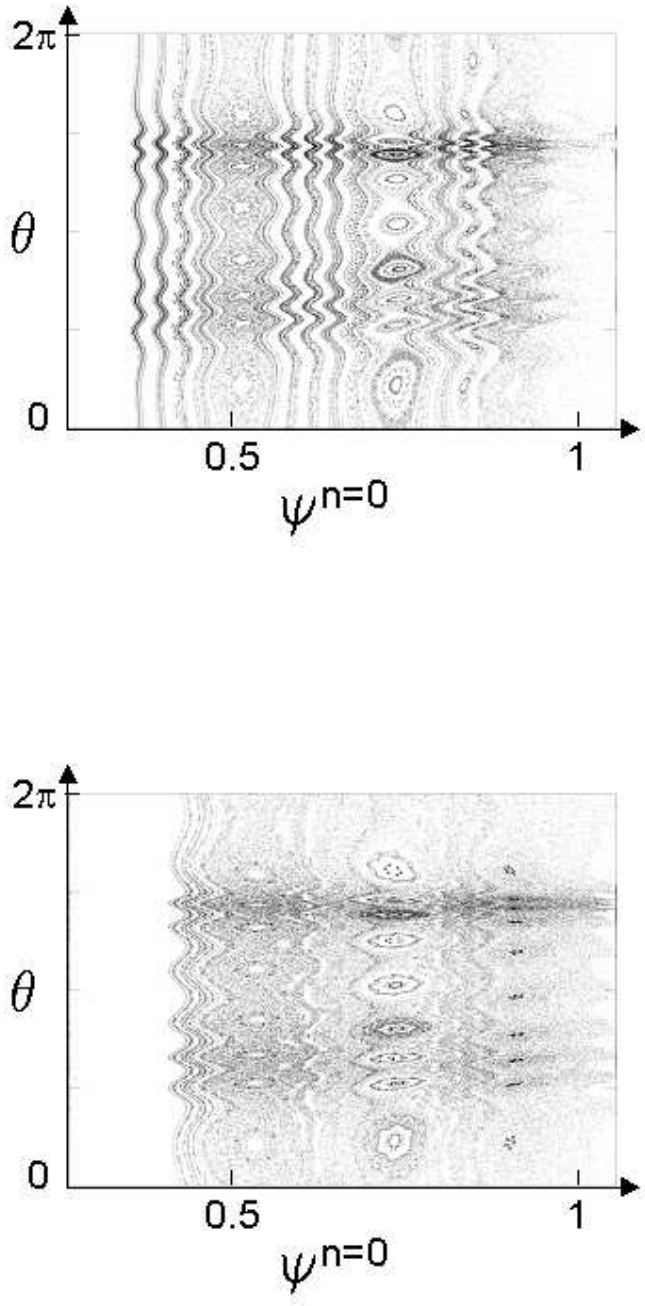

Figure 6.2: Poincaré plots including plasma response from a JOREK simulation without any toroidal rotation, at $t = 700\tau_A$ (upper plot) and $t = 1200\tau_A$ (lower plot).

Figure 6.3: Perturbations of the toroidal current density ($J^{n=3}$) at $t = 700\tau_A$ for the JOREK simulation without any toroidal rotation.

into a rotating plasma). As this manuscript is being written, work is ongoing in CEA in order to treat the problem correctly. For this, the cylindrical code is very helpful, as will be explained in section 6.4.

6.3.3 Description of a density transport mechanism due to RMPs

We now focus on simulations without any toroidal rotation and study the transport due to RMPs. It is a general feature of the simulations that, after a transient phase, steady-state structures of the $n = 3$ harmonic of the velocity potential ($u^{n=3}$) appear (fig. 6.5), which have a clear resonant aspect.

On a cut of $u^{n=3}$ (fig. 6.6) along the AB line from fig. 6.5, one can see indeed that they are localized around the $q = 8/3$ and $q = 9/3$ surfaces (where they have the corresponding poloidal symmetry $m = 8$ and $m = 9$) and also around the separatrix, where $u^{n=3}$ takes its largest values (there the poloidal symmetry is difficult to estimate because of fine structures around the X-point, but seems to be about $m = 10 - 12$). These structures of $u^{n=3}$ around the unperturbed separatrix are remindful of the peeling-tearing mode described in [80]. This similarity is reinforced by the observation that the structures are linked to the imposed current at the edge (which is supposed to simulate the bootstrap current). However, here the plasma is intrinsically stable: if no external magnetic perturbations are applied, these structures do not appear.

Associated to the structures of $u^{n=3}$ is a plasma $\vec{E} \times \vec{B}$ drift velocity: plasma flows along the isopotential lines. In particular, plasma flows radially across the unperturbed separatrix due to the local structure of $u^{n=3}$. This can be seen on fig. 6.7, which represents

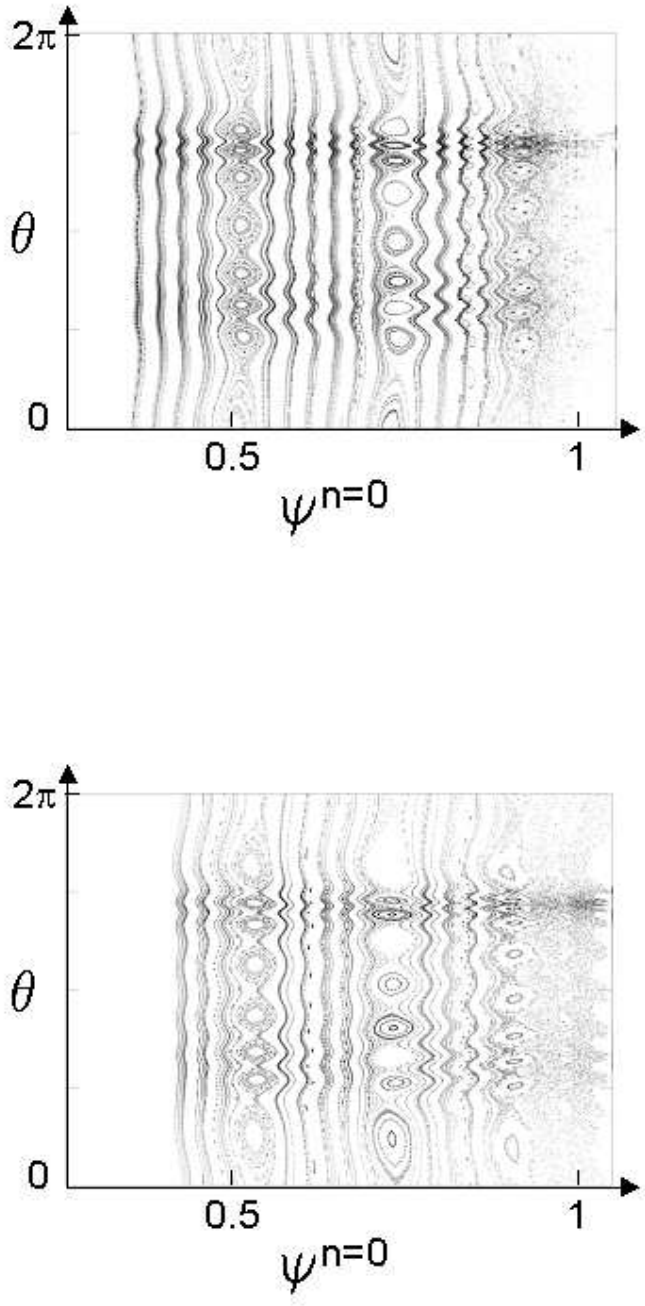

Figure 6.4: Poincaré plots including plasma response from a JOREK simulation with a typical pedestal-like toroidal rotation, at $t = 700\tau_A$ (upper plot) and $t = 1200\tau_A$ (lower plot).

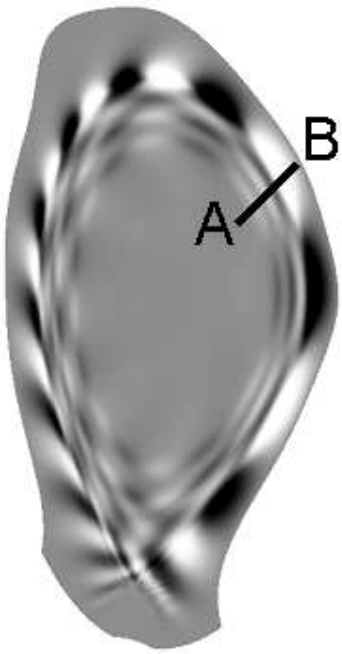

Figure 6.5: Perturbations of the velocity potential ($u^{n=3}$) at $t = 700\tau_A$.

the plasma density for the simulation with $S = Re = 10^5$, after an evolution of $2500\tau_A$. On this figure, one can clearly see plasma fingers that have crossed the unperturbed separatrix due to $\vec{E} \times \vec{B}$ convection in the steady-state $u^{n=3}$ field that appears on fig. 6.5. These fingers are observable because there is no parallel plasma transport in the simulation, so that plasma contained in the fingers is not removed although it has reached a region of open field lines with short connection lengths. If parallel transport was present, the plasma contained in the fingers would be removed, resulting in a pump-out of the density.

This $\vec{E} \times \vec{B}$ flow due to the steady-state $u^{n=3}$ structures around the unperturbed separatrix is therefore an interesting candidate in the perspective of understanding the experimental pump-out. However, since the simulations are done at a much larger resistivity than the experimental one, it is important to know the evolution of this mechanism as resistivity becomes smaller. One can see on fig. 6.6 that the structures of $u^{n=3}$ depend on resistivity (and/or viscosity, since we keep $S = Re$ while scanning the resistivity): higher resistivity gives a larger amplitude of the peaks around the resonant surfaces and a larger broadness of the peak around the separatrix. This has as a consequence the fact that the convective transport decreases with resistivity, as can be seen on fig. 6.8, which presents the diffusive and convective fluxes across the unperturbed separatrix for different resistivities. On this figure, one can see that the convective flux grows in time at the beginning of the simulations, which corresponds to the establishment of the $u^{n=3}$ structures and formation of plasma fingers, reaches a maximum (except for the case $S = Re = 2 \cdot 10^5$ because the simulation has not been pushed far enough in time) and starts to decrease slowly. The diffusive flux is decreasing from the beginning, which is a consequence of both the absence of particle source in the simulations and the competition with the convective flux. One can see that the maximum of the convective flux decreases when the Lundquist

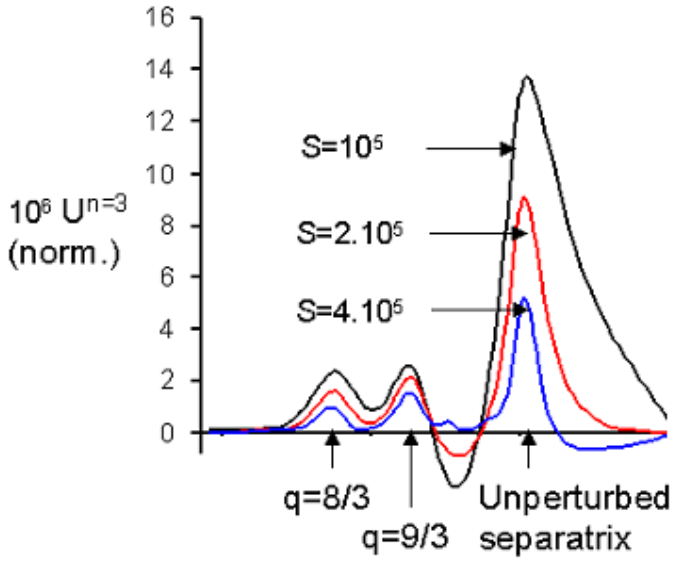

Figure 6.6: Cut of the perturbations of the velocity potential $u^{n=3}$ along the AB line from fig. 6.5.

Figure 6.7: Colour plot of the plasma density at $t = 2500\tau_A$ for a simulation with $S = Re = 10^5$.

number becomes larger (i.e. when resistivity becomes smaller) and that the diffusive flux is already dominating the convective flux at $S = Re = 4 \cdot 10^5$.

Let us now evaluate the realistic Lundquist number. The resistivity in $\Omega \cdot m$ is: $\eta = 1.65 \cdot 10^{-9} \cdot ln\Lambda \cdot T_e^{-3/2}$, where T_e should be expressed in keV. The Coulomb logarithm [2], $ln\Lambda$, has a weak dependency on density and we take here $ln\Lambda = 17$. In the experiment, the electron temperature at the top of the pedestal is $T_e \simeq 1$keV. This gives $\eta \simeq 2.8 \cdot 10^{-8}$, i.e. a Lundquist number $S \simeq 1.3 \cdot 10^8$.

It is very difficult to use the curves from fig. 6.8 in order to extrapolate the convective flux to the realistic parameters, because in the simulations with a small resistivity, the convective flux is blurred by the diffusive flux. It is more relevant to take the value of the convective flux for the simulation with $S = Re = 10^5$, when the convective flux is not blurred by the diffusive one, and apply a scaling factor (with respect to the Lundquist number) calculated from the amplitude of the $u^{n=3}$ peak in the ergodic region, which appears in fig. 6.6 (notice that the poloidal mode number does not change with resistivity, meaning that the radial velocity and convective flux are proportional to the amplitude of $u^{n=3}$).

In order to determine the scaling of the amplitude of the electric potential structures as a function of resistivity, we also did simulations with the cylindrical code (see section 6.4), which is more convenient for basic physics studies and allows to explore lower resistivities than JOREK. RMPs with an $(n = 1, m = 4)$ symmetry were imposed as boundary conditions. On fig. 6.9, one can see that steady-state $(n = 1, m = 4)$ structures of the velocity potential are induced around the $q = 4$ surface, which are very similar to what is observed in the JOREK simulations.

Fig. 6.10 presents the amplitude of the peak in the $n = 1$ velocity potential, denoted u_{max}, as a function of the normalized resistivity $\eta \equiv S^{-1}$ for a range of RMPs amplitudes, together with points from the JOREK simulations. It can be observed that, when η becomes very small, u_{max} has a linear dependency on η. The qualificative "very small" should be understood here with respect to the amplitude of the magnetic perturbations: indeed, as can be seen on fig. 6.10, the regime of linear dependency is reached at smaller η for smaller amplitudes of the RMPs.

It is not straightforward to compare the JOREK simulations with the cylindrical code simulations, however it can be seen that the points obtained with JOREK show a similar trend to the points from the cylindrical code. It seems therefore reasonable to extrapolate that at the realistic Lundquist number $S \simeq 1.3 \cdot 10^8$, the electric potential structures will be a factor of 100 to 1000 smaller than calculated with JOREK at $S = 10^5$. The convective flux should consequently also be a factor 100 to 1000 smaller.

We now have to take into account the fact that the diffusive flux in our simulations is overestimated, due to two reasons: the first one is that our perpendicular normalized diffusivity $D_\perp$ corresponds to a value in physical units of $D_\perp \sim 1.5 m^2/s$, which is about 15 times larger than the typical value in the pedestal, and the second one is that our radial density gradient (at t=0) is larger by a factor $\sim$2 than the realistic one. Thus, we can roughly estimate that the diffusive flux at t=0 is $\sim$30 times larger than the realistic diffusive flux.

To finish, we should notice that the maximal convective flux at $S = 10^5$ is $\sim$1.5 times larger than the diffusive flux at t=0.

Therefore, if all the parameters were set to their experimental value, the convective flux would be between $\frac{1.5 \cdot 30}{1000} = 4.5\%$ and $\frac{1.5 \cdot 30}{100} = 45\%$ of the diffusive flux, i.e. between

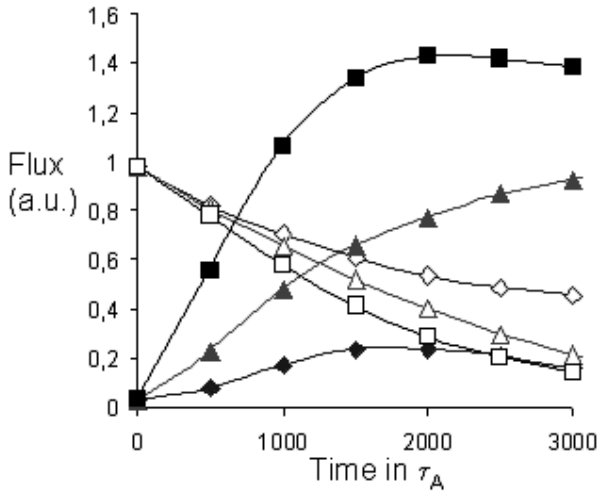

Figure 6.8: Convective (full symbols) and diffusive (open symbols) fluxes across the unperturbed separatrix for three simulations: $S = Re = 10^5$ (squares), $S = Re = 2 \cdot 10^5$ (triangles) and $S = Re = 4 \cdot 10^5$ (diamonds).

almost negligible and quite significant. Thus, we are not able to decide here if our candidate mechanism is really playing a role in the experiments: that depends on the scaling with resistivity. All we can say for now is that it could be playing a role if the scaling with resistivity is somewhat weaker than linear (i.e. $\propto \eta^{2/3}$ for instance).

6.4 RMPs penetration in cylindrical geometry

As stated above, the JOREK simulations, in spite of the correct treatment of the geometry, cannot pretend to give reliable results as to the RMPs penetration into the plasma: more physics requires to be included and the resistivity needs to be pushed to much lower values. In order to do that, it is convenient to use the cylindrical code, for several reasons:

- it is much less demanding in terms of numerical resources (due mainly to the fact that the equations are solved in the Fourier space for the poloidal and toroidal angles);
- the simple geometry makes the development of the equations and the interpretation of the results easier;
- the analytical theory for RMPs penetration in cylindrical geometry is well established [75], providing a basis for analyzing the simulation results.

Nevertheless, it is clear that performing a realistic simulation of RMPs penetration requires much work, and we did not manage this objective was not reached in the present

Figure 6.9: Poloidal cut of the typical steady-state $n = 1$ component of the velocity potential, $u^{n=1}$, generated by the $(n = 1, m = 4)$ RMPs around the $q = 4$ surface in simulations with the cylindrical code.

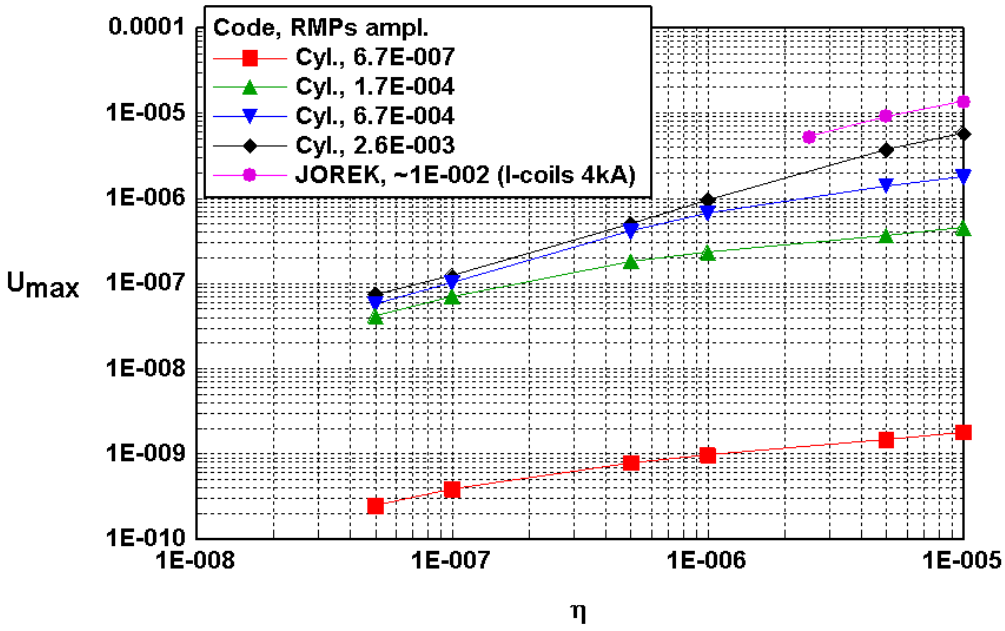

Figure 6.10: Maximal value of the velocity potential structures generated by RMPs for simulations with the cylindrical code (for a range of RMPs amplitudes) as well as for JOREK simulations, as a function of the normalized resistivity $\eta \equiv S^{-1}$.

work. However, we report here on first simulations using the cylindrical code which constitute a basis for future developments. We first present simulations of the RMPs penetration into the plasma without any rotation, before presenting results in presence of a rotation from the external RMPs (like JOREK, the cylindrical code assumes a zero plasma toroidal velocity).

Equations 6.10 and 6.11 are solved numerically in the Fourier space, taking into account only the $(n = 0, m = 0)$ (equilibrium) and $(n = 1, m = 3)$ (perturbations) components, where m is the poloidal mode number and n is the mode number in the z direction, which is assumed to be periodic (z is the equivalent of $R_0\varphi$ in toroidal geometry, R_0 being the major radius). We impose external RMPs by fixing the value of the $(n = 1, m = 3)$ harmonic of the magnetic flux, $\psi_{3/1}$, at the boundary of the computation domain. The equilibrium current profile is chosen such that there is a $q = 3$ surface inside the plasma and such that the plasma is stable if no external magnetic perturbation is applied.

6.4.1 RMPs penetration without rotation

In order to study the penetration of the external RMPs, we switch them on at $t = 0$, with, as in the JOREK simulations, a switch-on time of $100\tau_A$:

$$\psi_{3/1}(r_{bnd}) = \psi^0_{3/1}(1 - e^{-t/100\tau_A}), \tag{6.23}$$

r_{bnd} being the radius of the boundary of the computation domain[4] and $\psi^0_{3/1}$ the amplitude of the imposed RMPs (when not precised, other notations, such as τ_A, are the same as for the section on JOREK).

We first present a scan in Lundquist number S and magnetic Reynolds number Re where we kept $S = Re$. Fig. 6.11 represents the temporal evolution of $|\psi_{3/1}|$ (the module of the complex number $\psi_{3/1}$) on the $q = 3$ surface, for S from 10^5 to 10^8, the latter value being typical for plasmas with $T_e \sim 1$keV, while the former value corresponds to very cold plasmas ($T_e \sim 10$eV). A curve corresponding to the vacuum case is also shown. It appears clearly that there is a finite penetration time of the RMPs into the plasma, which increases as S increases, i.e. as the resistivity η decreases. It is also interesting to notice that for the lowest value of S, the final value of $|\psi_{3/1}|$ almost coincides with the vacuum value whereas for the other cases, $|\psi_{3/1}|$ significantly overcomes the vacuum value. This is intrepeted as an amplification of external RMPs by a plasma that is stable but close to the threshold with respect to a tearing instability, a phenomenon known from theory [75]. However, this amplification can occur only in the case where η is small enough. Indeed, it is due to perturbation currents appearing in a layer centered on the resonant surface (as we will see below), called the "resistive layer". The width of the resistive layer increases with η, and if η is large enough (in our case, for $S = 10^5$), it can reach a size comparable to the minor radius of the machine a, in which case the current in the resistive layer is influenced by the boundary conditions, which prevents from an amplification of the external RMPs.

Let us now focus on the $S = Re = 10^7$ case. Fig. 6.12 (resp. fig. 6.13) presents the profiles of $|\psi_{3/1}|$ (resp. the real part of the perturbation axial current $\Re(J_{3/1})$) at three

[4]Typically, we take $r_{bnd} = 1.1 \cdot a$, with a the minor radius of the plasma. We indeed assume that the plasma is surrounded by a vacuum region, which we simulate by imposing a very large resistivity for $r > a$.

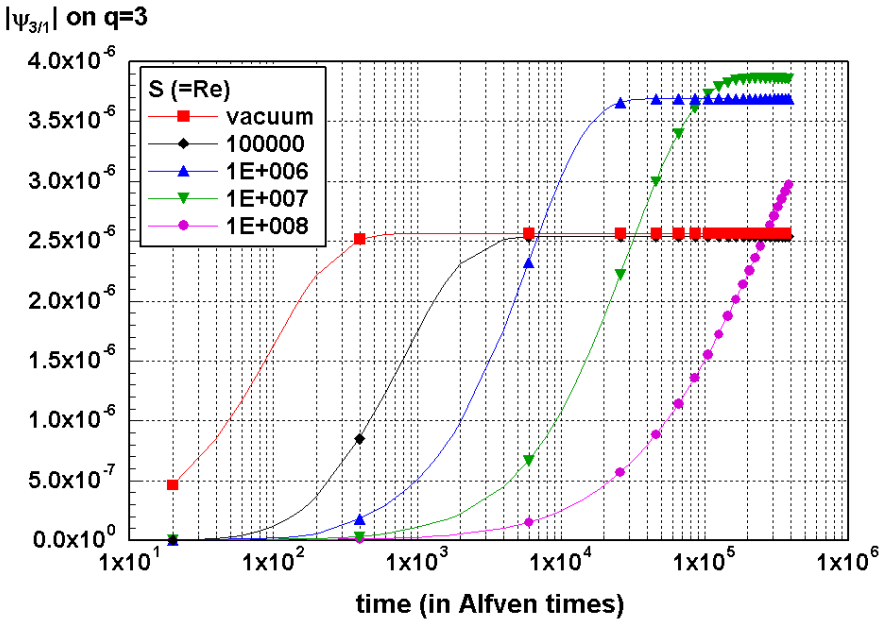

Figure 6.11: Temporal evolution of the perturbation magnetic flux $|\psi_{3/1}|$ on the $q = 3$ surface, for different values of $S = Re$ as well as for the vacuum case.

different times in the simulation. At $t = 2 \cdot 10^3$ (in τ_A units), the screening is almost total (see also the Poincaré plot on fig. 6.14 [upper right plot], displaying very small islands) and is associated to a perturbation current profile presenting one single peak centered on the $q = 3$ surface, which can be seen also in a poloidal cut of $J_{3/1}$ on fig. 6.14 (upper left plot). At $t = 10^4$, the penetration is partial and the perturbation current profile starts to present two peaks of opposite signs. At $t = 4 \cdot 10^5$, the penetration is full (see also the Poincaré plot on fig. 6.14 [lower right plot], with the islands appearing clearly), with still the same shape of the perturbation current profile as at $t = 10^4$, but a larger amplitude of it (see also fig. 6.14 [lower left plot]). The $|\psi_{3/1}|$ profile is clearly different from the vacuum one (which is also shown on fig. 6.12 for comparison), demonstrating the strong plasma effect in this simulation.

6.4.2 RMPs penetration with rotation

We now study the impact of rotation on the RMPs penetration. Let us start with a short overview of the theoretical results in this domain before presenting our simulation results.

Theory

We summarize here the theory of Fitzpatrick, which is often cited as a reference, and can be found in [75]. First of all, we stress that, in this theory, "rotation" refers to the toroidal rotation of the plasma. The poloidal rotation is indeed assumed to be unchanged by the RMPs because it is fixed, according to neoclassical theory [74], to a well defined

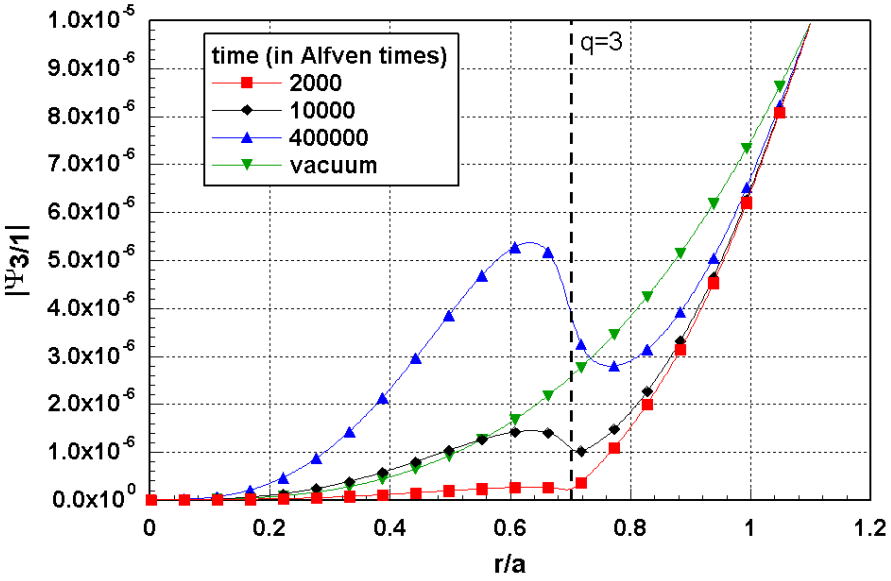

Figure 6.12: Profiles of $|\psi_{3/1}|$ from the $S = 10^7$ simulation, at three different times, together with a vacuum profile.

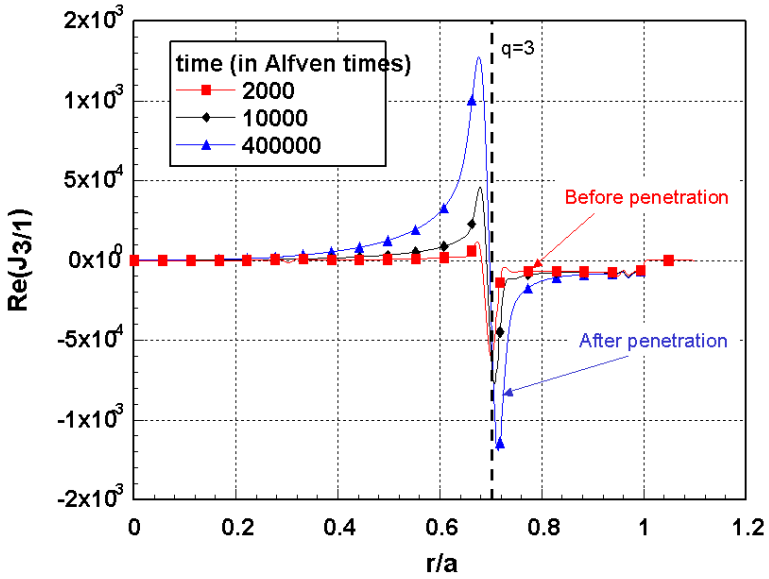

Figure 6.13: Profiles of $\Re(J_{3/1})$ from the $S = 10^7$ simulation, at the same three different times as fig. 6.12.

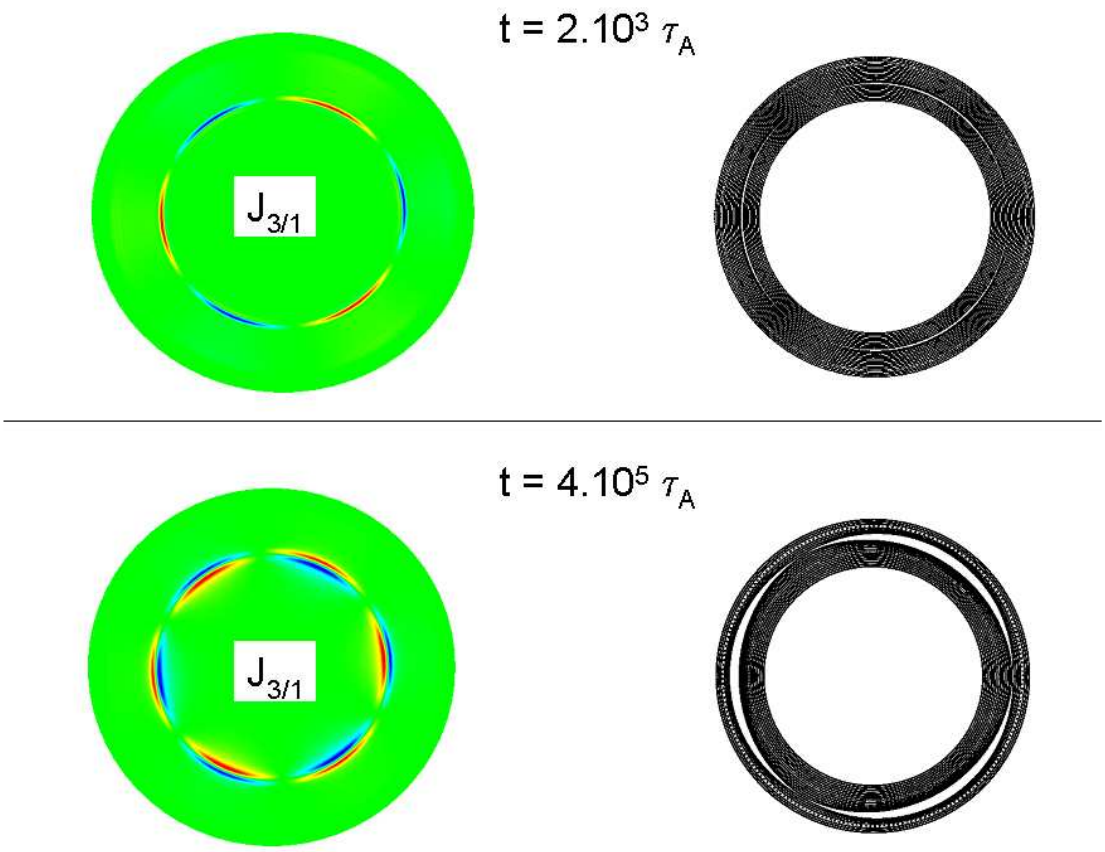

Figure 6.14: Poloidal cuts of $J_{3/1}$ and Poincaré plots, both at $z = 0$, for two different times: one before ($t = 2 \cdot 10^3$) and one after ($t = 4 \cdot 10^5$) RMPs penetration.

value due to the neoclassical poloidal viscosity[5]. The poloidal rotation is therefore not considered as a degree of freedom, oppositely to the toroidal rotation.

The Fitzpatrick theory predicts that at fixed plasma rotation velocity, static external magnetic perturbations are screened, due to currents appearing in the plasma, in the following way:

$$\psi_{real}^{pert} = \frac{2m}{-\Delta' + i\omega_{slip}\tau_{layer}}\psi_{vac}^{pert}, \tag{6.24}$$

where ψ_{real}^{pert} is the actual value of the perturbation of the poloidal magnetic flux at the resonant surface, ψ_{vac}^{pert} is its vacuum value, i.e. the value that it would have if there were no currents flowing in the plasma, Δ' is the well known tearing stability index of the plasma [2] (which is negative for a tearing-stable plasma), ω_{slip} is the so-called "slip frequency" of the mode, defined by $\omega_{slip} \equiv m\Omega_\theta - n\Omega_\varphi$, Ω_θ and Ω_φ being the poloidal and toroidal angular rotation frequencies of the plasma, and finally τ_{layer} is a typical time constant for the resistive layer, which depends in particular on the plasma resistivity and viscosity.

Fitzpatrick also predicts that the external magnetic perturbations induce a $\vec{j} \times \vec{B}$ force, localized in the resistive layer, which is opposite to the plasma rotation. The induced local, so-called "resonant", braking is counterbalanced by viscous forces which tend to make the resistive layer rotate at the same velocity as the rest of the plasma. The strength of the resonant braking torque T_{RB} is a non-monotonic function of ω_{slip}, represented on fig. 6.19, which tends towards 0 for either very small or very large values of ω_{slip}:

$$T_{RB} \propto \frac{\omega_{slip}\tau_{layer}}{(-\Delta')^2 + (\omega_{slip}\tau_{layer})^2}|\psi_{vac}^{pert}|^2. \tag{6.25}$$

In the Fitzpatrick theory, the toroidal velocity at the edge of the plasma is assumed to remain constant in time, which roughly accounts for an injection of momentum by external means (e.g. by NBI). In that case, for given plasma resistivity and viscosity and a given initial rotation profile, if static external RMPs are turned on at $t = 0$, the plasma will be locally braked down at the resonant surface. Due to the dependence of the braking torque on the slip frequency, the braking at final state will in general not be a smooth function of the RMPs amplitude, but there will exist a threshold value separating two domains[6]:

- below the threshold, the resonant braking force will remain small and will be easily counterbalanced by viscous forces for a small variation of the toroidal velocity at the resonant surface[7], and the RMPs will remain screened;
- above the threshold, the resonant braking force will be large enough to significantly brake down the rotation at the resonant surface, leading to a reduction in the slip frequency which will induce a further increase in the strength of the braking force.

[5]Neoclassical poloidal viscosity is a consequence of the friction of passing particles on banana particles, which do not possess any poloidal momentum.

[6]This is true under the condition that the initial rotation is fast enough, i.e. ω_{slip} is at the right of the value which maximizes T_{RB} (cf. fig. 6.19), which is most often the case in tokamaks.

[7]ω_{slip} will stay at the right of the value which maximizes T_{RB}

The final braking will then be very significant, with the rotation almost stopped at the resonant surface[8], and the RMPs will penetrate into the plasma. This is the archetype of a mode locking [2] process.

A similar behaviour is expected when scanning the plasma rotation at fixed RMPs amplitude: there exists a threshold in plasma rotation between a "screening regime" and a "mode locking regime".

Simulations

In our code, we do not have an equation for the toroidal plasma velocity. We are therefore not able to place ourselves in the conditions of the Fitzpatrick theory. However, since we do not take into account the neoclassical poloidal viscosity, the poloidal rotation is a degree of freedom for us. According to the Fitzpatrick theory, the $\vec{j} \times \vec{B}$ force due to the external RMPs is perpendicular to the field lines and it thus possesses a poloidal component. The typical processes described above for the toroidal rotation can thus be expected to take place also in our simulations, but for the poloidal rotation instead of the toroidal rotation. In our simulations, the plasma poloidal rotation is null at $t = 0$ and we rotate the external magnetic perturbations by imposing:

$$\psi_{3/1}(r_{bnd}) = \psi^0_{3/1}(1 - e^{-t/100\tau_A})e^{i\omega t}, \tag{6.26}$$

with a given frequency[9] ω. The equilibrium current profile is the same as in the simulations without any rotation presented above.

We first present two scans done at fixed resistivity and viscosity ($S = Re = 10^7$): one in RMPs amplitude at constant rotation frequency and one in rotation frequency at constant RMPs amplitude.

Fig. 6.15 presents the results of the scan in RMPs amplitude. The top plot shows the time evolution of $|\psi_{3/1}|$ at the $q = 3$ surface for four values of $\psi^0_{3/1}$ between 10^{-6} and 10^{-5} (normalizations are the same as for JOREK), the RMPs rotation frequency being fixed at $\omega = 10^{-4}$. Curves from simulations without any external RMPs rotation ($\omega = 0$) are also shown for comparison (dashed curves). It can be seen that the RMPs always penetrate more slowly with than without rotation. For $\psi^0_{3/1} = 10^{-6}$, the simulation is even too short to tell if the RMPs penetrate or not. The bottom plot shows, for the same simulations, the time evolution of the $(m = 0, n = 0)$ component of the poloidal velocity, v_{pol}. This plot evidences the fact that the rotation of the external RMPs induces a poloidal rotation of the plasma (in the cases without RMPs rotation, no plasma rotation appears) which tends to set the slip frequency to zero. This corresponds to the scenario described in the Fitzpatrick theory, but instead of a plasma braking imposed by static RMPs, we have a plasma spin-up imposed by rotating RMPs. Indeed, reading from fig. 6.15, the rotation velocity tends to the value $v_{pol} \simeq -2.3 \cdot 10^{-5}$, which is the rotation velocity of the external perturbations[10], and the RMPs penetration time is clearly very close to the time of onset of the poloidal rotation.

[8] ω_{slip} will now be at the left of the value which maximizes T_{RB}

[9] pulsation in fact

[10] Since the perturbations have a poloidal mode number $m = 3$, their velocity on the $q = 3$ surface (which is located at $r/a \simeq 0.7$ [see fig. 6.11]), is indeed $v_{pol}^{RMPs} \simeq -0.7 \cdot \omega/3 = -2.3 \cdot 10^{-5}$.

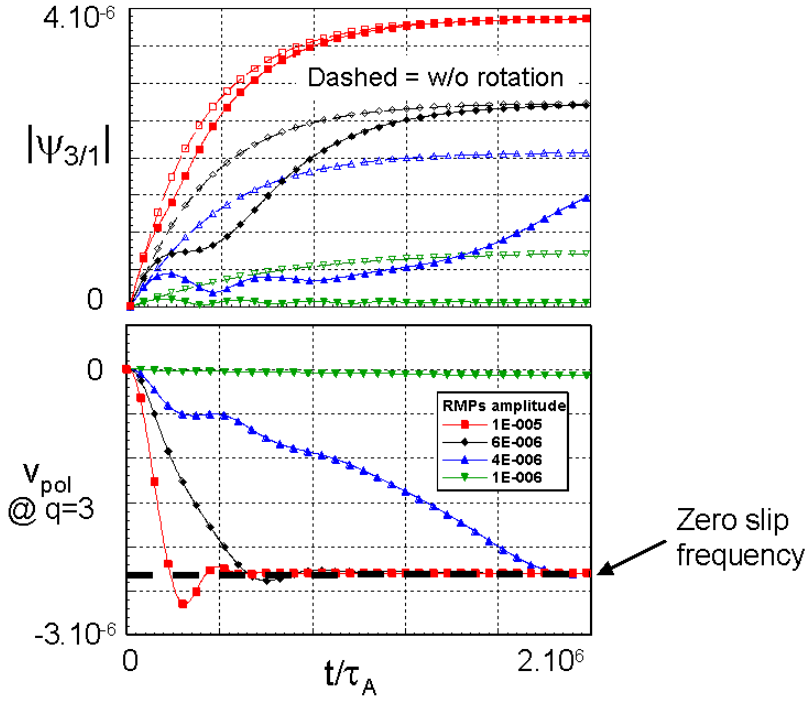

Figure 6.15: Temporal evolution of $|\psi_{3/1}|$ and v_{pol} on the $q = 3$ surface for different values of $\psi^0_{3/1}$ and a fixed $\omega = 10^{-4}$. On the top plot, dashed lines correspond to $\omega = 0$ cases, for comparison (in these cases, v_{pol} on the $q = 3$ surface remains null).

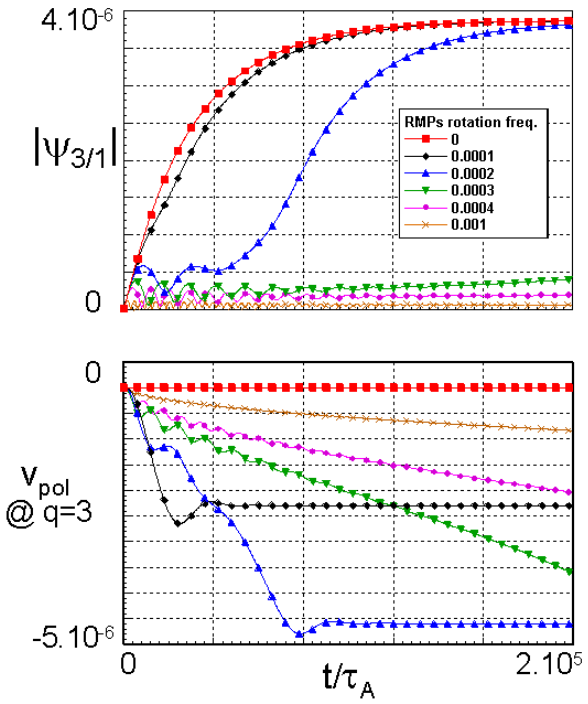

Figure 6.16: Temporal evolution of $|\psi_{3/1}|$ and v_{pol} on the $q = 3$ surface for different values of ω and a fixed $\psi^0_{3/1} = 10^{-5}$.

Fig. 6.16, which presents the results of a scan in ω (six values between 0 and 10^{-3}) at fixed $\psi^0_{3/1}$ ($= 10^{-5}$), confirms these findings: it can again be observed that the RMPs rotation induces a plasma rotation at the same velocity, associated to the RMPs penetration.

Doing the two above scans, we thus found a good qualitative agreement with theory, but we did not demonstrate clearly the existence of two distinct domains separated by a threshold value of $\psi^0_{3/1}$ or ω described in the Fitzpatrick theory. Instead, we present, to finish, another study where a similar effect is clearly observed. This consists in a scan in the viscosity for the $(m = 0, n = 0)$ component of the flow, which we denote $visco_0$ [11], at fixed $\psi^0_{3/1}$ and ω. The time evolutions of $|\psi_{3/1}|$ and v_{pol} on the $q = 3$ surface are presented on fig. 6.17 and their steady-state values as functions of $visco_0$ on fig. 6.18. It clearly appears that there are two different types of steady-states depending on the value of $visco_0$:

- for $visco_0 < 4 \cdot 10^{-6}$ (the numerical value of $visco_0$ corresponds to the inverse of the magnetic Reynolds number), v_{pol} at $q = 3$ can approach the rotation velocity of the external RMPs and RMPs penetration take place;
- for $visco_0 > 4 \cdot 10^{-6}$, v_{pol} at $q = 3$ remains small and RMPs penetration is prevented.

[11] We kept the viscosity for the flow perturbations constant, in order to show that the effect was really due to $visco_0$.

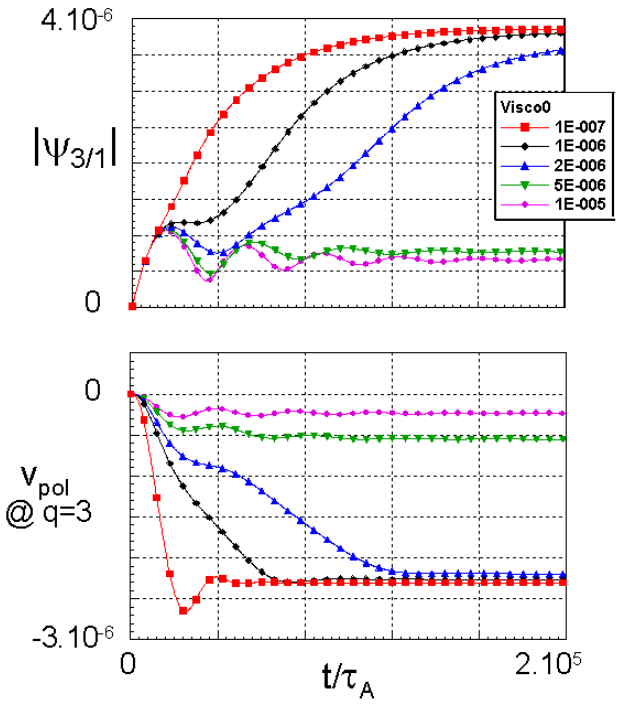

Figure 6.17: Temporal evolution of $|\psi_{3/1}|$ and v_{pol} on the $q = 3$ surface for different values of the axisymmetric viscosity $visco_0$, at fixed $\psi^0_{3/1} = 10^{-5}$ and $\omega = 10^{-4}$.

On fig. 6.19, we present a conceptual sketch which helps to interprete this result. The amplitudes of the (normalized) resonant braking torque T_{RB} and viscous torque T_{visc} are represented as functions of the slip frequency ω_{slip}. They are not calculated numerically: we just gave them a plausible appearance. In particular, for T_{RB}, we took the expression 6.25. As to T_{visc}, we represented it as a linear function of the rotation frequency on the resonant surface (since the "natural" rotation frequency of the rest of the plasma is zero), which is in fact the difference between the value of ω_{slip} at $t = 0$ and the actual ω_{slip}. T_{visc} is thus represented on fig. 6.19 as a straight line crossing the horizontal axis at the value of ω_{slip} at $t = 0$ (point A). The slope of the line increases with $visco_0$. On fig. 6.19, we represented two cases, one for $visco_0$ below the threshold and one for $visco_0$ above the threshold. The final state is determined by the equilibrium between T_{RB} and T_{visc}. For the small $visco_0$, the intersection is on the left of the maximum of T_{RB} with a small final ω_{slip} (point C), while for the large $visco_0$, the intersection is on the right of the maximum, and ω_{slip} remains high (point B), which qualitatively corresponds to the simulation results.

6.5 Summary

In order to progress in the understanding of the physical mechanisms at play in ELMs control by RMPs, we performed numerical simulations with non-linear reduced MHD codes.

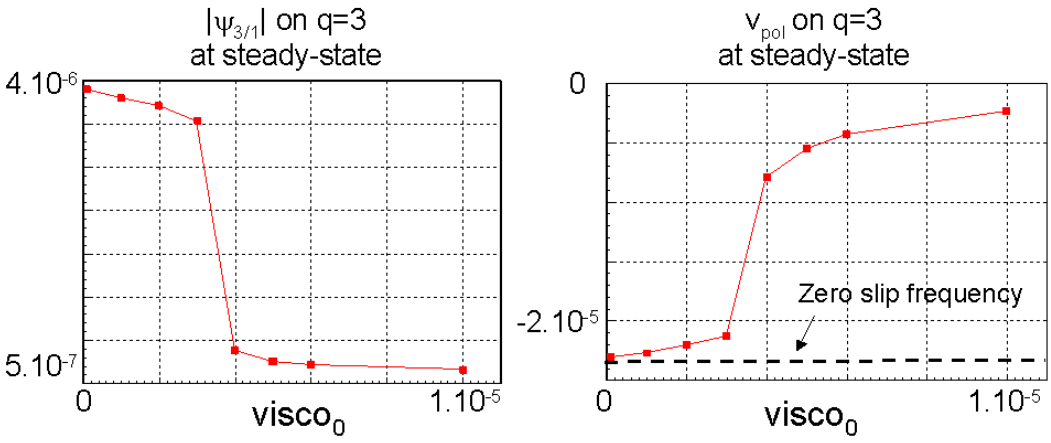

Figure 6.18: Values of $|\psi_{3/1}|$ and v_{pol} on the $q = 3$ surface at steady-state as a function of the axisymmetric viscosity $visco_0$, for fixed $\psi^0_{3/1} = 10^{-5}$ and $\omega = 10^{-4}$.

A DIII-D case was simulated in realistic geometry with the JOREK code. It was found that the magnetic response from the plasma is small in the absence of toroidal rotation, the islands being very similar to the vacuum islands. In order to simulate a plasma toroidal rotation, we imposed a toroidal rotation of the external magnetic perturbations, since JOREK does not yet describe the toroidal velocity of the plasma. A toroidal rotation of the external magnetic perturbations at realistic velocity induced a clear screening of the RMPs. However, this result is not definitive since more physics requires to be included and the plasma resistivity needs to be pushed to much lower values (a resistivity much larger than the experimental one was required in the simulations for numerical reasons). It was also found that the magnetic perturbations induce convective cells at the edge which carry plasma from the confined region into the SOL. Estimates of the associated level of transport were done by studying the scaling of this phenomenon with plasma resistivity. Depending on the scaling, this mechanism could be responsible for a density flux across the unperturbed separatrix equal to 4.5 to 45% of the standard diffusive flux, meaning that it could be playing a role in the experimentally observed density pump-out.

In order to progress in the numerical modelling of RMPs penetration as well as plasma braking in presence of plasma rotation, it is convenient to make use of a cylindrical code rather than directly work with JOREK. We presented first simulations with this code, to be used as a basis for future developments. It is observed that, without any rotation, the

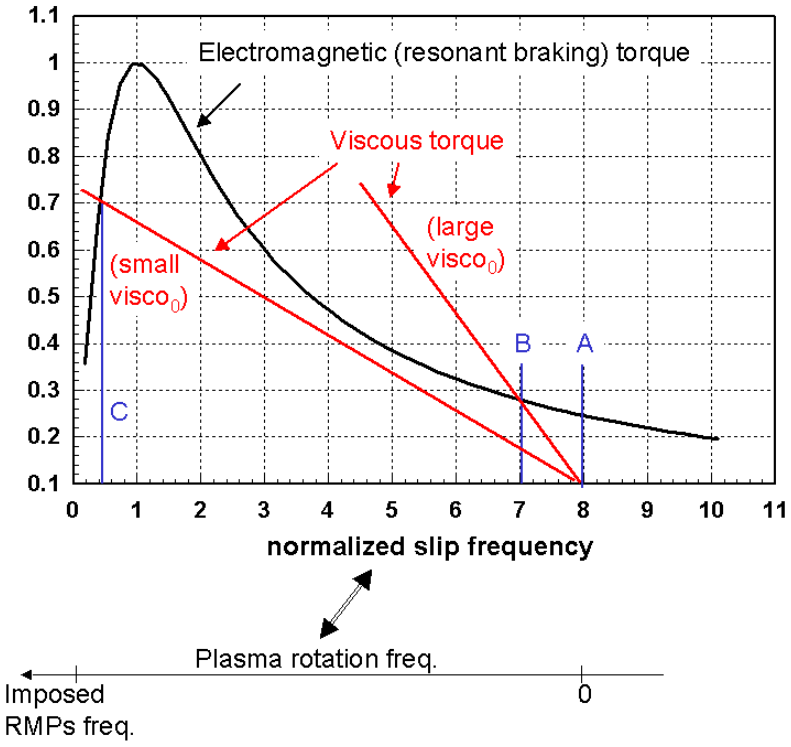

Figure 6.19: Conceptual plot explaining qualitatively the behaviour observed in the scan in the axisymmetric viscosity $visco_0$ at fixed $\psi^0_{3/1} = 10^{-5}$ and $\omega = 10^{-4}$ (see text).

penetration time is increasing as plasma resistivity decreases. With a toroidal rotation from the external magnetic perturbations, a plasma poloidal rotation appears, tending to reduce the slip frequency. RMPs penetration is associated to a significant drop in the slip frequency. A scan in the viscosity for the $(m = 0, n = 0)$ component of the flow showed that RMPs penetration only occurs below a certain viscosity. Above this viscosity, RMPs remain screened. All of these results are qualitatively consistent with the Fitzpatrick theory of RMPs penetration into a rotating plasma.

Conclusion

Since the first successful experiments at DIII-D in 2003, ELMs control by RMPs has been a subject of great interest in the fusion community. The reason for this is the potential application of the method to ITER.

Chronologically, the present work was first dedicated (from the end of 2004) to the design of ELMs control coils for ITER. The decision to start this work early (in view of the rather poor level of understanding of the DIII-D experimental results at the time) was justified by the ITER schedule: in order to have a chance to see ELMs control coils implemented into the machine, propositions of designs needed to be ready by the beginning of the ITER Design Review process, after which the design of the machine would be fixed. We developed the ERGOS code for this purpose and based our design studies for ITER on the reference case of the DIII-D I-coils. We assumed that the ergodization of the magnetic field at the edge was the reason for ELMs suppression. Our studies, mainly done in the frame of the EFDA-CEA ERGITER contract, revealed that designing ELMs control coils for ITER is not an easy task. In particular, the large size of the machine implies to use much larger currents in the coils than, for instance, in the DIII-D I-coils. Furthermore, it is not easy to avoid core RMPs because they are correlated to edge RMPs. Nevertheless, we were able to propose three candidate designs at the ITER Design Review. One of these designs, using coils external to the VV, was discarded because of the need to finalize rapidly the design of the ITER cryostat, with which these coils interfere, and because of the large non-resonant perturbations produced by these coils, a problem which we had not considered at first. Recently, the ITER management decided to provide a budget in order to implement ELMs control coils in the machine. However, the design of the coils is not decided yet between the two remaining possiblities out of the three that we have proposed. These two possibilities are either to wind coils around the blanket modules of the machine (which could be adapted into coils located just behind the blanket or in-between the VV walls) or to wind them around the midplane port plugs. The former is clearly the best solution from the physics point of view, but the latter is simpler from a technical point of view.

The decision to implement ELMs control coils in ITER is a strong motivation to pursue the efforts in order to better understand the physical mechanisms at play in ELMs control by RMPs. From this point of view, the experiments done at JET and MAST with the EFCCs are particularly interesting. While further experiments would be required in MAST in order to verify the possible but not certain effect of the EFCCs on the ELMs observed up to now, JET very clearly demonstrated a mitigation of the ELMs using the EFCCs in either $n = 1$ or $n = 2$ configurations, while the DIII-D I-coils produce $n = 3$

RMPs. In addition to the difference in n, the JET EFCCs are large monopole coils located far away from the plasma while the DIII-D I-coils are small multipole coils located close to the plasma. The fact that a clear effect on the ELMs was obtained with both types of coils shows the robustness of the method. A common point between these coils, in spite of their different aspect, was demonstrated using the ERGOS code: they both ergodize the magnetic field at the edge in the vacuum approximation. Furthermore, for the case of JET, we made a detailed comparison of the current required for ELMs mitigation and the one required for edge ergodization, and we found a satisfying correlation. This seems to confirm that edge ergodization is at the origin of the effect on the ELMs, a reassuring finding with respect to the design of the coils for ITER, which was based on this criterion. However, it must be said that the effect of the coils on the ELMs is not the same at DIII-D and at JET: at DIII-D, a complete ELMs suppression is obtained (at low ν_e^*), while at JET the ELMs become more frequent and smaller. In fact, the effect on ELMs of the JET EFCCs is similar to the one of the I-coils at DIII-D when q_{95} is outside the resonant window. On the other hand, the JET EFCCs and DIII-D I-coils (at low ν_e^*) have similar effects on the plasma profiles. In particular, they induce a clear pump-out of the density and they do not modify significantly the T_e profile, a surprising feature in an ergodic magnetic field.

A clear route towards a better understanding of the physics of ELMs control by RMPs is the numerical simulation with non-linear MHD codes such as JOREK. This will allow in particular to address the question of RMPs penetration into a rotating plasma and possible RMPs amplification by plasma effects. We found a screening of the RMPs in simulations for DIII-D, but these results cannot be considered as definitive since several key physics elements are missing and the plasma resistivity is much too large compared to reality. The work towards more relevant simulations has been begun and is ongoing at CEA Cadarache. A possibly interesting method of comparison between simulation results and experiments, with respect to the magnetic response of the plasma, is to study the magnetic footprints, which can, on the one hand, be calculated from the output of the simulations by following field lines until they hit the divertor, and on the other hand be observed experimentally on different signals, such as the IR images. For the case of JET, we showed that the theoretical footprints in the vacuum hypothesis should be observable experimentally and our calculations demand a comparison to experiment. This would be the occasion to directly test the vacuum hypothesis, which has gained some credibility from the good correlation found between ELMs mitigation and edge ergodization in our ERGOS calculations. If satisfying simulations of RMPs penetration are obtained which compare well with the existing experimental data, it will then be possible to make predictions for ITER.

The question of the transport induced by the RMPs is also a crucial one. Indeed, it was shown by linear MHD calculations for DIII-D that the ELMs suppression was due to the decrease in the pressure gradient induced by the RMPs. However, this decrease is not due to a decrease mainly in the temperature gradient, which could have been expected in an ergodized magnetic field, but rather to a density pump-out. Several mechanisms have been proposed in order to explain this pump-out. In particular, our JOREK simulations showed the existence of convection cells across the unperturbed separatrix due to the RMPs, which could be responsible for an enhancement of density transport, but we

were not able to quantify the level of transport very precisely. Furthermore, our model is one-fluid MHD and it would be interesting to address the impact of two-fluid effects.

Finally, an open subject of research of practical importance for ITER is to develop a scenario in H-mode with ELMs control by RMPs that can be safely extapolated to ITER. Crucial points are the ability to suppress all of the ELMs (which was never done up to now), to maintain the density in spite of the pump-out induced by the RMPs in order not to lower the fusion power[12] (which goes as the density squared) and to avoid core MHD modes.

Upcoming experiments at MAST with the new set of coils specifically designed for ELMs control (using ERGOS), at COMPASS-D (where ERGOS was also applied for calculating the best pluggings to use for the saddle coils in order to ergodize the edge) and at ASDEX-Upgrade (where new coils dedicated to ELMs control will also be installed soon), will be helpful in progressing both in the understanding of ELMs control by RMPs as well as development of scenarios for ITER.

[12]Related to this topic is the one of the compatibility of ELMs control by RMPs with plasma fuelling pellet injection (the forecasted fuelling method for ITER).

Appendix A

Calculation of the islands widths

In this appendix, we derive the analytical expression of the islands widths.

Defining:

$$B^1 \equiv \vec{B} \cdot \vec{\nabla} s, \tag{A.1}$$
$$B^2 \equiv \vec{B} \cdot \vec{\nabla} \theta^*, \tag{A.2}$$
$$B^3 \equiv \vec{B} \cdot \vec{\nabla} \varphi, \tag{A.3}$$

where s, θ^* and φ are the intrinsic equilibrium radial, poloidal and toroidal coordinates, the variations of s and θ^* with respect to φ along a field line can be written:

$$\left.\frac{ds}{d\varphi}\right|_{FL} = \frac{B^1}{B^3}, \tag{A.4}$$
$$\left.\frac{d\theta^*}{d\varphi}\right|_{FL} = \frac{B^2}{B^3}. \tag{A.5}$$

In order to study the trajectory of a field line near the rational surface $q = \frac{m}{n}$, it is convenient to define:

$$\chi \equiv \theta^* - \frac{n}{m}\varphi, \tag{A.6}$$

which implies:

$$\left.\frac{d\chi}{d\varphi}\right|_{FL} = \frac{B^2}{B^3} - \frac{n}{m}. \tag{A.7}$$

In the vicinity of the $q = \frac{m}{n}$ surface (located at radius $s = s_0$), we can use the following approximation:

$$\frac{B^2}{B^3} = \frac{1}{q} \tag{A.8}$$
$$\simeq \frac{1}{\frac{m}{n} + \bar{s} q'} \tag{A.9}$$
$$\simeq \frac{n}{m}\left(1 - \frac{n}{m}\bar{s} q'\right), \tag{A.10}$$

where $\bar{s} \equiv s - s_0$ and $q' \equiv \frac{dq}{ds}\big|_{s=s_0}$. Introducing this into eq. A.7, we find:

$$\left.\frac{d\chi}{d\varphi}\right|_{FL} \simeq -\left(\frac{n}{m}\right)^2 \bar{s}q' \tag{A.11}$$

$$\simeq -q^{-2}\bar{s}q'. \tag{A.12}$$

We can then write:

$$\left.\frac{d\bar{s}}{d\chi}\right|_{FL} = \left.\frac{d\bar{s}}{d\varphi}\right|_{FL} . \left.\frac{d\varphi}{d\chi}\right|_{FL} \tag{A.13}$$

$$= \left.\frac{ds}{d\varphi}\right|_{FL} . \left(\left.\frac{d\chi}{d\varphi}\right|_{FL}\right)^{-1} \tag{A.14}$$

$$\simeq -\frac{B^1}{B^3}\frac{q^2}{\bar{s}q'}. \tag{A.15}$$

Now, if in eq. A.15 we keep only the resonant component of $\frac{B^1}{B^3}$ and assume that it can be written in the form:

$$\left(\frac{B^1}{B^3}\right)_{res} = \tilde{b}^1_{res}\sin(m\chi) \tag{A.16}$$

(the most general expression would be $\left(\frac{B^1}{B^3}\right)_{res} = \tilde{b}^1_{res}\sin(m(\chi-\chi_0))$ but in that case we would redefine χ as $\chi - \chi_0$), then eq. A.15 can be integrated easily. Indeed, we can rewrite eq. A.15 in the form:

$$\bar{s}d\bar{s} \simeq -\frac{q^2\tilde{b}^1_{res}}{q'}\sin(m\chi)d\chi, \tag{A.17}$$

i.e.:

$$\frac{1}{2}d\left(\bar{s}^2\right) \simeq \frac{q^2\tilde{b}^1_{res}}{q'm}d[\cos(m\chi)], \tag{A.18}$$

which gives, after integration:

$$\bar{s}^2 \simeq \frac{2q^2\tilde{b}^1_{res}}{q'm}[\cos(m\chi) + C]. \tag{A.19}$$

The solutions of this equation for a set of values of the integration constant C, in the $(\chi, \bar{s})$ plane are displayed on fig. A.1, showing the typical island structure. The island separatrix, in bold line, is the limit between "trapped" and "passing" trajectories, and corresponds to $C = 1$. The island half-width δ can be expressed by taking the maximum of $\bar{s}$ for $C = 1$:

$$\delta_{q=\frac{m}{n}} = \left(\frac{4q^2\tilde{b}^1_{res}}{q'm}\right)^{\frac{1}{2}}. \tag{A.20}$$

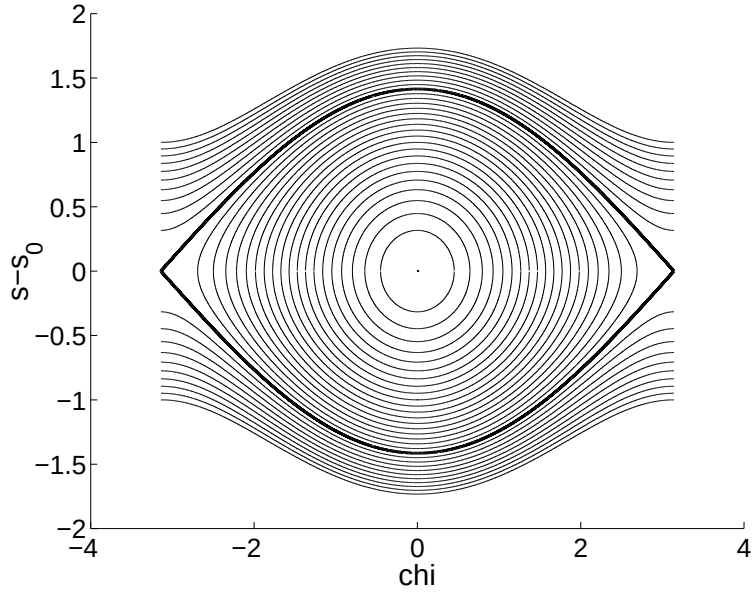

Figure A.1: m=1 island (here $\delta = \sqrt{2}$)

Appendix B

Demonstration of the r^{-m} dependence of magnetic perturbations with a poloidal mode number m in cylindrical geometry

Let us work in a cylindrical system of coordinates (r, θ, z) and let $\vec{B} = \vec{\nabla} \times \vec{A}$ be the magnetic field created by a current distribution directed along $\vec{e}_z$ and independent of z: $\vec{j}\,(r, \theta, z) = j_z\,(r, \theta)\,\vec{e}_z$, with $\vec{A}$ its vector potential. Then, it can be shown easily that:

$$\vec{A}\,(r, \theta, z) = \psi\,(r, \theta)\,\vec{e}_z, \tag{B.1}$$

where ψ is called the "magnetic potential". Assuming, furthermore, a poloidal symmetry of the system with a single poloidal mode number m, we can write:

$$\psi\,(r, \theta) = \psi_c(r)\cos(m\theta) + \psi_s(r)\sin(m\theta)\,. \tag{B.2}$$

Now, if we are in vacuum and study an electrostatic field, Ampère's law writes:

$$\vec{\nabla} \times \vec{B} = \vec{0}, \tag{B.3}$$

i.e.

$$\nabla^2\psi = 0, \tag{B.4}$$

i.e.

$$\left(\frac{1}{r}\,(r\psi_c')' - \frac{m^2}{r^2}\psi_c\right)\cos(m\theta) + \left(\frac{1}{r}\,(r\psi_s')' - \frac{m^2}{r^2}\psi_s\right)\sin(m\theta) = 0, \tag{B.5}$$

which (since this has to be satisfied for any θ) results in:

$$\frac{1}{r}\,(r\psi_c')' - \frac{m^2}{r^2}\psi_c = \frac{1}{r}\,(r\psi_s')' - \frac{m^2}{r^2}\psi_s = 0, \tag{B.6}$$

where the primes denote radial derivatives. The solutions for these second order differential equations are of the type:

$$\psi_{c/s}(r) = \psi^+_{c/s}r^m + \psi^-_{c/s}r^{-m}, \tag{B.7}$$

where $\psi^{+}_{c/s}$ and $\psi^{-}_{c/s}$ are constant numbers. If, in a region $0 < r < r_0$ there is no current, then only solutions of the type:

$$\psi_{c/s}(r) = \psi^{+}_{c/s} r^m \tag{B.8}$$

are acceptable, since otherwise there would be a divergence at $r = 0$. Therefore, in such a case, the magnetic potential has an r^m dependence. This results in an r^{m-1} dependence for the magnetic field amplitude.

Bibliography

[1] "La fusion nucléaire contrôlée par confinement magnétique" (collection CEA, Masson, 1987)

[2] J. Wesson, "Tokamaks", third edition (Clarendon Press, Oxford, 2004)

[3] R.J. Goldston and P.H. Rutherford, "Introduction to plasma physics" (Institute of Physics Publishing, Bristol and Philadelphia, 1995)

[4] Official website of the ITER project: www.iter.org

[5] "ITER Physics Basis", special edition of Nuc. Fusion, volume **39** (1999) number 12

[6] "Progress in the ITER Physics Basis", special edition of Nuc. Fusion, volume **47** (2007) number 6

[7] M. Shimada et al., Nucl. Fusion **47** (2007) S1-S17

[8] F. Wagner et al., Phys. Rev. Lett. **49** (1982) 1408

[9] C. Pérez von Thun, "MHD analysis of edge instabilities in the JET tokamak", PhD thesis, 2004

[10] H. Zohm, Plasma Phys. Control. Fusion **38** (1996) 105

[11] J.W. Connor, Plasma Phys. Control. Fusion **40** (1998) 531

[12] W. Suttrop, Plasma Phys. Control. Fusion **42** (2000) A1

[13] J.P. Freidberg, "Ideal Magnetohydrodynamics", Plenum Press, New York, 1987

[14] M. Bécoulet et al., Plasma Phys. Control. Fusion **45** (2003) A93-A113

[15] G.T.A. Huysmans, Plasma Phys. Control. Fusion **47** (2005) B165-B178

[16] P.B. Snyder et al., Nucl. Fusion **44** (2004) 320

[17] A. Loarte et al., Plasma Phys. Control. Fusion **45** (2003) 1549

[18] G. Federici et al, Plasma Phys. Control. Fusion **45** (2003) 1523

[19] A. Zhitlukhin et al., J. Nucl. Mat. **363-365** (2007) 301-307

[20] K. Kamiya et al., Plasma Phys. Control. Fusion **49** (2007) S43-S62

[21] P.T. Lang et al., Nucl. Fusion **43** (2003) 1110

[22] A. Grosman et al., J. Nucl. Mat. **313-316** (2003) 1314

[23] A.B. Rechester and M.N. Rosenbluth, Phys. Rev. Lett. **40** (1978) 38

[24] T.E. Evans et al., Phys. Plasmas **9** (2002) 4957

[25] T.E. Evans et al., Phys. Rev. Lett. **92** (2004) 235003

[26] R.A. Moyer et al., Phys. Plasmas **12** (2005) 056119

[27] T.E. Evans et al., J. Nucl. Mat. **337-339** (2005) 691-696

[28] T.E. Evans et al., Nucl. Fusion **45** (2005) 595-607

[29] T.E. Evans et al., Proceedings of the 32nd European Physical Society Conference on Controlled Fusion and Plasma Physics, Tarragona, Spain, 2005 (European Physical Society, Geneva, 2005), vol. 29C, paper I5-005

[30] K.H. Burrell et al., Plasma Phys. Control. Fusion **47** (2005) B37-B52

[31] T.E. Evans et al., Nature Phys. **2** (2006) 419

[32] M.E. Fenstermacher et al., J. Nucl. Mat. **363-365** (2007) 476-483

[33] Ph. Ghendrih, A. Grosman and H. Capes, Plasma Phys. Control. Fusion **38** (1996) 1653-1724

[34] J.C. Vallet et al., Phys. Rev. Lett. **67** (1991) 2662

[35] E.J. Doyle et al., Nucl. Fusion **47** (2007) S18-S127

[36] T.H. Osborne et al., Proceedings of the 32nd European Physical Society Conference on Controlled Fusion and Plasma Physics, Tarragona, Spain, 2005 (European Physical Society, Geneva, 2005), vol. 29C, paper P4-012

[37] I. Joseph et al., J. Nucl. Mat. **363-365** (2007) 591

[38] I. Joseph et al., "Calculation of the thermal footprint of resonant magnetic perturbations in DIII-D", to be published in Nucl. Fus.

[39] M.Z. Tokar et al., Phys. Rev. Lett. **98** (2007) 95001

[40] P.C. Stangeby, "The plasma boundary of magnetic fusion devices" (Plasma Physics Series, Institute of Physics Publishing, Bristol, 2000)

[41] G.L. Jackson et al., Proceedings of the 30th European Physical Society Conference on Controlled Fusion and Plasma Physics, St. Petersburg, Russia, 2003 (European Physical Society, Geneva, 2003), CD-ROM, paper P-4.47

[42] G. T. A. Huysmans, J. P. Goedbloed, and W. Kerner, "Isoparametric bicubic Hermite elements for solution of the Grad-Shafranov equation", in Proc. CP90 Conf. on Comp. Phys. Proc. (World Scientific Publ. Co. 1991), p. 371

[43] A.J. Lichtenberg and M.A. Lieberman, "Regular and Stochastic Motion", Applied Mathematical Sciences 38, Springer-Verlag, New York Heidelberg Berlin, 1983, p. 232

[44] C. Pérez von Thun, "MHD analysis of edge instabilities in the JET tokamak", PhD thesis, 2004, p. 69

[45] G. Agarici et al., "Design of a resonant magnetic perturbation ELM suppression system for JET", Fus. Eng. Des., in press

[46] P. Cahyna et al, "Resonant magnetic perturbations and edge ergodization on the COMPASS tokamak", to be submitted to Plasma Phys. Rep.

[47] I. Barlow et al., Fusion Eng. Des. **58-59** (2001) 189

[48] P. Cahyna and L. Krlin, Czech. J. Phys. **56** (2006) 367

[49] E. Nardon, "On the possibility of producing Resonant Magnetic Perturbations (RMPs) at the edge with the Error Field Correction Coils (EFCCs) without triggering core instabilities", EFDA Task Force MHD report of activites, June 26th 2006, http://users.jet.efda.org/pages/mhd-task-force/Meetings/TFMmeeting2006.06.27/Nardone.ppt

[50] Y. Liang, H.R. Koslowski, P.R. Thomas, E. Nardon et al., Phys. Rev. Lett. **98** (2007) 265004

[51] Y. Liang et al., "Mitigation of type-I Edge Localized Modes in H-mode Plasmas by Application of an $n = 1$ Perturbation Field on JET", JET science meeting, November 13th 2006, http://users.jet.efda.org/pages/mhd-task-force/Meetings/ScienceMeeting_2006-11-13/Liang_20061113_EFCC_new.ppt

[52] D. Darrow et al., Rev. Sci. Instrum. **77** (2006) 10E701

[53] T.E. Evans et al., "RMP ELM suppression in DIII-D plasmas with ITER similar shapes and collisionalities", submitted to Nucl. Fus.

[54] H.R. Koslowski et al., Proceedings of the 34th European Physical Society Conference on Controlled Fusion and Plasma Physics, Warsaw, Poland, 2007, paper P5.135

[55] Y. Liang et al., Proceedings of the 34th European Physical Society Conference on Controlled Fusion and Plasma Physics, Warsaw, Poland, 2007, paper I5.004

[56] L.L. Lao, H. St. John, R.D. Stambaugh et al., Nucl. Fusion **25** (1985) 1611

[57] S.S. Abdullaev and K.H. Finken, Nucl. Fus. **38** (1998) 531

[58] M.W. Jakubowski et al., Phys. Rev. Lett. **96** (2006) 035004

[59] T.E. Evans et al., J. Nucl. Mat. **363-365** (2007) 570-574

[60] A. Kirk et al., Phys. Rev. Lett. **96** (2006) 185001

[61] M. Bécoulet et al., Nucl. Fusion **45** (2005) 1284

[62] A. Grosman et al., J. Nucl. Mat. **313-316** (2003) 1314

[63] M. Bécoulet, E. Nardon et al., Proceedings of the 32nd European Physical Society Conference on Controlled Fusion and Plasma Physics, Tarragona, Spain, 2005 (European Physical Society, Geneva, 2005), vol. 29C, paper P2-005

[64] E. Nardon, M. Bécoulet et al., J. Nucl. Mat. **362-365** (2007) 1071-1075

[65] M. Bécoulet, E. Nardon et al., Proceedings of the 21st IAEA FEC, Chengdu, China, 2006, Paper IT/P1-29

[66] M. Bécoulet, E. Nardon et al., "First Intermediate Report on the Task: CEFDA05-1336 TW5-TPO-ERGITER: Resonant Magnetic Perturbations (RMPs) for ELMs suppression in ITER. Design studies of RMPs coils for ITER.", note de travail CEA/DRFC

[67] M. Bécoulet, E. Nardon et al., "Second Intermediate Report on the Task: CEFDA05-1336 TW5-TPO-ERGITER: Resonant Magnetic Perturbations (RMPs) for ELMs suppression in ITER. Design studies of RMPs coils for ITER.", note de travail CEA/DRFC

[68] M. Bécoulet, E. Nardon et al., "Final Report on the Task: CEFDA05-1336 TW5-TPO-ERGITER: Resonant Magnetic Perturbations (RMPs) for ELMs suppression in ITER. Design studies of RMPs coils for ITER.", note de travail CEA/DRFC

[69] M. Bécoulet, E. Nardon et al., "Numerical Study of the Resonant Magnetic Perturbations for Type I Edge Localized Modes Control in ITER", submitted to Nucl. Fusion

[70] M.J. Schaffer et al., submitted to Nucl. Fusion

[71] ITER physics basis 1999, Nucl. Fusion **39** 2175

[72] A. Polevoi et al., ITER Confinement and Stability Modelling, in J. Plasma Fusion Res. SERIES, Vol. 5 (2002) 82-87

[73] T.C. Hender et al., Nucl. Fusion **47** (2007) S128-S202

[74] F.L. Hinton and R.D. Hazeltine, Rev. Mod. Phys. **42** (1976) 239

[75] R. Fitzpatrick, Nucl. Fusion **33** (1993) 1049

[76] K.C. Shaing, Phys. Plasmas **10** (2003) 1443

[77] E. Lazzaro et al., Phys. Plasmas **9** (2002) 3906

[78] W. Zhu et al., Phys. Rev. Lett. **96** (2006) 225002

[79] K. Ioki et al, Fus. Eng. Des. **58-59** (2001) 573-578

[80] G.T.A. Huysmans, Plasma Phys. Control. Fusion **47** (2005) 2107

[81] G. Huysmans and O. Czarny, Nucl. Fusion **47** (2007) 659-666

[82] D. Biskamp, "Nonlinear Magnetohydrodynamics" (Cambridge monographs on plasma physics, Cambridge University press, 1993)

[83] H.R. Strauss, Phys. Fluids **19** (1976) 134

[84] H.R. Strauss, Phys. Fluids **20** (1977) 1354

[85] R. Izzo et al., Phys. Fluids **26** (1983) 2240

[86] S. Briguglio et al., Phys. Plasmas **5** (1998) 3287

[87] S.E. Kruger et al., Phys. Plasmas **5** (1998) 4169

[88] E. Nardon et al., Phys. Plasmas **14** (2007) 092501

Acronyms

ECE: Electron Cyclotron Emission
EFCCs: Error Field Correction Coils
EFDA: European Fusion Development Agreement
ELM: Edge Localized Mode
ETB: Edge Transport Barrier
HFS: High Field Side
ICRH: Ion Cyclotron Resonant Heating
ISP: Inner Strike Point
ITB: Internal Transport Barrier
IR: InfraRed
LFS: Low Field Side
LP: Langmuir Probe
MHD: MagnetoHydrodynamics
NBI: Neutral Beam Injection
NRP: Non-Resonant Perturbation
NPV: Neoclassical Poloidal Viscosity
NTM: Neoclassical Tearing Mode
NTV: Neoclassical Toroidal Viscosity
OSP: Outer Strike Point
P-B: Peeling-Ballooning
PF: Poloidal Field
RF: Radio Frequency
RMP: Resonant Magnetic Perturbation
RWM: Resistive Wall Mode
SOL: Scrape-Off Layer
TF: Toroidal Field
USBPO: United States Burning Plasma Organization
VV: Vacuum Vessel